Some aspects of the Martian climate in the Mars Orbiter Laser Altimeter (MOLA) Investigation

Part I. Evolution of the Polar Residual Ice Caps
Part II. Polar night clouds
Part III. Interpretation of the MOLA reflectivity measurement in terms of the surface albedo and atmospheric opacity

Thesis by

Anton Borisovich Ivanov

In Partial Fulfillment of the Requirements
for the Degree of
Doctor of Philosophy

California Institute of Technology
Pasadena, California

2000

(Submitted December, 9, 1999)

To Olga and Danil

To my parents

Acknowledgements

First and foremost I would like to thank Dewey Muhleman for being my advisor and mentor. Dewey taught me how to be a good scientist and, even more, how to be a good person. I was fortunate that Dewey somehow liked my Russian accent and was able to stand it for more than 5 years. Dewey's lectures were ones of the best I have ever had and greatly encouraged my curiosity in science. I am very grateful to Dewey for bringing me into the MOLA project and giving me a lot of responsibility there. It is a unique experience which I will never forget. Dewey is a wonderful person and I have a warm feeling that I am a member of a family. My thanks also go to Andy Ingersoll for providing me with an invaluable advice on all aspects of science, when I really needed it. I really enjoyed morning basketball games. I also would like to thank Bruce Murray for our talks and providing me with scientific and political wisdom. I thank Peter Schroeder for introducing me into the computer graphics world.

This work is totally based on the results from the Mars Orbiter Laser Altimeter investigation. It would not been possible without grand efforts by people from the MOLA team. Thanks go to all of them, especially Dave Smith and Maria Zuber who kept the whole operation running; Greg Newmann, "the MOLA guy," who is an incredible resource on every aspect of the MOLA data and a wonderful person to work with; Jim Abshire and Xiaoli Sun of the engineering team for a lot of fruitful discussions and advice. I would like to acknowledge the help of my colleagues from the TES team, Mike Smith and Tim Titus, who provided data for important comparisons.

I would like to extend my sincere thanks to Kay Campbell, Irma Black, Tammie Henderson, Susan Powell and Joyce Campbell for helping me with all of the Caltech matters. Thanks also go to Mike Black for providing support with computer "stuff" and rescuing some of my files from the backup.

Thanks to my officemates at different times for providing support and helping me to shape up my English: Stuart and Stuart, Liz, Charlie, Anthony, Antonin, Helen and Lori. The coffee break crowd contributed enormously to the enhancement of the social life at Caltech: Mark, Ashwin, Matt, Sarah, Gabe, Shane and all others. Thanks to graduate students before me: Mark (G), Eric and Albert for help and very interesting science discussions.

This acknowledgments would not be complete without thanking my Russian friends from Caltech: Mitya, Olga and Fedor, Tanya, Andy and Galka, Oleg and Nastya, Andrei, Alexander, Ilya, Max, Sergey, Sasha, "Red Rush" soccer team. Also thanks to Alexei, Ulyana, Yulya and Igor, my fellow Russians in the Geology department. Special thanks go to Slava Solomatov for enriching science discussions. I am missing our volleyball games.

I can never express how much the love and support of my parents, Boris and Natasha Ivanov, has meant to me. Thanks to my Dad for always trying to understand what it is that what I'm doing and always giving me sound advice, not only in science. Thanks to my Mom for care, understanding and advice on all of the life issues. I wish to thank my in-laws, Vladimir and Irina, for helping us at various times. This work would not have come to a fruition without the love and support of my family.

Above all, I express my deep appreciation and love for my wife, Olga Ivanova. It has been an emotional period in both our lives, but she has always been there for me. It is her patience, humor and love that keeps me going. Our son Danil is always a source of enjoyment and gives me a feeling of purpose in this life.

Abstract

The spacecraft exploration of the planet Mars in the last two decades provided scientists with an enormously rich data base. This work presents some aspects of the Mars Orbiter Laser Altimeter investigation related to the issues in the Martian climatology. The instrument continues to function on board of the Mars Global Surveyor Spacecraft.

The polar ice caps on Mars are the largest reservoirs of water on the planet. Their formation and evolution are not understood very well at this point. Ice flow, sublimation and wind erosion are believed to be the most important processes that shape the caps. We have developed a model to understand the role of sublimation for the formation of the ice caps and attempted to constrain the time scale for the formation of the observed ice caps. The model has been justified using the precise topography of the ice caps and the layered terrains that have been measured by the MOLA instrument. We argue that sublimation is a very important process for the formation of the caps, especially on the time scales greater than 10 million years.

We report the direct observations of CO_2 clouds, forming during the polar winter times over both poles. These clouds are similar over both poles and possibly represent a CO_2 snowfall. On the basis of the reflective properties and spatial occurrence, we can distinguish two major classes of clouds. We will discuss some hypotheses on the mechanisms of their formation.

Total atmospheric opacity of the Martian atmosphere at $1\mu m$ can be derived from the MOLA reflectivity measurement. Opacity estimates for the period from $L_s = 105°$ to $L_s = 220°$ are found to be consistent with the Viking Lander and Pathfinder values. Opacity measured in the polar regions displays storms and polar hood activity. Aerosol scale heights can be inferred from the opacity changes on some large scale topographic features. Dust scale heights are found to be lower than the atmospheric scale height. Water ice cloud scale heights are found to be consistent with the atmospheric scale height. Comparison of the MOLA derived opacity with the TES derived opacity yields information on the aerosol particle size distribution. We discuss an algorithm to derive $1 \mu m$ normal albedo of the surface. $9 \mu m$ dust opacity from the Thermal Emission Spectrometer (TES) is employed to remove an atmospheric attenuation from the MOLA reflectivity measurements. We will present some initial results on the calculation of the surface albedo.

Contents

List of Figures

List of Tables

Chapter 1 Introduction

> Есть ли жизнь на Марсе
> нет ли жизни на Марсе -
> науке это не известно
> наука пока ещё не в курсе дела
> Лектор из общества по распространению
> Карнавальная ночь, 1957 [1]

> "There is something fascinating about science.
> One gets such wholesale returns of conjecture
> out of such a trifling investment of fact."
> Mark Twain.

The past and present climate of the planet Mars have been receiving an increasing attention in the last decade. The answer to the question of existence of life on Mars depends on our knowledge about the planet's early environment. The hypothesis of warm and early Mars that could possibly host lifeforms requires a lot of testing. We will address some issues of the past climate in our sublimation model, developed to understand the evolution and current shape of the polar ice caps. The current climate state can be characterized using a large number of parameters. Dust opacity is one of the most important, because it regulates the heating of the atmosphere. Reflectivity measurements allow us to calculate total atmospheric opacity or to calculate albedos of the surface.

Starting in the late 1960's with Russian Mars 1 and US Mariner 4, there were a lot

---

[1] If there is life on Mars
or if there is no life on Mars
science is not aware
sceince is not well posted yet
Lector from Society on Distribution of Knowledge
Astronomy lecture on the New Year Eve. "Carnival Night" (1957)

of spacecraft missions, successful and not, to explore the surface and the atmosphere of the planet. Viking program was the most successful by far. Two landers and two orbiters returned an enormous amount of data, that was extensively analyzed during the next 20 years. After the failure of the Mars Observer in 1993, it was decided to split the original mission into several smaller missions over the course of 6 years. In 1996 Mars Global Surveyor Spacecraft was launched with a camera, spectrometer, magnetometer and a laser altimeter on board. The data collected by the Mars Orbiter Laser Altimeter are the foundation of this dissertation. This work constitutes a part of the MOLA investigation. Three major topics related to various climatological observations will be discussed: (1) evolution of the shape of the polar ice caps; (2) detection of the polar night clouds; (3) derivation of normal surface albedo and total atmospheric opacity from the measurement of surface reflectivity performed by MOLA.

1.1 Description of the MOLA instrument

General description of the MOLA-1 laser and scientific objectives can be found in Zuber et al. (1992). The MOLA-1 laser was a part of the ill-fated Mars Observer Mission, which failed to reach Martian orbit in 1993. MOLA-2 is an upgraded version of MOLA-1, with added capabilities. MOLA is a laser altimeter with Q-switched Nd:YAG laser operating at the wavelength of 1.064 μm . The range precision is about 37 centimeters, and a profiling resolution on the Martian surface is ~300 m. MOLA's vertical accuracy is limited by the orbital determination for the spacecraft, but is currently at about the 5-10m level and is expected to improve further with advanced orbit reconstruction techniques. By firing short (~8-ns) pulses of infrared light at the surface and measuring the time for the reflected laser energy to return, MOLA measures the range from the Mars Global Surveyor spacecraft to the tops of Mars' mountains and the depths of its valleys. The pulsing rate is 10Hz. Laser ranging schematic is shown in Figure 1.1. A portion of the output laser energy is diverted to the detector and starts a precision clock counter. A telescope focuses the light scat-

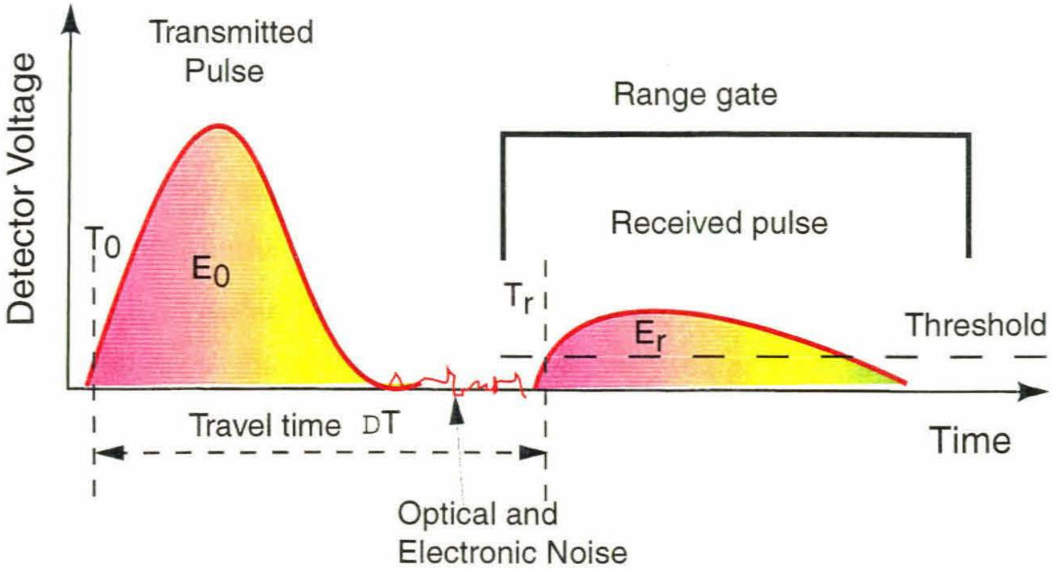

Figure 1.1: Laser ranging schematic. Range to the surface $R = c\Delta T/2$, $\Delta T = T_r - T_0$, T_0 - transmitted pulse time, T_r -received time, E_0 - transmitted energy, E_r - received energy. Detector can only register incoming photons when the range gate is open.

tered by terrain or clouds onto a silicon avalanche photodiode detector. Four separate channels filter the voltage output in parallel to detect pulses spread out by the roughness of terrain or clouds, increasing the likelihood of detection, and providing some information about surface roughness or cloud characteristics. Channels are sensitive to some amount of topography variation within a footprint: 3m (channel 1), 9m (2), 27m (3), 81m (4). More information about the channels and their characteristics can be found in section 3.3. The received pulse energy measures the near-IR reflectivity of the surface or cloud medium. In addition, measurements of the returned laser pulse width are providing fascinating information about the 100-meter-scale roughness of the Martian surface. The data analyzed in this dissertation contain > 200 million shots and the operations are continuing.

1.2 Topography of the polar regions

Precise topographic grids compiled by the MOLA instrument allow us for the first time an access to the shape of some very interesting features. Polar ice caps and polar layered deposits are the major known reservoir of water on Mars. Their shape was very poorly known prior to the MGS mission. Cited errors were at 1km level (James et al. (1992)). MOLA measurements allowed us to reconstruct the shape of the ice caps down to about 5m absolute error. It may be even possible to track changes in the seasonal snow cover.

The evolution and origin of the residual ice caps and layered deposits are poorly understood. The layered deposits are thought to be a record of the climatic variations on Mars, which are possibly due to variations in the planet's orbit. Just like the core samples from the Antarctic, they can help us to look in to the past climate of Mars. We have developed a time dependent ice sublimation model to reproduce the observed shape of the ice caps. Chapter 2 of this work describes the topography of North and South Polar regions and the model. Results of the model were compared to the MOLA topographic profiles. We attempted to constrain the time scale of the formation of the current ice caps, having sublimation as the only process that modulates the shape of the ice caps. Spiraling troughs in the polar layered deposits are a long-standing mystery. Their formation has not been explained yet. We attempted to analyze trough shapes and their time scales with the sublimation model. The model can reproduce the shape of the troughs very well. Sublimation models can not fully explain the process of the trough formation. However, the model can help to bound the time scales for trough formation. We will argue that sublimation is a very important process for the evolution of the ice caps and its time scales are shorter than that of the ice flow. Parts of this work will be published in the upcoming Mars Polar Science special issue of Icarus in Ivanov and Muhleman (2000).

1.3 Observations of the polar clouds

Condensation of CO_2 at the winter poles is a very important process in the current climate of Mars. Almost 25% of the Martian atmosphere is recycled through the polar ice caps every year. The condensed form of CO_2 have never been observed or quantified in any significant detail. MOLA is a very sensitive instrument and was able to detect faint returns coming from the clouds, forming over the polar regions when they were shrouded in winter darkness. The clouds are probably composed of CO_2 ice, which formed in very cold polar winter temperatures. A theoretical study was attempted by Gierasch and Goody (1968), who suggested a possibility of CO_2 cloud formation. In Chapter 3, we will present seasonal, spatial and elevation distributions of cloud returns. By the differences in reflective properties and spatial occurrence, we were able to classify two types of clouds: polar clouds forming poleward of 80° and clouds that formed only in the southern hemisphere just off the pole the latitudinal range from 70°S to 80°S. From the measurements of the reflected energy and the returned pulse width, we were able to calculate the backscattering coefficient of the cloud tops. We compare these values with backscattering coefficients for some Earth water cloud distributions. Simultaneous observations by the Thermal Emission Spectrometer enabled us to address the question of the low brightness temperature zones observed by both TES and IRTM (Infrared Thermal Mapper) instruments. MOLA cloud detections helped us to distinguish between the contributions of the CO_2 snowfall and condensing CO_2 on the ground.

1.4 Interpretation of the reflectivity

1.4.1 Atmospheric opacity

Along with the range to the surface, MOLA measures the returned signal strength and the width of the returned pulse. From the returned energy we can easily calculate the reflectivity for each shot. Reflectivity is a product of normal albedo of the surface at the MOLA wavelength ($1.064\mu m$) and the two-way transmissivity of the Martian atmosphere. The transmissivity here is an exponential function of the total atmospheric opacity at the MOLA wavelength. We can assume one of the above parameters to calculate the other from the reflectivity. To solve for the opacity of the Martian atmosphere we tentatively used the Plescot and Miner (1981) albedo dataset. In Chapter 4, we discuss what corrections have to be made for Plescot and Miner (1981) albedo data set to infer $1\mu m$ albedo for opacity calculations. We were able to estimate opacity for the duration of the mapping mission in several regions. We obtain values that are consistent with the Viking Lander and Pathfinder observations. Atmospheric opacities for the polar regions exhibit storm and polar hood activities. Simultaneous observations of opacity at $1\mu m$ by the MOLA and $9\mu m$ by the MGS Thermal Emission Spectrometer (TES) support the value of fundamental visible-to-IR scaling factor of 2.5 during the dust storm season. However, we have observed large deviations from this factor, especially in the southern winter. Visible-to-IR scaling depends on the particle size distribution of suspended dust in the atmosphere. Increased value of the ratio suggests an enrichment in smaller particle sizes ($< 2\mu m$). An algorithm for an aerosol scale height calculation is presented. It is based on the observations of opacity on large topographic features, such as Olympus Mons, Alba Patera and Hellas Basin. Dust scale heights were calculated on the slopes of Alba Patera and walls of Hellas Basin. Water clouds, formed during the southern winter, were observed near the Olympus Mons.

1.4.2 Surface albedo

One of the primary scientific objectives of the MOLA investigation is to compile a map of normal surface albedo at the MOLA wavelength. We will discuss an algorithm which employs the $9\mu m$ total dust opacity and water ice opacity derived by Smith et al. (1999b) to infer the total atmospheric opacity at the MOLA wavelength and remove atmospheric attenuation from a reflectivity measurement. The necessary opacity values were kindly supplied to us by M. Smith and J. Pearl or the TES team. This algorithm is based on the visible to IR dust opacity scaling ratio. Although the primary goal of the reflectivity study was to compile the albedo map of Mars, lack of quality simultaneous observations by both MOLA and TES instruments did not allow us to address this problem in complete detail. Saturation of the reflectivity measurement, which is discussed in Chapter 4, prevented the MOLA instrument from measuring all of the planet's reflectivity. After an increase in total atmospheric opacity during the dust storm season, MOLA collected unsaturated reflectivity measurements from about 70% of the surface. Work to employ TES dust opacity measurements for the calculation of the normal albedo at the MOLA wavelength is continuing. We present only some initial steps towards this goal.

1.5 Summary

This study addressed some issues relevant to the past and present climate on Mars, using data from the Mars Orbiter Laser Altimeter. The MOLA instrument was intended as a very precise geophysical tool to assess the shape and topography of the planet Mars. We hope that we have demonstrated utility of the instrument to shed some light onto the evolution of the ice caps, which pertains to the climatic evolution of the planet. Opacity maps provided by the MOLA can be used together with the TES opacity maps. Differences between the $1 \mu m$ and $9 \mu m$ opacity bear some information on the particle size distribution of the suspended aerosols in the Martian atmosphere. Finally, the $1 \mu m$ albedo map of Mars can be used for mineralogical studies and in atmospheric models.

Chapter 2 Martian Ice Caps

Martian polar deposits play a very important role in the cycles of the major constituents in the atmosphere: CO2, water and dust. However, very little is known about composition of the polar deposits or about dust and ice annual budgets (Thomas et al. (1992)). Results from the Mars Global Surveyor mission greatly enhances our knowledge about both North and South Ice Caps. This chapter will describe the observations of topography of North and South Polar Layered Deposits by the Mars Orbiter Laser Altimeter. A precise geometrical form of the polar layered deposits is now known. We will present a sublimation model for the evolution of the ice caps and compare the shape of the caps obtained from this model with MOLA topography observations of the North and South Polar Regions. The sublimation model developed in this work allows us to address the question of the time scale of the formation of the ice caps. Our simple sublimation model suggests bounds of 1mil-100mil years for the time scale for the formation of the observed ice caps on Mars. These bounds are greater than periods of currently known orbital variations.

A major part of the material presented in the following chapter will be published in the special Mars Polar Science Issue of Icarus (Ivanov and Muhleman (2000)). Some material was also discussed as a part of MOLA Science Team papers: Zuber et al. (1998a) (observations of the North Polar Ice Cap after the Science Phasing Orbits) and Smith et al. (1999a) (global topography of Mars and first observations of the South Polar Layered deposits).

2.1 Introduction

Major questions about Mars concern the origin and the evolution of the permanent ice caps in terms of their topographical shapes. their masses and their future configurations. The ice caps were first observed in the end of the 17th century by Cassini. Particularly during the last 3 decades we learned by means of ground based and spacecraft observations that they play an extremely important role in regulating the climate of Mars. It is well known that they are acting as a reservoir for CO_2 and maybe for water and dust.

The first to recognize the importance of the ice caps in regulating the climate of Mars was the model by Leighton and Murray (1966). More detailed and thorough theoretical studies of the climatic history of Mars can be found in Toon et al. (1980), who analyzed effects of the astronomical variations on the atmosphere of Mars. The climatic history of Mars is closely related to the most enigmatic feature of the ice caps: the polar layered deposits (PLD). A general discussion on PLDs can be found in Thomas et al. (1992). Their composition (e.g., dust/ice ratio) and rates of formation are still unknown. Various theories of their origin and evolution were discussed in papers by Squyres (1979), Howard et al. (1982) and Cutts and Lewis (1982). Most authors agree that layered terrain are formed by deposition of dust and water ice, and then exposed by erosion under the sun and wind.

Mariner 9 and Viking Orbiter spacecrafts have provided some insight into the topography and composition of the ice caps. The composition of the ice caps was determined by the Viking Infrared Thermal Mapper (IRTM), Kieffer et al. (1976a). These data showed the residual Northern Ice Cap to be composed of water ice. Direct confirmation of this result came from the Mars Atmospheric Water Detection (MAWD) experiment, Farmer et al. (1976). MAWD observed an enhanced water vapor abundance over the North Pole during the summer time, when all the CO_2 frost is gone and most of the area of the residual cap is exposed. Dzurisin and Blasius (1975) used stereogrammetry and occultation data to create topographic maps and estimated the thickness of the layered deposits at 4 to 6 km. Later, Malin (1986) suggested that the maximum thickness is 5km along the ridge at 87°N.

The detailed shape of the North Polar Ice Cap (NPIC) has been measured to high accuracy with the Mars Orbiter Laser Altimeter (MOLA) instrument on the Mars Global Surveyor (MGS). The general instrument description can be found in Zuber et al. (1992). First observations of the Northern Hemisphere topography were published in Zuber et al. (1998a). The first global topography results are published in Smith et al. (1999a). The topography of both caps has been well sampled with nadir-viewing tracks for latitudes south of 87°N. The remainder of the caps to the pole was sampled in 10 tracks spread over the complete longitude range. To zeroth order, topography of both caps is parabolic in shape and extends down to a latitude of about 80° (Fig. 2.1).

The details of the cap as revealed by MOLA include troughs and layering as well as large scale asymmetries such as Chasma Boreale. Even without knowing the origin of the ice cap we can safely say that its current configuration is due to the combined forces of elastic displacements and ablation due to sublimation from the ice surface over the range of annual equilibrium temperatures at a given latitude. The latter effects would be modified by local winds, surface roughness, etc.

In this paper we consider the effects of ablation through sublimation on the current shape of the NPIC. We used the model to calculate the thickness of the water ice layer sublimated and deposited onto the residual ice cap over one Martian year. The model was cycled for the equivalent of millions of years. The results of the model simulations were compared to the MOLA topography. We have been able to reproduce the overall shape of the cap and details of selected troughs. We include in this investigation a discussion of the estimation of ablation time scales and the major difficulties in making such estimates. We have not attempted the development of a definitive model of the evolution of the cap with accurate time scales. The primary goal of the paper is to understand the shape of the general cap and to understand the development of the troughs.

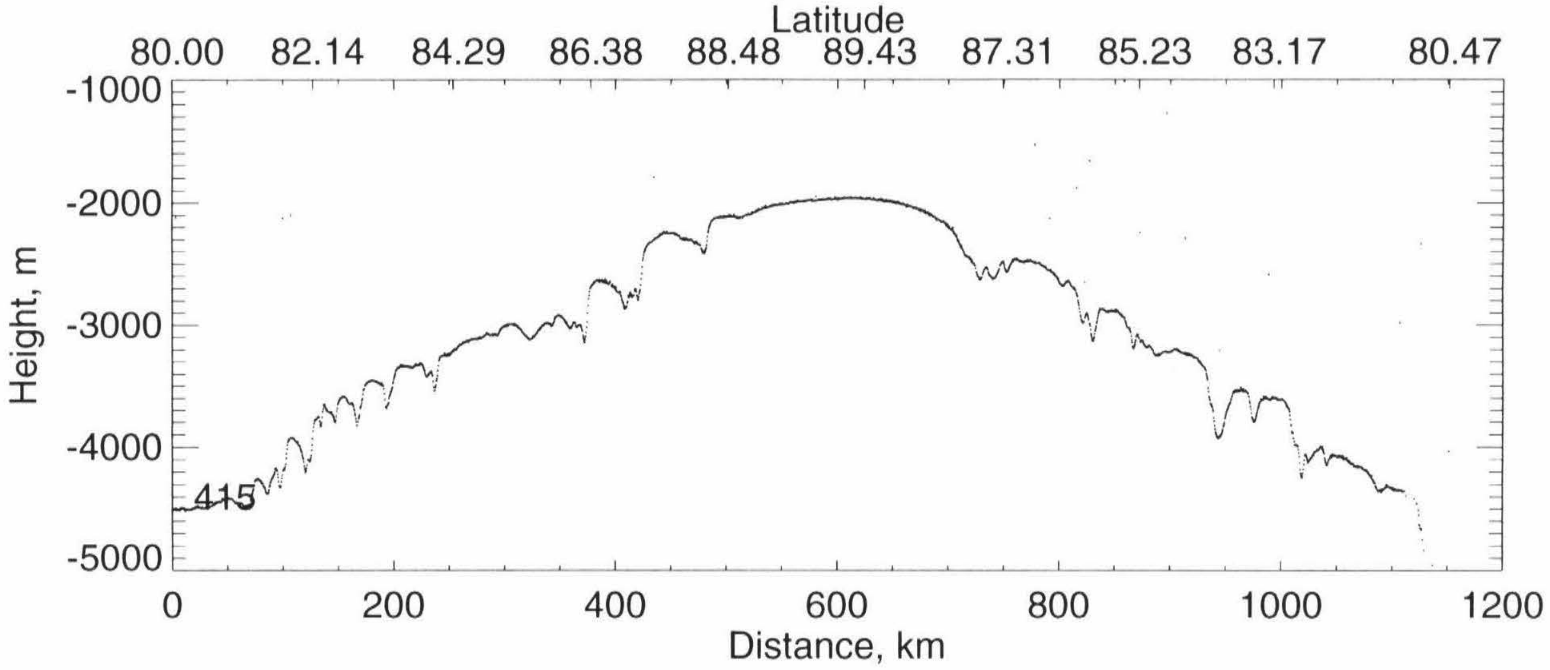

Figure 2.1: Cross section of the North Pole along 90°E-270°E longitude. Data from track 415. Vertical exaggeration is about 1:100. Elevations are negative because they are given relative to the geoid model of Mars Zuber et al. (1998a). The shape of the ice cap is parabolic to the zeroth order and in this respect similar to, for example, the cross section of the Antarctica ice sheet on Earth. The distance is from 80°N.

2.2 Topography data

Mars Orbiter Laser Altimeter (MOLA) instrument has presented us a long awaited opportunity to measure the altimetry of the North Polar ice cap (NPIC) and the South Polar Ice Cap (SPIC) of Mars. Science data campaigns consist of several large separated periods of time due to aerobraking, problems with one of the solar panels, high-gain antenna release, etc. A summary of periods when topography data were taken and corresponding acronyms is presented in Table 2.1

Name	Time period	NPIC data	SPIC data
Hiatus	9/15/97 - 11/6/97	Only the edge	No
Science Phasing Orbit 1 (SPO1)	3/28/98-4/28/98	Yes	No
Science Phasing Orbit 2 (SPO2)	5/28/98-7/30/98	Yes	No
Bonus, pre-mapping	2/28/99-3/26/99	Yes	Yes
Mapping	4/2/99 - 1/01 (planned)	Yes	Yes

Table 2.1: Periods of science data campaigns and corresponding acronyms

During the Science Phasing Orbits (SPO) period a little less than 200 tracks were obtained and all of them crossed the NPIC. Geometry of the orbit and limitations on MOLA range allowed only observation of regions north of equator. Dense coverage, comparable to expected during mapping, was obtained for regions north of about 60°N. Due to the orbit inclination of the Mars Global Surveyor spacecraft, MOLA was only able to measure topography up to about 86.3°N. Fortunately, 10 times during the SPO period the spacecraft was tilted towards the North Pole (by $\sim 50°$) and collected altimetry across the center of the ice cap. This maneuver partially filled the gap in coverage and measured the maximum thickness of the NPIC. First analysis of the NPIC topography is presented in Zuber et al. (1998a). All of the tracks are shown in Fig. 2.2. Zuber et al. (1998a) performed an interpolation of all MOLA data to a 1 km spatial resolution grid north of 75°N to the pole. We present two 3D renderings of this grid in Fig. 2.3 with a mosaic of Viking summer images of the North Pole draped over the MOLA topography.

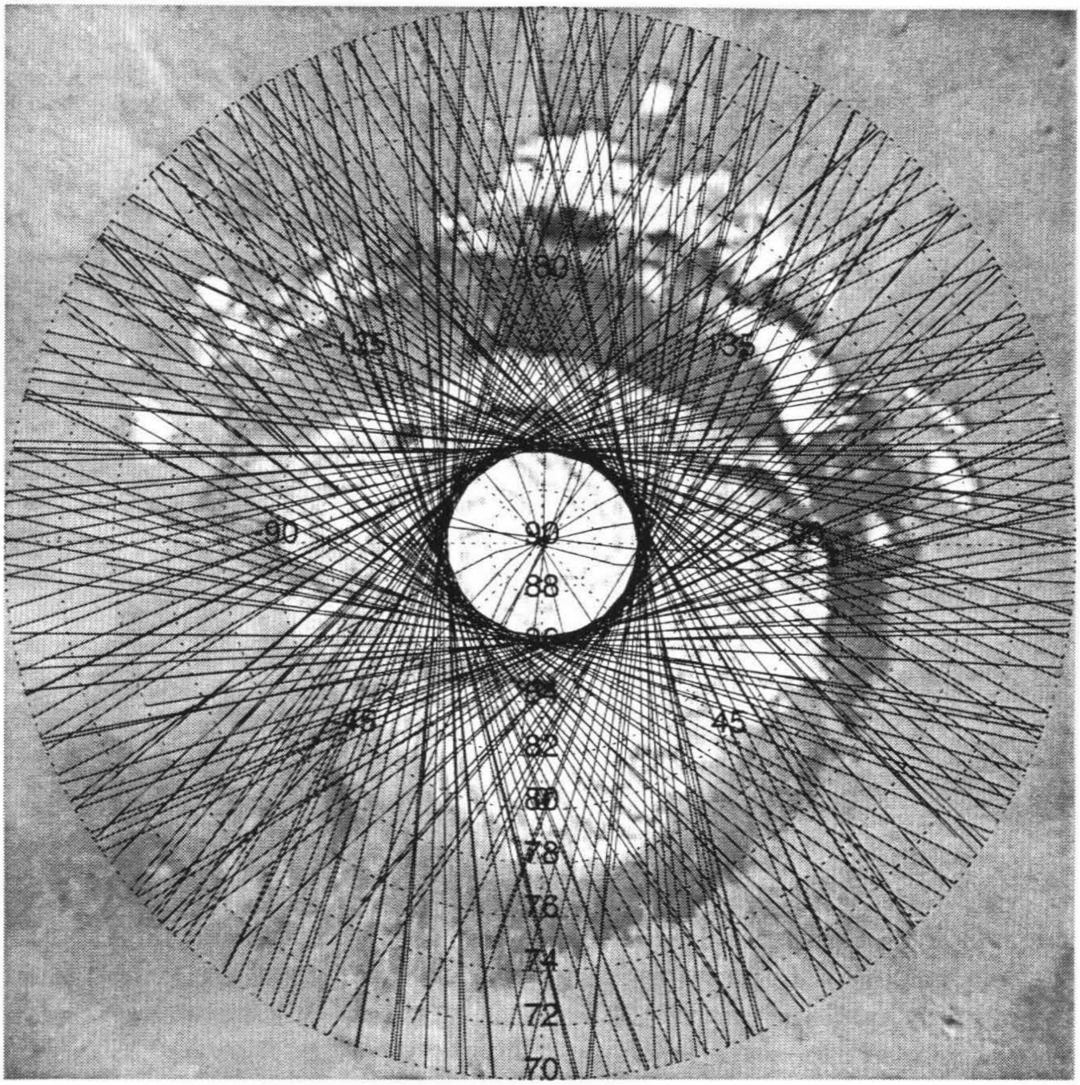

Figure 2.2: MOLA coverage of the North Polar Region at the end of Science Phasing Orbit (north of 70°N shown from 0°E longitude). Inclination of the spacecraft orbit allowed MOLA to measure topography up to about 86.3°N at normal incidence. In addition, MOLA was able to collect cross sections through the center ice cap, when the spacecraft was tilted towards the center of the NPIC.

Figure 2.3: Three- dimensional view on the Martian Polar Region north of 75°N. The North Pole is at the center of these images. The topography grid is compiled from the MOLA data by G. Neumann (see Zuber et al. (1998a)). Viking Mosaic of summer images taken by Viking spacecraft shown over the topography. Elevation range here is about 3km. Vertical exaggeration is 1:200. View in a) is shown from 90°E longitude. This rendering displays significant asymmetries between left and right (as seen on this view) parts of the cap. Dark area on the right side is Olympia Planitia - huge dune formation. View in b) is shown from 180°E. Olympia Planitia is before the ice cap in this view. Notice general parabolic shape of the ice cap from this point.

The MOLA instrument initiated near-continuous global profiling of Mars on February, 28, 1999, and started providing data over both northern and southern hemispheres. Again, the geometry of the orbit did not allow observations of the center of the ice caps. A specially designed maneuver to tilt the spacecraft towards both polar regions was performed during the mapping campaign. It is now possible to compile a complete topographic grid for the whole planet, including the poles. Topography grid for the SPIC after a month of mapping is shown in Fig. 2.5.

The maximum thickness of the ice cap, measured relative to the surrounding plains, is about 2.7 km. This value is observed right at the pole (90°N). As we mentioned earlier, the cross-sectional form of the ice cap is roughly parabolic (e.g., Fig. 2.1 and Fig. 2.3b). This is similar to the form of large ice sheets on Earth, such as the Antarctica ice sheet. In that case, the topography is caused by the rheology of the "warm" ice.

Almost all the tracks over the ice caps have crossed troughs in the polar layered deposits. The depth of the troughs varies greatly. The deepest troughs are about 1 km deep and cut the layered deposits to almost the level of the surrounding plains. It was known from previous observations that equator facing walls are steeper than north facing slopes. MOLA observations showed south facing slopes to be of order $4^\circ - 7^\circ$ and north facing slopes $2^\circ - 4^\circ$.

Chasma Borealis is a large reentrant trough, which cuts the NPIC almost in two. It is slightly elevated over the surrounding plains ($\sim$ 200m) and is 600 km long. Elevation of the floor in Chasma Borealis only varies by about 200m. Various mechanisms were proposed to explain its formation including catastrophic discharge of melted water by Clifford (1987) and erosion by winds Howard (1998). Symmetric from Chasma Borealis across the pole is the Olympia Planitia - a huge dune field. Its origin is also unknown. It was proposed in Zuber et al. (1998a) that Olympia Planitia is the remnant ice from an ancient larger ice cap. These deposits may now be covered by dunes and preserved.

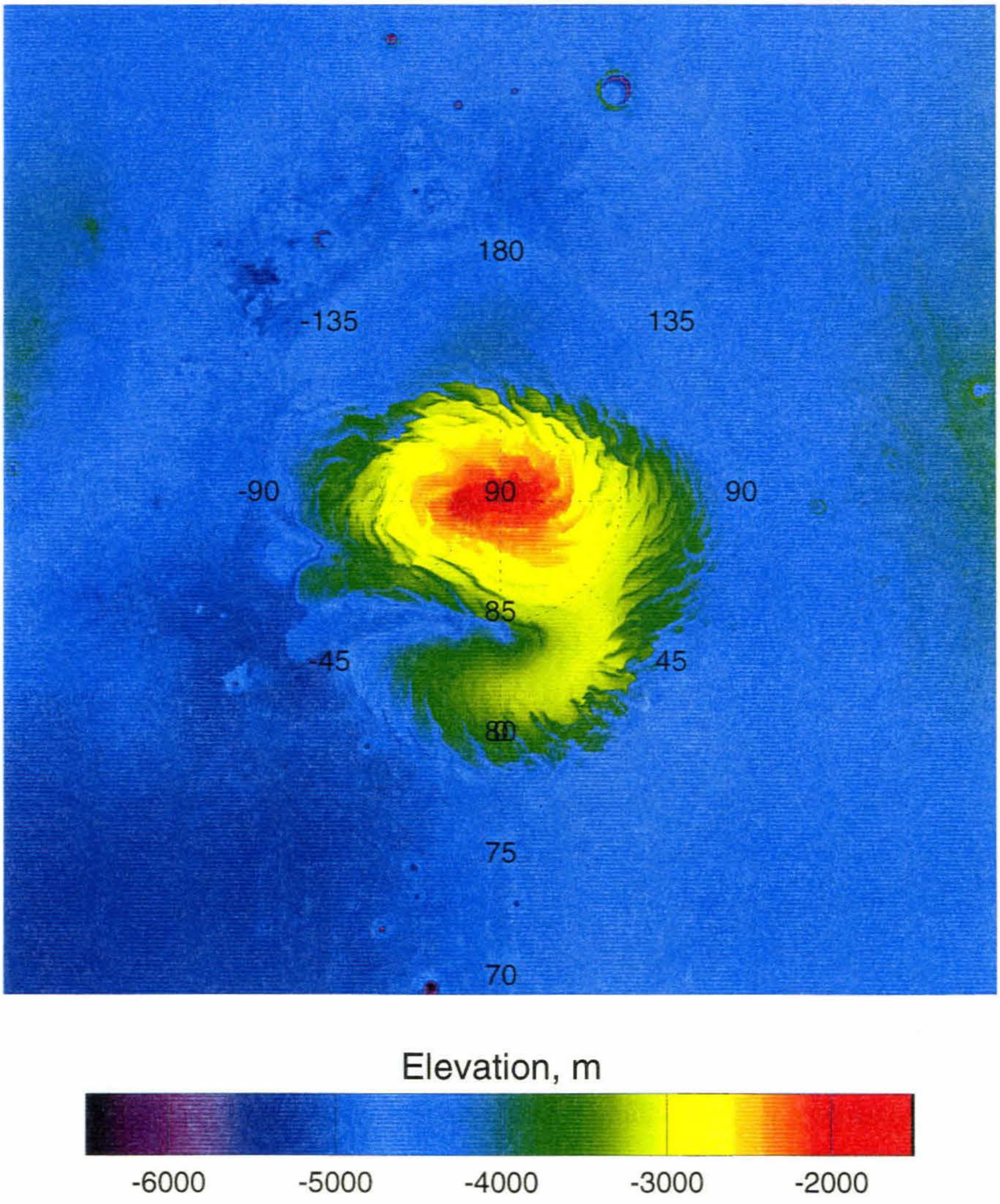

Figure 2.4: Polar stereographic projection showing the high resolution digital topographic model of the North polar region from latitude 70°N to the pole (Zuber et al. (1998a)).

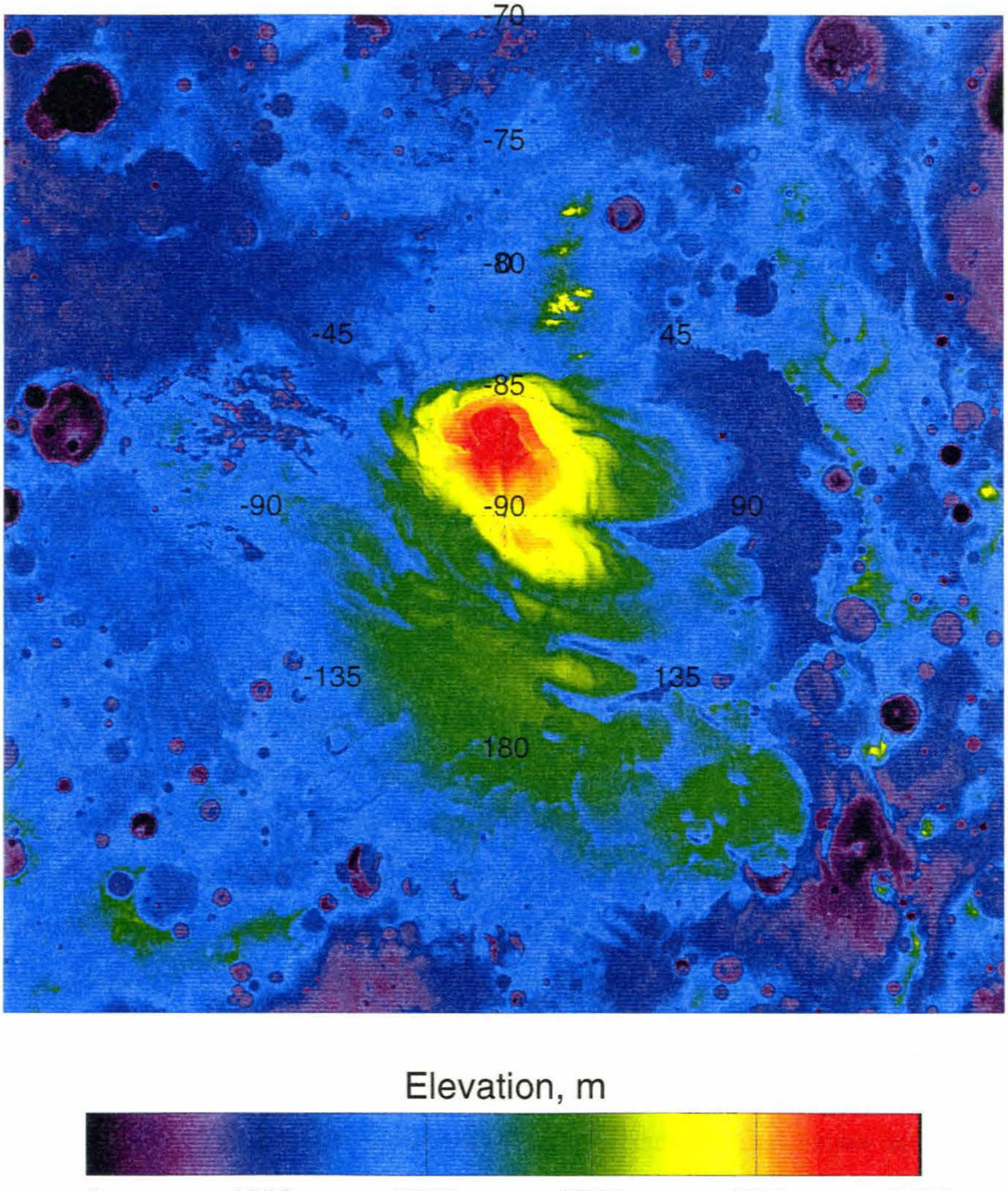

Figure 2.5: Polar stereographic projection showing the high resolution digital topographic model of the South polar region from latitude 70°S to the pole (Smith et al. (1999a)).

2.3 Sublimation model

In this section we will describe the sublimation model and discuss its limitations. Our discussion builds on early works on the general problem by Ingersoll (1970), Toon et al. (1980) and Haberle and Jakosky (1990). There are two processes involved in sublimating water vapor: turbulent transfer and convective evaporation. The sublimation process depends to some extent on the Martian atmosphere near the ice surface, which is essentially pure CO_2 gas. If the Martian ice were in a pure vacuum (such as the case for the ring particles at Saturn), the water loss rate at any instant of time could be computed using the expression from kinetic theory

$$\frac{dM}{dt} = -p_{sat}(T)\sqrt{\frac{m_w}{2\pi kT}}, \tag{2.1}$$

where $\frac{dM}{dt}$ is the water mass loss rate per unit surface area in $g/cm^2/s$, $p_{sat}(T)$ is the water saturation vapor pressure over ice at temperature T, m_w is the mass of a water molecule and k is the Boltzmann constant. Eq. 2.1 is derived by assuming the water vapor very near the surface is saturated with a velocity distribution given by the Maxwell distribution. The flow of water molecules from the surface is given by the integral over the vertical velocity from 0 to ∞. At any given epoch there is a vertical distribution of water vapor in the Martian CO_2 atmosphere which was measured for the north polar region during the Viking mission and reported by Farmer and Doms (1979), Jakosky and Farmer (1982) (see also a more recent discussion by Jakosky and Haberle (1992)). The effect of the atmospheric water vapor would be to *slow down* the sublimation rate. If the partial pressure of the water vapor, p_{H_2O}(t), is greater than $p_{sat}(T)$, then condensation of water occurs on the surface and the cap grows. The "t" in the argument of p_{H_2O} refers to time during the Martian season. Eq. (2.1) should become

$$\frac{dM}{dt} = -(p_{sat}(T) - p_{H_2O}(t))\sqrt{\frac{m_w}{2\pi kT}}, \tag{2.2}$$

where $p_{H_2O}(t)$ - the ambient partial pressure of water vapor, is a function of season on Mars, m_w - molecular mass of water, T - the surface temperature. is assumed to be equal for the surface and atmosphere *adjacent* to the surface.

The variation of the water vapor over the NPIC is probably directly connected to the annual cycle of water vapor from the cap to the atmosphere. This could in principle be included as a feedback mechanism in our calculations, but would greatly complicate the problem. In this study we used Viking-like water vapor cycle, which was observed by the MAWD instrument, Jakosky and Farmer (1982). This cycle is parameterized in Eq. (2.4).

We believe that Eq. (2.2) would be a good estimator of $\frac{dM}{dt}$ except for the important effects of the CO_2 atmosphere, winds, turbulence and the buoyancy effects of the lighter H_2O molecules in the CO_2 atmosphere. The buoyancy effect would apparently diminish the loss rate, and turbulence would reduce this effect by removing water vapor from the near surface. The dependence on T in Eq. (2.1) and Eq. (2.2) is exponential in $p_{sat}(T)$ of the form

$$p_{sat}(T) = C_0 * exp(-C_1/T), \tag{2.3}$$

where C_0 and C_1 are known constants. Consequently, the temperature T dependence in the radical of Eq. (2.2) is relatively unimportant. The water vapor partial pressure term above the laminar layer in Eq. (2.5) is taken to be (in mbars)

$$p_{H2O}(t) = 1.3 * 10^{-3} + 1.3 * 10^{-3} * sin(L_s(t)), \tag{2.4}$$

corresponding to 70 $pr.\mu m$ of water vapor at the northern summer solstice ($L_s = 90^\circ$) and 0 $pr.\mu m$ of water at the winter solstice ($L_s = 270^\circ$). L_s is the aerocentric longitude of the Sun. It is a convenient measure of seasons on Mars. We do not consider sublimation or condensation of water ice during $0^\circ < L_s < 80^\circ$ in the model. No sublimation will occur during this period due to extremely cold temperatures and CO_2 blanketing. We neglect condensation during this period as most of the water vapor had likely condensed in the fall and beginning of the winter ($L_s = 180^\circ - 360^\circ$).

We also assume negligible water transport from lower latitude to the ice cap. Water coming from the lower latitudes will condense and fall out before it reaches 80°N. Unfortunately, there are no MAWD observations for this period of time, but we can safely assume that the amount of water vapor during winter is small. We hope to use Mars Global Surveyor Thermal Emission Spectrometer (TES) temperature and water vapor opacity observations to support this assumption.

We argue in section 2.4 that the meteorological terms listed above essentially scale the dM/dt term in Eq. (2.2), significantly slowing the loss rate without affecting the shape of the ice cap. That is, we assume that the loss rate is given by

$$\frac{dM}{dt} = -D(T, u_*, u, z_0)(p_{sat}(T) - p_{H_2O}(t))\sqrt{\frac{m_w}{2\pi kT}}, \tag{2.5}$$

where D is very nearly a constant for the Martian polar region and a function of wind speed (u_*, u), surface roughness (z_0) and a weak function of temperature (T) (see Appendix 2.1). In any case, the temperature dependence in Eq. (2.5) is contained overwhelmingly in the exponential term in the saturation vapor pressure. D here defines only the time scale. The derivation of an expression very similar to that in Eq. (2.5) is presented in Appendix 2.1. In fact, it can be shown that Eq. (2.5) is similar to expression $\frac{dM}{dt} = 0.002\rho_w u$, which was used in other works (e.g., Ingersoll (1970), Toon et al. (1980), Haberle and Jakosky (1990)). This equation was developed and used for treating evaporation problems over Earth's oceans. Previous authors did not justify the use of this equation for sublimation of Mars' ice caps. This work (see Appendix 2.1) shows how a similar equation can be derived. It also provides analysis for the value of the constant drag coefficient ($\sim$ 0.002). We actually did our calculations of the evolution of the ice cap using Eq. (2.5) with D = 1.0. This necessarily leads to an ablation time scale that is too short. We will address the problem of the time scaling in section 2.4.

We compute the loss of water from the cap over one Martian year using the current obliquity of Mars of 25.2° even though it has not been constant during the evolution of the NPIC. In summing over the Martian year we assume an orbit with eccentricity equal to 0.0934 (current value). Variations of obliquity and eccentricity have a considerable effect on the Martian climate. To account for all the effects of variable orbit, we would have to introduce response of atmosphere and water cycle. The sublimation model would become extremely complicated. The orbital model in this work represents a good approximation for the major goal of this paper - the shape of the ice cap. Ablation time scale will be more affected by considering a real orbit. We discuss the effect of obliquity cycle on sublimation results in section 2.4.

We start the model calculation with a uniformly thick layer of ice (2.3 km) down to a latitude of 80°N. Numerical tests using a starting latitude for the cap of 70°N yielded essentially the same results, because the ice cover rapidly vanishes at these lower latitudes. Under any reasonable assumption of the initial cap thickness there is little variation in the final thickness right at the pole. Thus, the initial thickness was selected to match the observations. The shape of the initial deposit, a rectangle or a parabola, does not influence our final results, except for different number of model cycles required to reach the final shape. Any shape with a constant second derivative will relax eventually to a parabolic shape due to latitudinally varying insolation.

Using a Bond albedo of 0.5 we compute the equilibrium temperature at 150 latitude points from 80°N to the pole. The surface temperature is a function of time and location of an individual point on the surface. It is found from a simple radiative energy balance:

$$\sigma T^4(t,\theta) = (1-a)I_{Mars}cos(\theta) - L\frac{dM}{dt}(t,T), \tag{2.6}$$

where σ - Stefan-Boltzmann constant; I_{Mars} - is the solar constant at Mars $= 590W/m^2$; L is the latent heat of ice $= 2.8 * 10^6 J/kg$; a - albedo of the surface $= 0.5$ (in troughs we decreased the albedo by about 10%); θ - angle of *local* Sun incidence, which takes into account the latitude of a single point on Mars and the local slope. Thermal inertia for ice is relatively large, but we assume that it will have a small effect compared to other terms in Eq. (2.6). We set the surface temperature to the CO_2 condensation temperature of 150 K whenever the equilibrium temperature falls below this value.

The loss of water over the Martian year is then multiplied by 10 and the shape of the cap is adjusted as a function of latitude. Since the calculation is done with D=1.0 in Eq. (2.5), our integration step would be 10 Martian years. We will show in section 2.4 that D is less than unity and the step is significantly greater than 10 years. The calculation is then repeated with the new shape of the cap, including the detailed local angle of incidence of the Sun which is always greater than the latitude (except in a trough).

The second mechanism is convective evaporation. It occurs because molecules of water are lighter than CO_2. This mechanism has been described in Ingersoll (1970).

$$\frac{dM}{dt} = 0.17 * \rho_w D' \left(\frac{\frac{\delta\rho}{\rho} * g}{\nu^2} \right)^{1/3}, \tag{2.7}$$

where ρ_w - water vapor mass density; D' - diffusion coefficient of water vapor in CO_2; $\frac{\delta\rho}{\rho} = \frac{26P_w}{44P_{CO_2} - 26P_w}$; ν - viscosity of CO_2. This formulation assumes negligible amounts of water vapor over the surface. Our calculations show that convective evaporation is not important for the temperature range that we are considering in this paper (150-210K).

The average effect of sublimation and condensation is for the southern edge of the cap to retreat northward, for the cap to grow at the pole and for the general shape to approach a parabola of revolution about the North Pole. Typical shapes of the cap for different number of cycles are shown in Fig. 2.6.

We consider the formation and evolution of the dark troughs in separate calculations by decreasing the Bond albedo in a latitude band by a few percent, say to 0.48. A typical final trough shape is shown in Fig. 2.13. Comparisons of the modeled ice cap and trough with the MOLA topography profiles is discussed in section 2.5.

2.4 Timescales

In order to estimate a meaningful time scale, or bounds on that scale, for the ablation evolution of the NPIC, we must estimate D in Eq. (2.5). D is the factor, less than

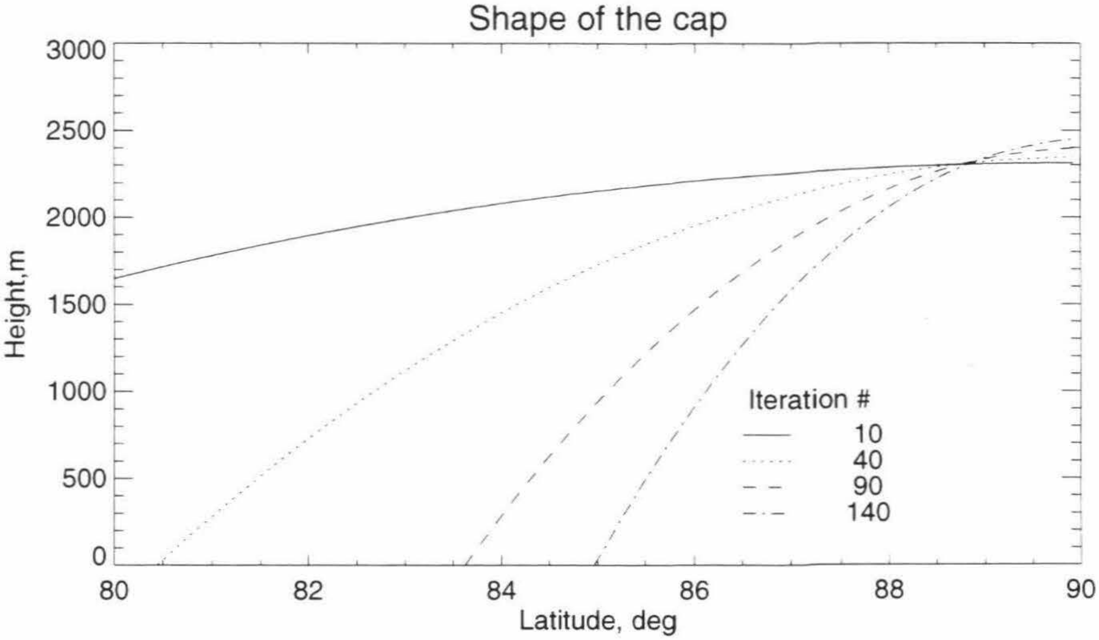

Figure 2.6: Sample output from the sublimation model. Several consecutive cycles are shown. Initial condition is 2.3 km thick ice cap. One cycle is one "model year" ×10 Martian years ×F, where F is bounded between 12×10^3 and 60×10^3. Thus, one cycle is bounded by 120 and 600 thousand Martian years. See section 2.4 for discussion of the time scales.

unity, that slows the sublimation relative to the situation of ice in a vacuum. From Eq. (2.24) in the appendix and Eq. (2.5)

$$D = \sqrt{\frac{2\pi m_w}{kT}} Au, \tag{2.8}$$

where A is the 'drag' coefficient at height z and u is a measure of the wind speed at that height. Research on the Earth's surface and in wind tunnels led Jakob (1957) (see also Priestley (1959)) to adopt a value of A = 0.0022 at $z \sim 1$ meter. Peixoto and Oort (1992) state that A = 0.0013 over oceans, which are, of course, very smooth. Paterson (1994)(pg. 66) suggests the use of 0.002 for icy surfaces. We will tentatively "adopt" a value of $A = 0.002$ with the realization that u is even more uncertain. Based on Viking Lander measurements, a reasonable minimum value is $u \sim 1$ m/s and a practical maximum $u \sim 5$ m/s. The winds may be much higher over the NPIC, speeding up the ablation process, and are probably rarely as low as 1 m/s. Using $A = 0.002$ and $u = 1$m/s in Eq. (2.8), D = 1.65×10^{-5}. Using $u = 5$m/s, $D = 8.25 \times 10^{-5}$. Consequently, we adopt as *reasonable* bounds

$$1.65 \times 10^{-5} < D < 8.25 \times 10^{-5}. \tag{2.9}$$

Thus, one model cycle is equivalent to 10 Martian years and multiplied by a factor F

$$12 \times 10^3 < F = \frac{1}{D} < 60 \times 10^3. \tag{2.10}$$

We feel that the lower bound of 12×10^3 is much more likely since the winds over the NPIC are probably greater than 5 m/s. For example, the NPIC evolution time from the initial configuration of a uniform ice sheet down to a latitude of 80°N illustrated in Fig. 2.8 (quadrant 90) requires 53 model cycles. One model cycle is equivalent to 10 Martian years multiplied by factor F from Eq. (2.10). Thus, one cycle is bounded between 120 and 600 thousand Martian years and the timescale for NPIC evolution in quadrant 90 roughly falls in the range 6.4 - 31.8 million Martian years. Fig. 2.8 is discussed in more detail in section 2.5.

Large variations of obliquity (e.g., Toon et al. (1980)) will influence our timescales. We present in Fig. 2.7 model runs for three different values of Mars obliquity: 0°, 25.2° (current) and 40°. According to our model, evaporation rates reach 1.3 mm/year during high obliquity periods. This rate is much higher than condensation rates during lower obliquity periods, when the ice cap tends to grow. Hence, the ice cap rapidly recedes during the high obliquity portion of the cycle and does not restore water ice lost, during the low portion of obliquity cycle. We suggest that timescales used in this work would be shorter due to this effect. Note that we used Eq. (2.5) to calculate evaporation rates for different obliquities.

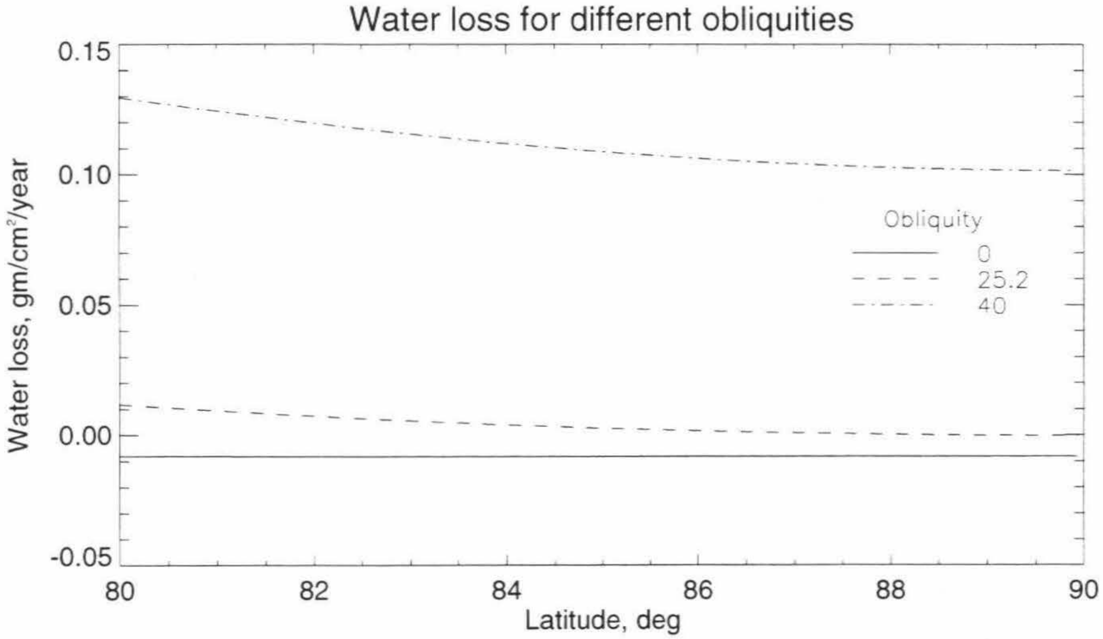

Figure 2.7: Evaporation/condensation rates from the sublimation model runs for Mars' obliquity equal to 0°, 25.2° and 40° as a function of latitude. Model runs were performed assuming surface wind speed of 5 m/s (see Eq. (2.8)). During high obliquity cycles ice evaporates much faster, then it condenses back on the cap during low obliquity cycles.

It is difficult to estimate the possible errors in the calculation of the atmospheric drag coefficient D that have accumulated from the ideas presented here and in the Appendix 2.1. Truly meaningful estimates of the ablation times for a careful comparison with the plastic flow times will require many more measurements (e.g., local wind measurements) on the surface of Mars, and indeed, on the ice caps themselves. However, we firmly believe that the time scale is relatively unimportant for the analysis of the current shapes of the caps and the troughs, the major goal of this paper. Model itself should be developed further to include orbital variations, water cycle, etc.

2.5 Results

2.5.1 General form of the ice cap

The output of the sublimation model is a set of the ice cap profiles as a function of time. We have compared this output with the topography data taken by the MOLA over the ice cap. Four different quadrants were chosen: around 0°E, 90°E, 180°E and 270°E. Selection of these four quadrants will allow us to simulate all types of terrain within the ice cap. For each of these quadrants a profile was taken along the corresponding longitude in the MOLA gridded dataset. The output sublimation model profiles are plotted over the MOLA data in Fig. 2.8.

Note, that two different numbers of model cycles were required to obtain these fits. Same number of cycles was required for quadrants 0 and 180 and a different one for quadrants 90 and 270. We have no explanation for the strong asymmetry of the current residual cap. Some speculative ideas are presented below.

Quadrant 0. This is the most difficult area of the ice cap to explain with any model, because Chasma Borealis cuts through this area. An interesting fact is that the topography profile measured north of 84.5°N latitude is symmetrical across the pole along the 0/180 longitude (see Fig. 2.9). This profile is consistent with the sublimation model results (cycle #155), shown in Fig. 2.8. Slopes in the 80°N-82°N region are consistent with model profile, which requires less cycles (cycle #40, in Fig. 2.9). The central part of the NPIC requires more sublimation model cycles than the south areas of the cap in this quadrant. The part of the ice cap north of Chasma

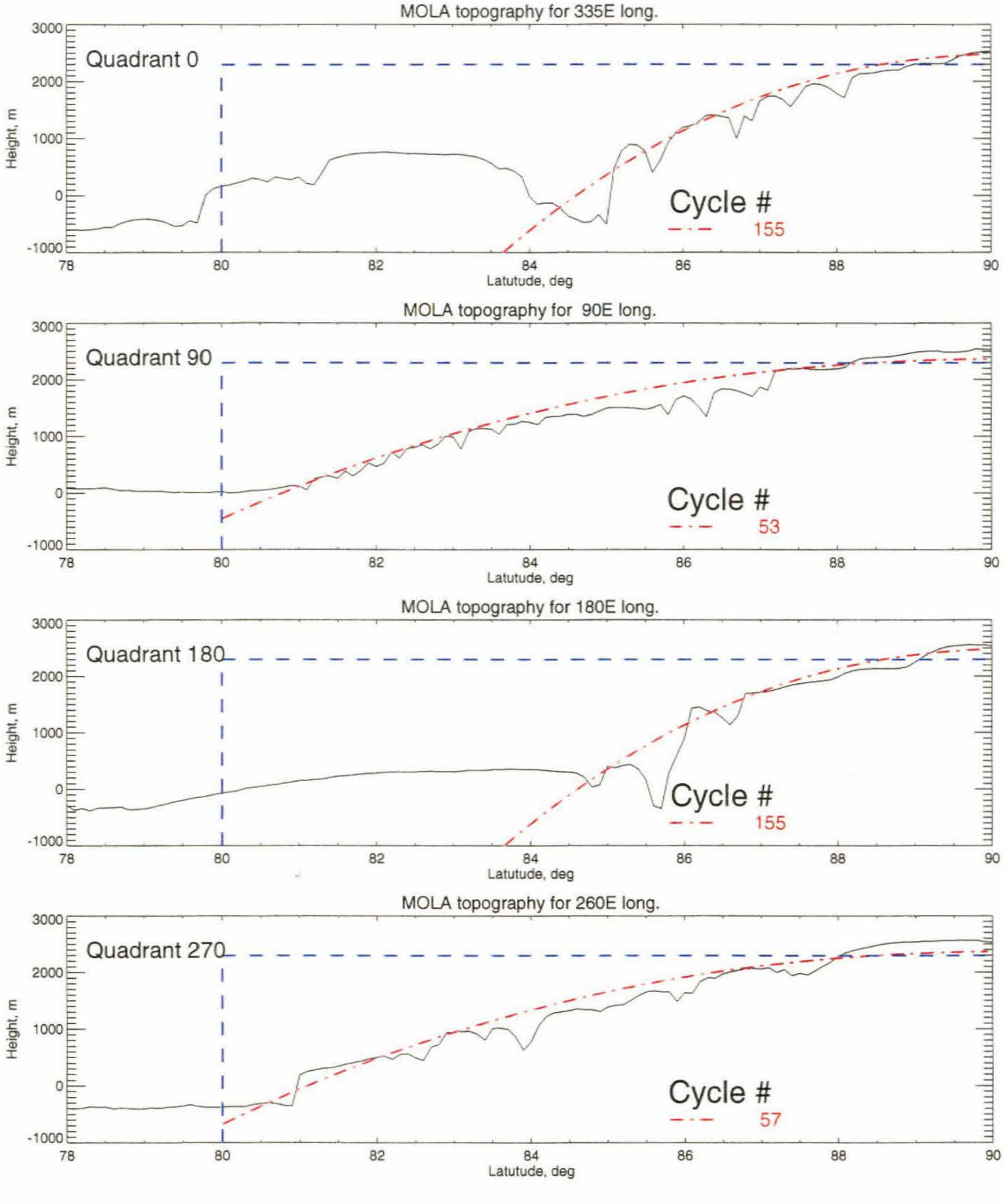
MOLA topography for 335E long.

MOLA topography for 90E long.

MOLA topography for 180E long.

MOLA topography for 260E long.

Figure 2.8: The shape of the ice cap from the sublimation model (dashed red line) over the averaged MOLA data (solid black line). Dashed blue line shows the initial state of the ice cap. MOLA data are taken from the gridded dataset along the corresponding longitudes and downsampled to 0.1° resolution. Origin of areas south of 84°N in quadrants 0 and 180 can not be explained by sublimation model.

Borealis may be older and the south portion may represent a younger ice cap. This cap could be analogous to the offset of the south residual ice cap. This "second cap," suggested by the outer model profile in Fig. 2.9, is also symmetrical to the Olympia Planitia region large dune field. Related to this problem is the plateau, best seen in Fig. 2.3a. It spans roughly 0°E to 60°E along 82°N latitude, about 60km wide. None of the model profiles were able to fit this region. The formation of both regions may be related to some large scale atmospheric asymmetries, which are yet to be discovered. Another hypothesis put forward by Smith et al. (1999a) and Fishbaugh and Head (1999) suggests that cap was actually bigger early in the history. Due to total material loss, the cap shrunk leaving large asymmetries seen near the cap. These asymmetries could also be related to the topography under the ice cap. Notice that in Fig. 2.3 the south edge of the cap is about 500m higher than the Olympia Planitia.

Quadrant 90. This model profile generally fits the surface very well with the exception of the region around 86°N. This is the "plateau" region discussed above. The 53rd cycle of the sublimation model is the best fit to the data and is equal to $53 \times 10 \times F$ Martian years. Since we bounded F in the range between 12×10^3 and 60×10^3 (see discussion in section 2.4), the time scale required for profile formation in this quadrant is between 6.4 and 32 million years. However, sublimation is not the only process responsible for the formation of the shape. We will discuss other factors which might influence the shape in section 2.7.

Quadrant 180. This profile is well represented by the model's 155th cycle. It is the same number of cycles required to the topography profile in the Quadrant 0. Fits in quadrants 0 and 180 were performed independently. This profile is apparently relatively older then the profile in quadrant 90, because of the larger number of cycles in the sublimation model required to fit the MOLA data. Following the logic described in the previous paragraph, we can bound the timescale between 19 and 93 million years.

Quadrant 270. It is very similar and symmetrical to Quadrant 90. However, there is no "plateau" area, except for a terrace between 84°N and 85°N.

We would like to point out again how symmetrical the ice cap is, at least north of 84°N. Figures 2.9 and 2.10 show MOLA data for tracks 404 and 415, which cross the ice cap roughly along longitudes 150°E-330°E and 90°E-180°E respectively and are almost perpendicular to each other. The sublimation model results show (Fig. 2.10) that 60 cycles were required to match the topography (especially outer edges) of the cap from track 415. However, the central part is also consistent with output from cycle #110. Cycle 155 is the single best fit for the track along profile 404 (see Fig. 2.9). Possible explanations from the point of view of the sublimation model are that the central part of the ice cap (north of $\sim 85°$N) was subjected to a different sublimation rate or was formed before the areas south of 84°N down to 80°N. The reasons for both of these explanations are not yet understood.

We stopped cycling the model when the simulated profile matched the measured shape of the ice cap. However, model does not reach a steady state in this case. It will continue to grow ice in the center and to sublimate at the edges. At some point, the cap will become mechanically unstable and start flowing outwards at much faster rates than it currently does. Hence, it will relax to more stable state.

The sublimation model appears to characterize various MOLA cuts across the ice cap very well. However, this is a very simple approach to the problem. We must also consider possible effects of plastic flow, underlying topography and atmospheric asymmetries.

2.5.2 Form of the troughs

In this section I will describe morphological analysis of the troughs, that have been performed using MOLA gridded data set. Previous researchers (Blasius et al. (1982), Herkenhoff and Murray (1990)) employed stereo pairs and photogrammetrical analysis to calculate trough walls' depth and slope. This approach suffered from lack of information about the albedo contrast inside the troughs and could be made for only a limited number of troughs, where stereo images were available.

For our analysis we used MOLA topography grid compiled from passes completed during Science Phasing Orbit and first two months of the mapping orbit (resolution

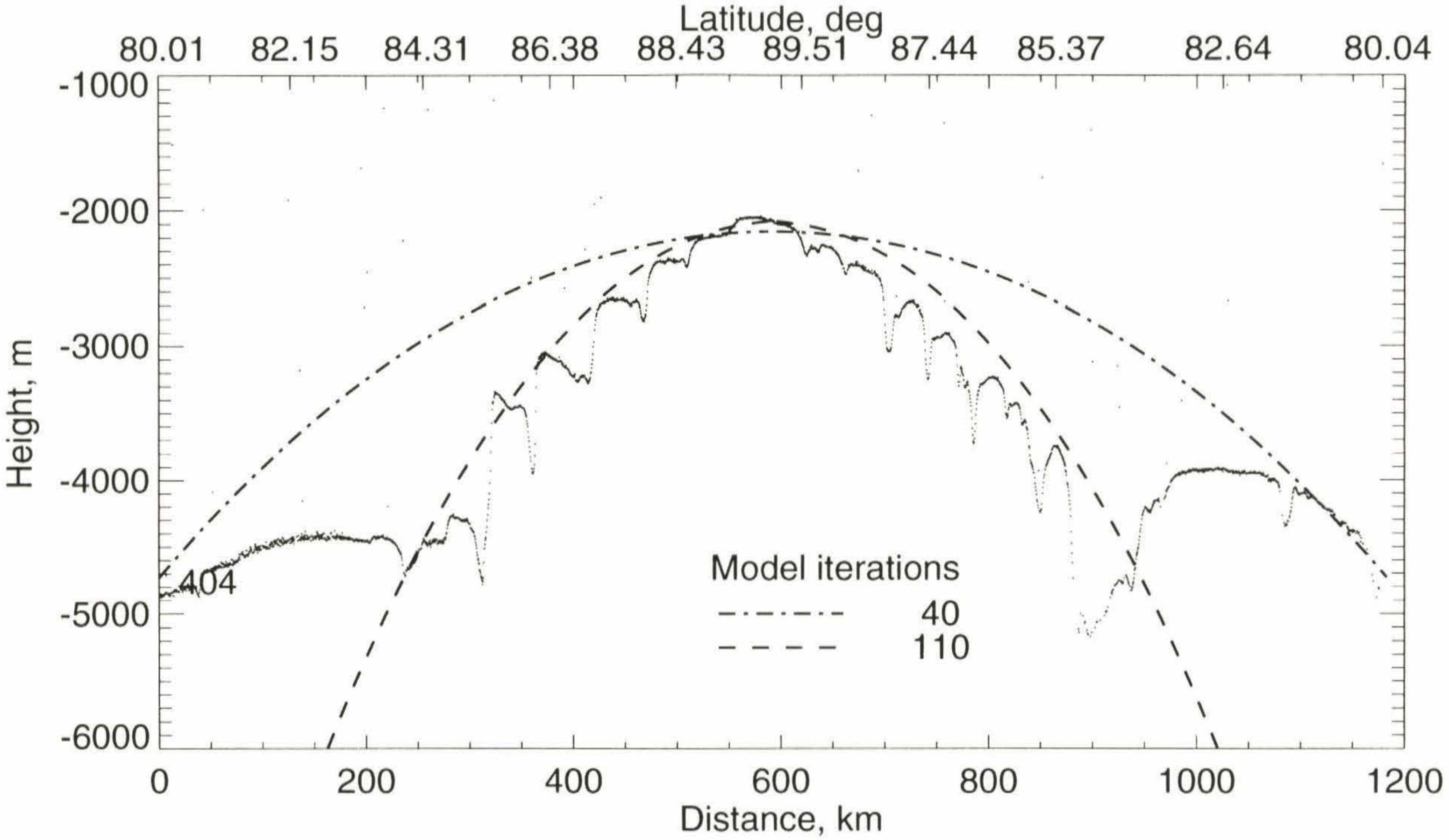

Figure 2.9: Data for MOLA track 404 and the output of the sublimation model (cycles 50 and 155). This track covers same area as averaged data in Fig. 2.8 (quadrants 0 and 180). The central part of the NPIC can be fit by running a sublimation model for 155 cycles. MOLA track 404 was taken right over the pole, when the spacecraft was tilted towards the center of the ice cap. Olympia Planitia is on the left and the ice cap continues all the way to the right side of the graph.

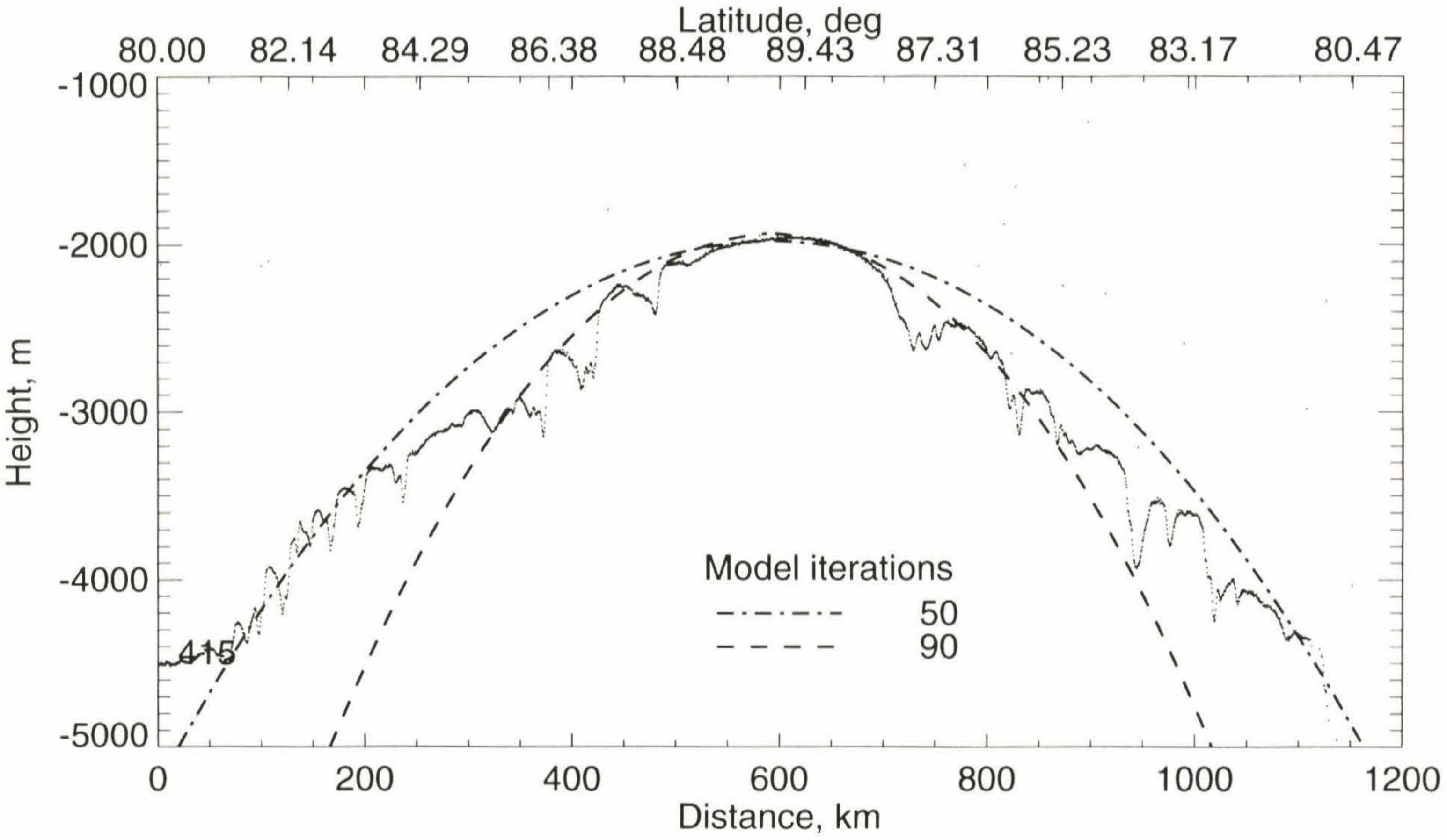

Figure 2.10: Data for MOLA track 415 and the output of the sublimation model (cycles 60 and 110). This track covers same area as averaged data in Fig. 2.8 (quadrants 90 and 270). The central part of the NPIC can be fit by running the sublimation model for 110 cycles, while the edges are consistent with only 60 cycles. MOLA track 415 was taken right over the pole, when the spacecraft was tilted towards the center of the ice cap.

0.75km/pixel). 194 profiles were manually measured across the troughs. They are shown in Fig. 2.11. Profiles were extracted from the grid to measure slope and height of north and south walls. Each trough was approximated as V-shape. It is a good first order approximation, even though many troughs have exhibited complex shapes with a lot of curvature. Two examples of trough shapes are shown in Fig. 2.12. Even though it was hard to define an "average" trough, I have found one that closely corresponds to average parameters of the compiled statistics. It is shown in Fig. 2.12a. This trough is a good example of the structure that can be observed elsewhere. The 100m from the bottom of the trough is bowl shaped, with almost equal slopes on both sides. Then slopes on both north and south sides break. South facing slope increases and north facing slope decreases. A complex trough example (Fig. 2.12b) is located at 86.4°N. It is wider than the "average" slope and exhibits a central hill. This form was suggested by Squyres (1979), arguing that trough movement towards the pole would leave a similar topography signature.

This dataset of trough shapes allowed compilation of some simple statistics on wall slopes and depths. Results are shown in Table 2.2. As expected, the south facing wall (or north wall) is generally higher than the north facing slope (or south wall) and has a larger slope, because it receives more sunlight and hence sublimates more material. The variance is high on all the numbers, which reflects a large variety of slope characteristics. It is very hard to define an "average" trough. Processes that form troughs also differ in magnitude, depending on location of the trough within the ice cap. For example, troughs that are located on the edges of the cap are more likely to be eroded by winds. Troughs that are located inside the ice cap were possibly shaped by sublimation and deposition of the material as well as wind erosion.

	Depth, m	Slope, deg
North slope (south facing)	509 ± 255	4.2 ± 2.6
South slope (north facing)	285 ± 146	1.9 ± 1.1

Table 2.2: Statistical analysis of trough wall depths and slopes on the basis of 194 profile measurements. All numbers are given with corresponding standard deviation.

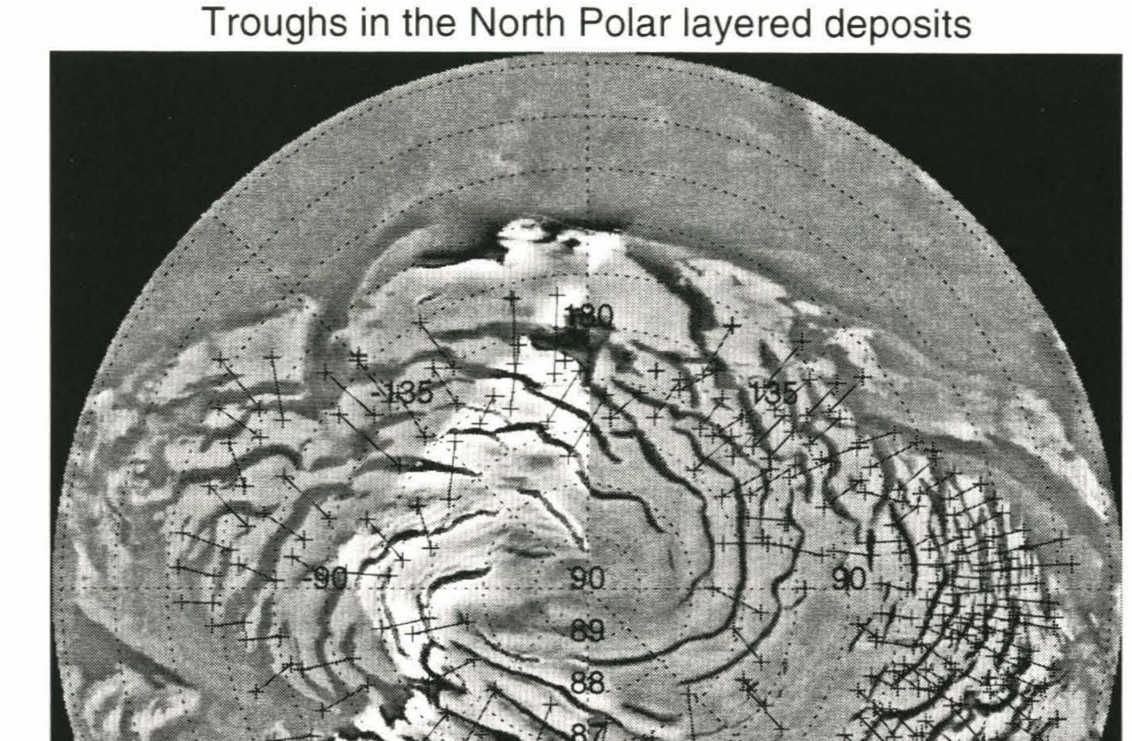

Figure 2.11: Locations of the trough profiles, that were used for the analysis in this work, over the Viking Image Mosaic of the North Polar Region. The image is in polar stereographic projection from 80°N latitude. No trough measurements were available north of 87°N, since there are only 20 MOLA tracks in this region and grid resolution is very poor.

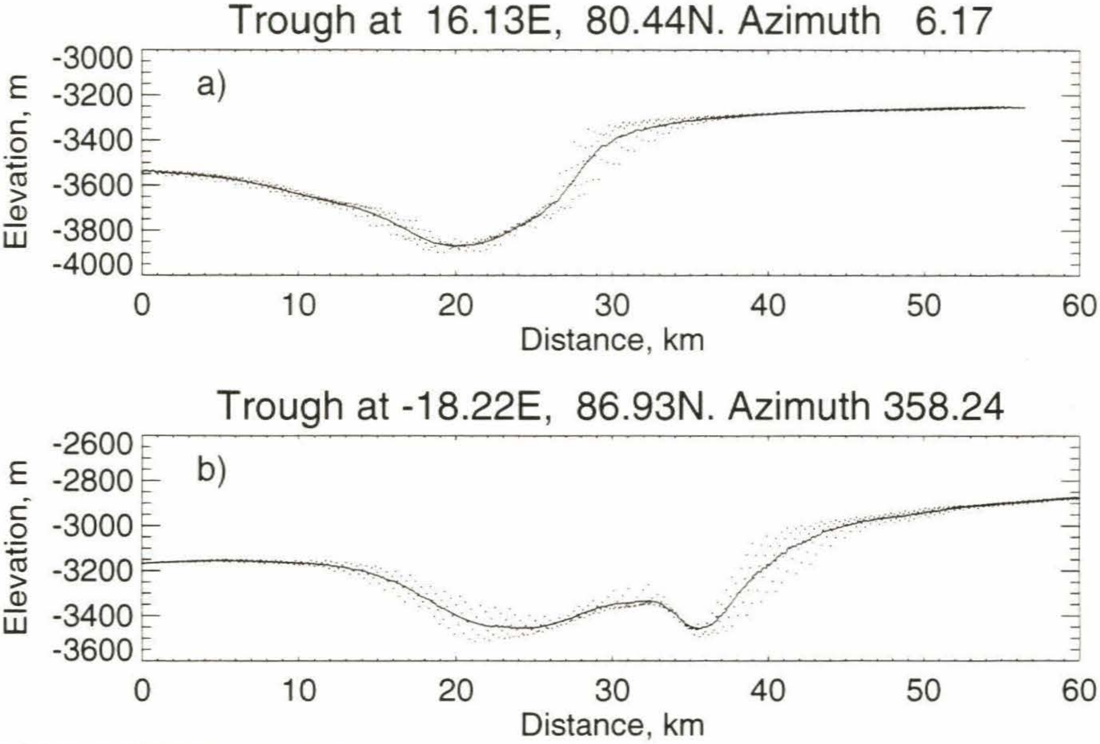

/home/anton/planets/MOLA/PRO 21Jun99 14:24:43

Figure 2.12: Two different trough profiles are shown along with location and azimuth. a) "Average" trough. b) Complex trough. Dots represent topography values from the gridded dataset. Solid line is a smoothed profile of the trough obtained from the grid. Vertical exaggeration 1:15.

The goal of this analysis was to study slope vs. depth relationship and compare it with results from sublimation modeling. Fig. 2.14 displays this relationship and compares observed characteristics of the trough with the results of trough evolution in the sublimation model. It is easy to observe linear trends for both north and south slopes. It is clear that as trough grows deeper, the wall slopes increase on both sides.

Viking Orbiter photographs have shown that troughs have an albedo contrast relative to the residual ice cap due to an enhanced dust/ice ratio in the layered deposits. We introduced such albedo contrasts in our model. At an arbitrary time step of the model the albedo for 3 grid points was lowered by some small amount. Such contrast could have been formed by an atmospheric current depositing dust across the ice cap. Another possibility is that a small trough formed on the ice cap by some other process and acted as a dust trap. Temperatures on grid points with lower albedo were obviously higher and hence the sublimation rates were greater. A distinctive slope structure is also created.

The results of a model with a trough are shown at Fig. 2.13. To create this particular trough an albedo contrast of $0.92 \times A_{ice}$ was used. Due to an albedo contrast, ice sublimates much faster than the rest of the ice cap. We have introduced the albedo contrast at the 70th cycle in this particular case. The output of the 97th cycle is shown in Fig. 2.13. Note that both the overall shape of the cap and the form of the trough are matched very well. Following the discussion in section 2.4 on the factor F, we can bound the time scale for trough formation between 3 and 16 million Martian years. Increased albedo contrast (say $0.875 \times A_{ice}$) will speed up formation of the troughs. Our calculations show that a trough can be formed in only 10 cycles, i.e., almost three times as fast.

Clearly, we can vary the albedo contrast and the exposure time of each particular trough and essentially fit any trough we want. Fig. 2.14 illustrates comparison between the measured parameters of the troughs in the MOLA data with the results of trough growth simulation in the sublimation model. The model can reproduce average depth of the sampled troughs. South facing slopes calculated in the model are quite consistent with an average slope in the MOLA data. The model tends

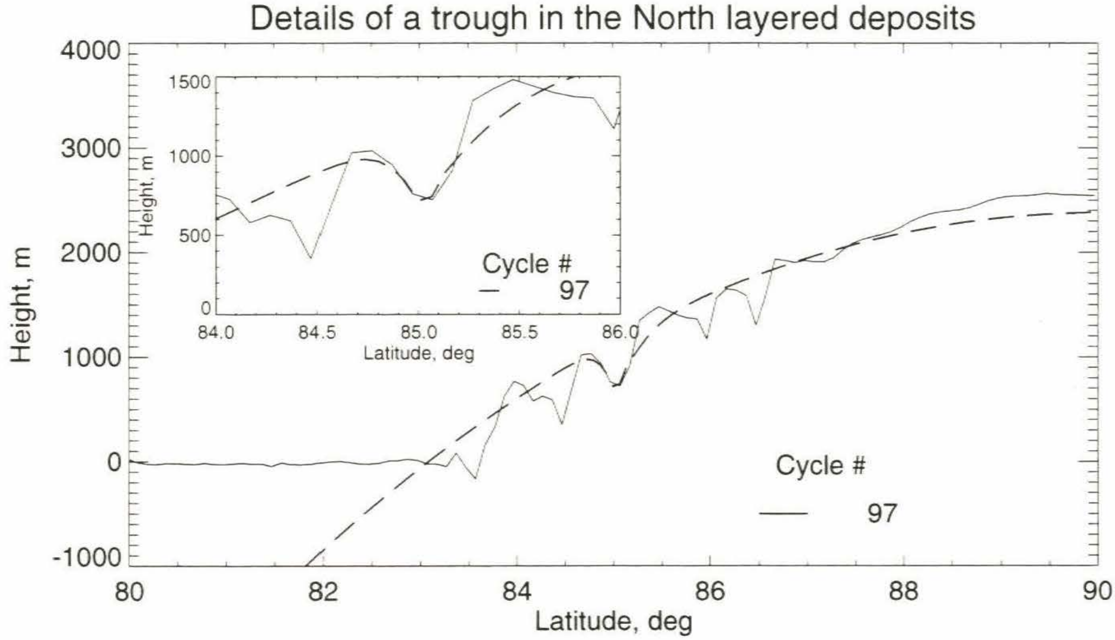

Figure 2.13: Results of the sublimation model run with a trough (dashed line) compared with the MOLA topography (solid line). To create this particular trough an albedo contrast of $0.92 \times A_{ice}$ was used. Albedo contrast was introduced at 70th cycle and was kept in place for 27 cycles. Details of the trough are shown on the insert. Note good agreement of the model output and overall shape of the ice cap.

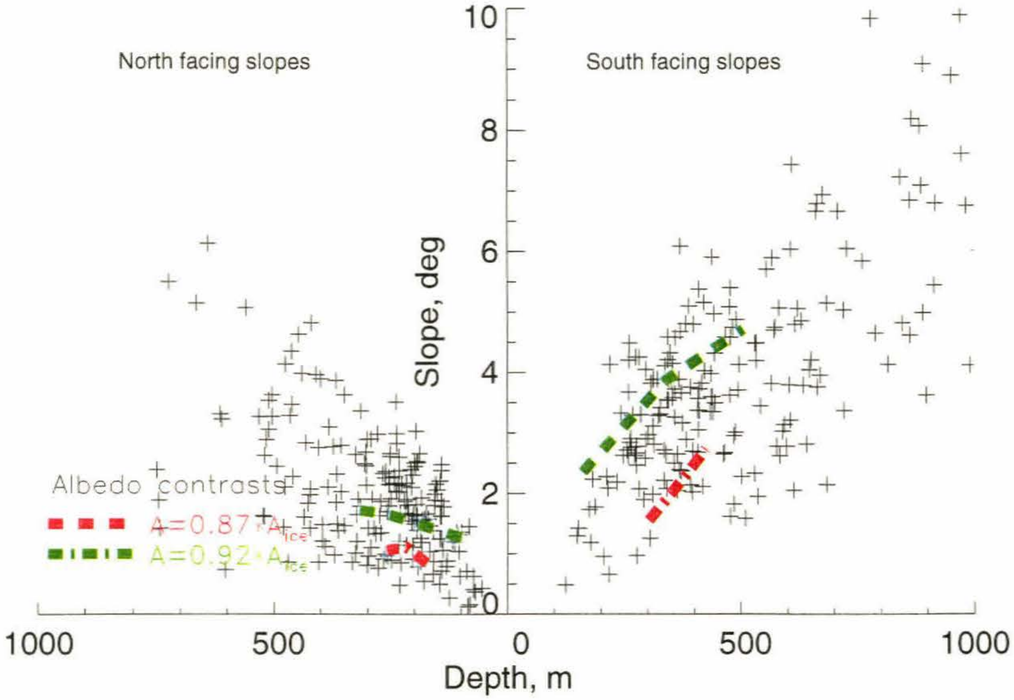

Figure 2.14: Comparison of the main trough parameters measured in the MOLA data and the output of the sublimation model. We varied albedo contrast in the sublimation model. Lines show the modeled slopes and depths for different albedo contrasts and exposure times. Points on the lines are calculated for same albedo contrasts. Time of exposure increases along the line.

to underestimate slopes. This is due to the smoothing algorithm we employ in the program to avoid 90° slopes, which result from subtracting thicknesses of evaporated material at neighboring points on the grid with different albedos. Still the model reproduces the distinction between south facing slopes and north facing slopes quite well. South facing slopes in the model follow the observed general growth trend in the MOLA data.

2.6 Shape of the South Pole Layered Deposits

High resolution topography grids now allow direct comparison of north and south ice caps and layered deposits. First analysis of the southern ice cap and estimates for volume can be found in Smith et al. (1999a). Detailed analysis of the thermal inertia and albedo of the south polar layered deposits (SPLD) is presented in Paige and Keegan (1994). The albedo of the south layered deposits is higher than that of the north polar layered deposits. It is quite likely that SPLD are covered by an insulating layer of dust, which prevents the ice caps from sublimating. Cross section through the centers of both ice caps along 0°-180° longitude are shown at Fig. 2.15. It is apparent that central parts of the ice caps are quite similar in size, at least cuts through this particular longitude. Durham (1998) suggested, based on rheological properties of CO_2 ice, that it is not possible to construct ice CO_2 cap this big. An immediate implication of this comparison is similarity of composition of both ice caps. This conclusion awaits further examination in the laboratory.

We have applied the sublimation model, discussed above, to the Southern ice cap. The results can be seen in Fig. 2.16. The model fits the slopes of the southern ice cap fairly well. The number of cycles (130) required to fit this South polar cap slope is the same as required for the same longitude cut at the North polar cap. The model was not able to reproduce the top of the ice cap and the edge of the cap. The latter is probably due to extensive edge erosion, enhanced by the katabatic winds. Clearly, sublimation models can not be expected to explain 3° offset of the center of the South polar ice cap. We do not know whether this offset is due to a polar wander or details

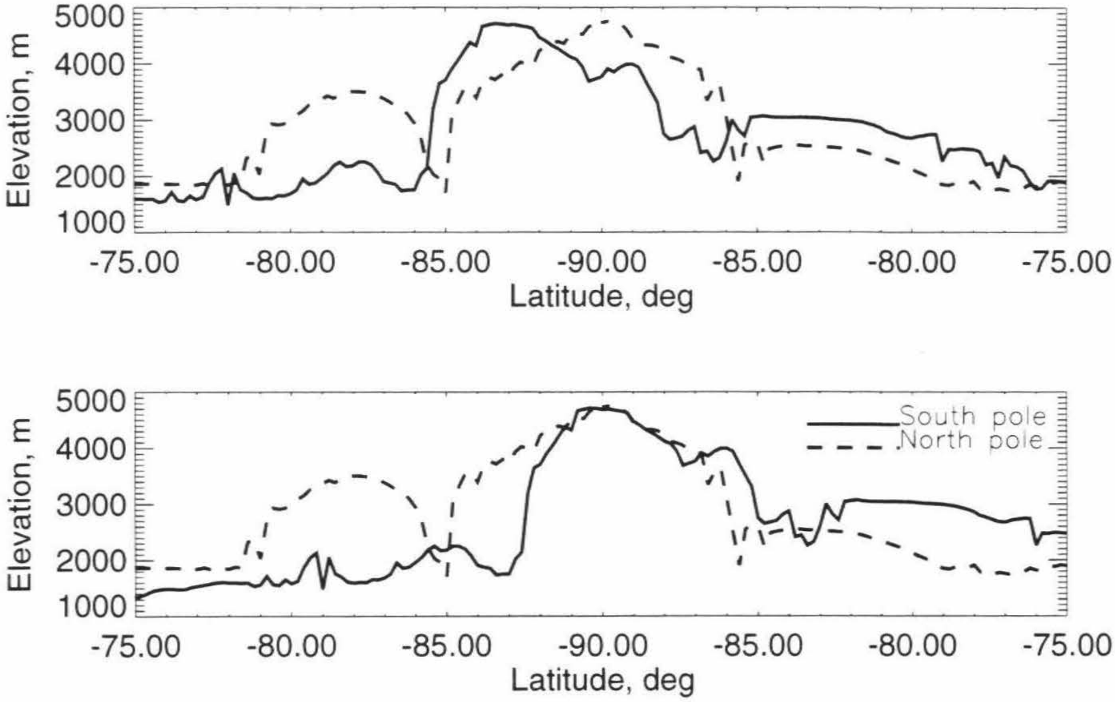

Figure 2.15: Comparison of North and South ice caps topography. South Pole profiles is the solid black. North Pole profile is the dashed line. The upper panel shows relative offset ($\approx$ 3 deg.) of the South polar cap topography maximum from the real pole. On the lower panel, topography of the South polar ice cap is shifted 3° towards the true pole to emphasize similar sizes of the ice caps. The slopes on the edges of the ice caps are very similar. Vertical exaggeration about 100:1.

of the underlying topography under the ice cap or some other large scale process.

Since the NPIC and the South Polar Layered Deposits (SPLD) are similar in size and shape, the results of sublimation model for the NPIC could have been applied for the the SPLD. However, insolation patterns are significantly different. Southern summer is hot and short relative to northern summer. Sublimation rate rises exponentially with temperature. The SPLD sublimate away much faster than the NPIC (in thousands of years vs. millions of years), if we assume the same albedo (0.5) as for the NPIC. The model does not include orbital evolution effects. Timescale for the SPLD sublimation, similar to the NPIC, could have only been achieved raising albedo to 0.6. This is not consistent with the IRTM albedo observations. Albedo of the SPLD is lower, so we can expect higher temperatures on the surface and hence more extensive evaporation. We also know from Viking observations that there is substantially less amounts of water vapor observed over the South Pole than over the North Pole. We know that the thermal inertia of the surface layer of the SPLD is low, suggesting low density material on the surface of SPLD. To prevent water ice from escaping, an insulating layer of dust covers the surface of polar deposits (Toon et al. (1980), Hofstadter and Murray (1990)). Relative age estimates, obtained from craters by Plaut et al. (1988), suggest older ages for the South polar layered deposits, than for the North polar layered deposits. We do not know well composition of the South polar layered deposits, and it is hard to hypothesize on evaporation rates at this point.

2.7 Discussion

We have employed a simple sublimation model to explain the form of the Northern Martian Ice Cap, which was observed by Mars Orbiter Laser Altimeter (Zuber et al. (1998a)). This model only takes into account sublimation and condensation of water ice. We have considered an ideal Martian ice cap overlaying a smooth global sphere, with uniform albedo (except in the troughs). This model does remarkably well at reproducing the current shape of the NPIC and a reasonable job of estimating time

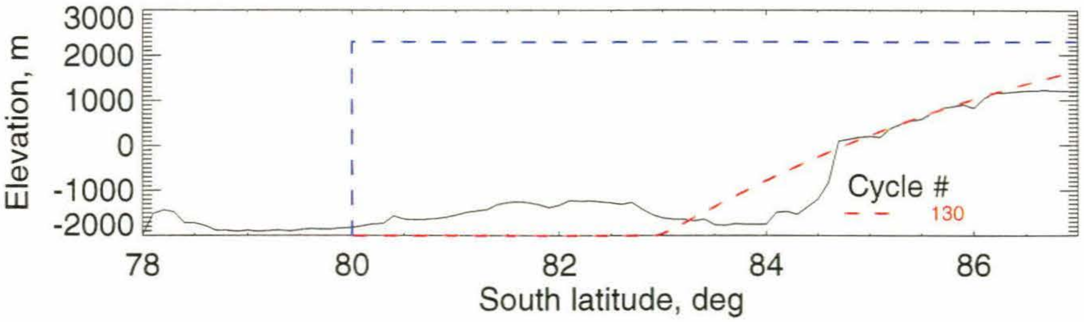

Figure 2.16: Application of the sublimation model to the Southern ice cap. Color code is the same as in Fig. 2.8. Note that MOLA topography data was shifted 3.5 km down. Slope of the Southern ice cap fit the sublimation curve well, which suggests sublimation is important process for the formation of the southern ice cap. The number of cycles (130) required to fit this profile is the same as for the North polar ice cap along the same longitude. In this simulation, the same albedo and orbital parameters as for the NPIC were used. The highest point of the South polar ice cap is shifted about 3° along 10°E longitude.

scales. The model is limited in that a fixed obliquity is assumed over time periods in which orbit evolution was undoubtedly variable. Atmospheric pressures and partial pressures of water ice will be significantly different from what we are observing on Mars now. It is also clear that Mars has gone through epochs of very different atmospheric dust loading and, probably, associated large variations in bond albedo.

The troughs in the NPIC, as cut in all directions by the MOLA tracks, are very distinctive. The details of the troughs and the layered terrains in general were extensively sampled by the MOLA instrument. We analyzed 194 individual trough profiles. Compiled statistics were compared with the simulated troughs in the sublimation model. Observed trough shapes are well explained by our ablation/sublimation model. This offers credibility to the idea that ablation is a more significant mechanism.

On Earth, the sublimation and evaporation of the ice caps is relatively unimportant compared to the flow of ice, ultimately to the oceans. Ice flow and deformation on Mars is considerably less important, since the Martian ice is very cold, mostly less than 200K. Viscous flow models (e.g., Zuber et al. (1998b)), which take into account

H_2O ice rheology at these low temperatures, can reach a reasonable agreement with the topography data. These models have not yet suggested a mechanism for trough formation and evolution. We argue, that sublimation and wind erosion are the two most significant mechanisms for their formation. Nevertheless, the time scales for the two processes - flow and ablation - are sufficiently difficult to estimate with the information about the ice caps we have now. We are prudent that both processes along with the wind erosion are important, but possibly acting on different time scales.

Both the North and South residual Martian polar ice caps show very strong asymmetries. The residual South cap is $\approx 2°$ off the current South Pole. The Northern ice cap has the great feature Chasma Borealis and great dune fields (Olympia Planitia) conjugate to it. These dune fields may rest on a remnant ice deposit, which would restore some symmetry to the NPIC. The asymmetries at both poles are large enough that they must strongly affect the meteorology of the Martian polar regions, possibly supplying feedback that created the asymmetries. In section 2.5 we made a highly speculative suggestion that the current NPIC consists of two caps from different epochs. These two structures are bridged by a ridge of ice or a mountain covered by ice. We have no knowledge about the topography underneath the ice caps. It can strongly influence the asymmetries that we observe. However, the North polar region is very flat and does not have large topographic variations except the ice cap itself (e.g., Zuber et al. (1998a)) and we *might* expect the topography under the ice cap to be flat. Radar investigation of the thickness of the ice will help greatly to remove this uncertainty. Clearly it is not possible to do much more than state these ideas from just the MOLA topography data and sublimation model results. Many more measurements over the coming decade will be required to fully understand the ice caps.

Results of the sublimation model suggest that the Northern ice cap is probably still evolving due to sublimation of ice from its surface. Changes in eccentricty and obliquity in the past may change the duration of north and south summers, so the Southern ice cap is sublimating and Northern ice cap is stagnant under a protective layer of dust. This might be a clue to the layered terrain development. Such protective layer might form from dust that is already in the ice. This dust layer should have some cohesion to be robust against surface winds. The current model lacks full representation of obliquity and eccentricity cycles. We have suggested that the time scale for the evolution of the current shape is bounded by 10-100 million years. We favor the lower bound of this estimate. All the orbital variations are of order of 100s of thousands of years with a long wavelength component of 1-2 million years. Orbital variations lead to significant changes in the climate of Mars and possibly responsible for the formation of the layered terrains. We will include these variations in our model to carry out more reasonable estimates for the time scales of evolution for the Martian polar ice caps and better understand formation of the layered terrains.

2.8 Conclusions

In this paper we present results of an ice sublimation model from the surface of the Northern Martian ice cap and compare them to the form of the ice cap observed by MOLA. In general, the agreement of the model with the overall shape of the cap is quite good. Moreover, we were able to use the same model to produce satisfactory trough shapes. We argue that sublimation is an important process for the formation of ice caps as well as plastic flow and wind erosion. Sublimation is faster than the flow, but they both must be important. Combined effect of all three processes on the form of the cap is yet to be investigated. We have also addressed the question of the formation time scale of the ice caps and troughs. Many meteorological parameters relevant to the evaporation of ice are known for Earth and practically unknown for Mars. We were able to bound the time scale for the formation of the ice cap (using values measured on Earth) somewhere between 5 - 100 million years, and we think that it is closer to the lower bound of this range. The time scale for the formation of troughs is shorter and is about 1 - 16 million years. More precise estimates of the time scales require measurements of the meteorological properties of the surface as well as continuous observations of water vapor distribution and winds over the ice cap. We hope that the future Mars missions will help us to answer these questions.

Appendix 2.1

Convection of the water vapor

We now present arguments for the use of Eq. (2.5) for the Martian ice cap. The subject of a turbulent layer on a boundary surface and its effects on sublimation and evaporation is remarkably complex and is well documented in the literature. Our line of argument most nearly follows that presented by Paterson (1994) which considers meteorological effects on the Earth's ice deposits. Our discussion also has a strong dependence on Peixoto and Oort (1992), Priestley (1959), and Brutsaert (1965), Brutsaert (1982). Eq. 2.1 is, of course, useless for the consideration of evaporation and sublimation of water from ice surfaces in contact with the heavy atmosphere of the Earth. The transport of water from surfaces on the Earth is driven by wind turbulence and buoyancy effects which completely dominate over molecular diffusion. Laboratory and field measurements under a reasonably wide range of meteorological conditions suggest that the eddy diffusion of vertical momentum, sensible heat and water vapor are similar and occur at about the same rates. The surface pressure on the Mars surface is about 6 mb, which scales to an altitude on the Earth of about 35 km! However, measurements on the Viking Landers as reported by Tillman et al. (1994) suggest that the wind and turbulence parameters on Mars are at least similar to those on the Earth's surface. The purpose of this appendix is to review the theoretical and empirical developments of these ideas and to apply them to the ablation problem for the Mars NPIC. The fundamental idea presented in all the references listed above is that the transport equation for momentum, sensible heat and water vapor are similar in the convective region. Following Paterson (1994) we consider these equations in our context. This development can not be done rigorously but rather depends on laboratory and field measurements on the Earth's surface.

The shear stress τ can be written

$$\tau = K_m \rho \frac{\partial u}{\partial z}, \tag{2.11}$$

where ρ is the fluid density, u the velocity, z the vertical coordinate and K_m is the eddy viscosity. Since ρu is the momentum per unit volume, this equation represents the vertical transport of momentum. The heat per unit volume can be written $\rho c_p T$, where c_p is the specific heat at constant pressure and T is the local temperature of the fluid. Then the heat flux per unit area is

$$F_h = -K_h \frac{\partial T}{\partial z}, \tag{2.12}$$

where K_h is the eddy diffusion coefficient for sensible heat, orders of magnitude larger than the molecular thermal diffusivity. Writing ρ_w as the mass of water vapor per unit area, the transport equation for water vapor can be written

$$F_w = \frac{dM}{dt} = K_w \frac{\partial \rho_w}{\partial z}, \tag{2.13}$$

where K_w is the eddy diffusion coefficient for the water vapor.

Laboratory experiments and field tests on Earth (usually made at 1 bar) show the these bulk transport coefficients are nearly equal and we will use

$$K_w = K_h = K_m. \tag{2.14}$$

We can use the ideal gas law for the water vapor and the CO_2 atmosphere on Mars and write the partial pressures

$$p_w = \frac{R}{\mu_w} \rho_w T \quad and \quad p = \frac{R}{\mu} \rho T, \tag{2.15}$$

where R is the universal gas constants. From Eq. (2.14) and Eq. (2.15)

$$\rho_w = \rho \frac{\mu_w}{\mu} \frac{p_w}{p}. \tag{2.16}$$

Eq. (2.13) becomes

$$F_w = K_m \frac{\mu_w}{\mu} \frac{\rho}{p} \frac{\partial p_w}{\partial z}, \tag{2.17}$$

where the derivative of ρ/p (essentially T) is neglected since this term is slowly varying with z. The diffusion transport coefficients depend on turbulence created by winds flowing over the surface which has finite roughness. K_m is estimated using the following arguments:

Experimental results show that the ratio τ/ρ is nearly constant with height and that a friction velocity u_* can be defined

$$u_* = \sqrt{\frac{\tau}{\rho}}. \tag{2.18}$$

The massive empirical evidence supports the equation for the fluid speed variation with height (see the references cited above).

$$\frac{u}{u_*} = \frac{1}{k_0} ln(\frac{z}{z_0}), \tag{2.19}$$

where k_0 is van Karman's constant ≈ 0.4 and z_0 is the roughness parameter of the particular surface and is equal to the thickness of the boundary sublayer. On Earth surfaces z_0 ranges from about 0.1 to 3 cm and there is no reason to believe that these are not reasonable values for the ice surfaces on Mars (Tillman et al. (1994)). However, at this time we have no information on the roughness of the Martian ice surfaces, but the Viking landing sites (which were not on ice) display the same range of values. We can then write, using Eq. (2.11) and Eq. (2.19),

$$K_m = \frac{\tau/\rho}{\partial u/\partial z} = u_* k_0 z, \tag{2.20}$$

as an estimate of the water vapor transport coefficient K_w. Eq. (2.17) for the water vapor flux can be written

$$F_w = \frac{\mu_w}{\mu} u_* k_0 \frac{\rho}{p} \frac{\partial p_w}{\partial (ln z)}. \tag{2.21}$$

We can approximate this equation with a difference equation of the form

$$F_w = \frac{\mu_w}{\mu} u_* k_0 \frac{\rho}{p} \frac{(p_{H_2O}(z) - p_{sat})}{ln(z/z0)}, \tag{2.22}$$

where the difference is taken from the upper edge of the laminar layer, z_0, to height z, p_{H_2O} is the partial pressure at z and p_{sat} is the saturation vapor pressure of water at the temperature within the laminar layer at z_0. That is, we assume that the water vapor at the surface remains saturated. We get the final form of our result by using Eq. (2.19) for u_*, defining A (after Paterson (1994), Priestley (1959) calls it the drag coefficient) as

$$A = \frac{k_0^2}{ln(z/zo)^2}. \tag{2.23}$$

Typically, $A = 0.002$ for icy surfaces on Earth and we accepted the same value for Mars. Using the equation of state for the CO_2, Eq. (2.15),

$$F_w = \frac{dM}{dt} = \frac{\mu_w}{RT} Au(p_{H_2O}(t) - p_{sat}(T)). \tag{2.24}$$

A similar analysis for the heat transport equation leads to

$$F_h = \rho c_p Au(T(z) - T_s). \tag{2.25}$$

Equations 2.24 and 2.25 have been extensively tested on the Earth and hold up well. It is reasonable to expect the situation to be the same on Mars if the roughness parameter can be bounded for the NPIC region. Equation 2.24 says that the sublimation from the surface depends on the difference of the saturation vapor pressure at the surface and the partial pressure of the water vapor just above that layer. It depends further on some velocity u. If that velocity were a kinetic theory velocity for the case of the vapor above ice in vacuum such as

$$u = const\sqrt{\frac{kT}{m_w}}, \tag{2.26}$$

where k is Boltzmann's constant and m_w is the mass of a water molecule, Equation Eq. (2.24) becomes

$$\frac{dM}{dt} = const A(p_{H_2O} - p_{sat})\sqrt{\frac{m_w}{2\pi kT}}, \tag{2.27}$$

which is our Eq. (2.5) in the main text.

Acknowledgments We wish to thank Andrew Ingersoll for many discussions on these matters and an introduction to the literature. We greatfully acknowledge the entire MOLA team for the fine instrument and the excellent operation of the instrument, data calibration and reduction. We are thankful for numerous discussions with the MOLA team members, particularly Dave Smith and Maria Zuber. Comments from James Cutts and an anonymous reviewer are greatly appreciated. We also thank Alexander Basilevsky and Misha Kreslavsky for useful discussions. This work was supported by NASA Grant NAG5-4437.

Chapter 3 Polar night clouds

Formation of the perennial ice caps is one of the most important climatic processes on Mars. Up to 25% of the atmosphere is recycled each year trough the ice caps. CO_2 ice may form on cold surface when temperatures are low enough ($\sim 146K$) or condense in the atmosphere and fall down on the surface as snow. Condensation of CO_2 had not been quantified or observed in any significant detail. Radiative properties of CO_2 clouds are poorly known at this point. However, clouds play an important role in the radiative budget of the Martian atmosphere. This chapter will describe observations of CO_2 clouds during the polar night by the Mars Orbiter Laser Altimeter (MOLA). We will present observations of cloud heights and their locations for North and South polar winter regions. Backscattering coefficient for the cloud tops can be calculated from the reflected energy and pulse width measurements. The calculated values are similar to those of Earth's high altitude clouds. Comparison with the MGS Thermal Emission Spectrometer (TES) brightness temperature data suggests that the anomalously low brightness temperatures in TES and Viking IRTM data can be explained by CO_2 snowfall or freshly formed snow.

Parts of this work were presented as an invited talk at XXIV General Assembly of the European Geophysical Society (Ivanov and Muhleman (1999b)) and at the 5th International Mars Conference (Ivanov and Muhleman (1999a)).

3.1 Introduction

Clouds in the Martian atmosphere are one of the most interesting variable phenomena. They play an important role in the radiative balance of the planet's atmosphere. Clouds were seen from orbit by Mariner 9 and the Viking Orbiters. There are also ground based observations by the Viking Landers and the Pathfinder. Most of the reported clouds were observed during the local daytime with conventional techniques, such as imaging and spectroscopy. The observed clouds most probably are composed of the condensing water vapor. Temperatures are too high during the day time on Mars to form thick CO_2 clouds. The latter can only form during the polar night, when the temperatures are the lowest.

In this chapter we will discuss first detection of the polar night clouds with the MOLA instrument. This detection was somewhat anticipated but still surprising. Along with the cloud height, MOLA measured the reflected energy and the returned pulse width. We will describe observations of the polar clouds and cloud opacities in the North and South polar regions in sections 3.4 and 3.5. A cloud reflections model and the calculation of the backscattering coefficient will be presented in section 3.6. We will describe comparison of the backscattering coefficient measured for Martian clouds with values for some Earth clouds distributions. The MGS Thermal Emission Spectrometer (TES) instrument has performed observations at the same time with the MOLA instrument. We will discuss comparison of MOLA and TES data in section 3.7.

3.2 Previous work

CO_2 ice clouds were first suggested by Gierasch and Goody (1968), further studied by Paige (1985) using a one-dimensional polar radiative transfer model. They are briefly described in the review of the global CO_2 cycle by James et al. (1992). A recent review by Forget (1998) discusses recent advances in modeling CO_2 condensation rates during the polar night. Pierrehumbert and Erlick (1998) offered some analysis of the impact of CO_2 cloud cover on the greenhouse effect for the Martian atmosphere. They suggested CO_2 clouds reflected outgoing thermal radiation back to the surface and warmed up the atmosphere of early Mars.

A direct observation of CO_2 clouds was made by the Mariner 6 and 7 infrared spectrometers (Herr and Pimental (1970)); three bright limb crossings yielded spectra with a spike at 4.26 μm which was attributed to reflection in the strong ν_3 band from solid CO_2 at $\approx$ 25 km altitude. However, the range of occurrence of CO_2 clouds was highly uncertain. The Viking Infrared Thermal Mapper (IRTM) instruments found areas in the winter polar regions with anomalously low brightness temperatures at 20-μm wavelength, some below 135K (Kieffer et al. (1976b)). The location and brightness temperatures of these areas sometimes varied on the scales of days, suggesting complex physical processes. Kieffer et al. (1977) have suggested three hypotheses to explain these anomalously low brightness temperatures. They include (1) a strong enrichment in lighter, non-condensible gases in the winter polar atmosphere allowing the partial pressure of CO_2 to be less than that at low latitude: (2) low emissivity of the frost, formed on the ground and (3) the presence of the clouds. The latter hypothesis was also investigated by Forget et al. (1998), suggesting that the IRTM instrument observed a snowfall on Mars. The mapping campaign during the Mars Global Surveyor mission allowed simultaneous observations of both poles by MOLA and TES (Thermal Emission Spectrometer) instruments. The TES team has reported low emission zones, similar to the ones observed by the Viking IRTM instrument. We present comparison between MOLA cloud observations and TES low brightness temperatures regions in section 3.7.

3.3 Instrument description

Before we discuss observations of the clouds, we would like explain how the MOLA instrument measures reflected energy and the returned pulse width. This section contains information from Zuber et al. (1992) and Abshire et al. (1999). We advise the reader to refer to these two sources for more detail.

The MOLA laser operates at the wavelength of $1.064\mu m$. Pulses are emitted with a repetition rate of 10Hz. Ranging schematic is shown in Fig. 1.1. The output laser pulse energy (E_0) is determined by optically sampling the center portion of the laser exit beam via transmission optics and passing the signal through an energy monitor. The output of the start detector acts to initiate the range timing process by starting the TIU (Time Interpolation Unit). The received laser pulse, after being focused by the telescope's mirrors is directed onto a silicon avalanche photodetector (Si APD). After passing through a low-noise preamplifier, the received signal passes through a parallel bank of four low-pass filters. In this work, we will refer to these filters as channels. These filters have approximately Gaussian shapes and are matched for received pulse widths of 20, 60, 180 and 540 ns (Table 3.1). The widths of these matched filters were selected to optimize probabilities for Mars footprint-scale surface slopes of 1.7°, 5°, 15° and 39°. All the slopes from 0° to greater than 39° will be detectable with various probabilities. If any of the filter outputs exceeds the specified detection threshold within the range gate (c.f. Fig. 1.1), the signal triggers a voltage comparator circuit, which stops the time-of-flight measurement. The received energy (E_r) of the channel that stops the TIU and the returned pulse width (time when filter output was over the threshold) are measured by a second energy monitor and subsequently reported to the MOLA packet data via the flight computer. The transmitted and received energies are measured with 2% resolution.

Characteristic	Channel			
	1	2	3	4
Description	smooth	moderate	rough	scarp or cloud
Channel width, ns	20	60	180	540
Terrain height variation within the footprint, m	3	9	27	81
Footprint-scale surface tilt, deg	1.1	3.3	9.8	27.0
Probability of measurement	.9	.9	.5	.1

Table 3.1: MOLA Matched Filter Characteristics (adapted from Zuber et al. (1992))

The shape of the returned waveform carries information about the footprint-scale roughness of the surface. Flat surfaces would exhibit a narrow waveform. Rough, sloping surfaces yield broad waveforms with low peak powers. Atmospheric layers are diffuse reflectors; backscattered laser energy from such features would be considerably spread in time and would be detectable with the MOLA's widest filter (channel 4). However, in the mapping mission observations, discussed in the next section, MOLA has detected unambiguous cloud returns in channel 1. It would be extremely beneficial to obtain waveforms of the cloud returns. Strict power and data returned constraints on the MGS spacecraft did not allow implementation of a waveform digitizer in the MOLA instrument. A sister instrument to MOLA, Shuttle Laser Altimeter (SLA-02), has a waveform digitizer. We will discuss some examples of returns from an ocean surface and from the cloud in section 3.6.

3.4 Observations

During Science Phasing Orbits and the Mapping period (see Table 2.1), MOLA was able to perform observations during both north and south polar nights. Numerous reflections above the ground were detected. Many of them can be classified as clouds, providing direct observational evidence of clouds during the Martian polar night. Orbit characteristics were completely different during the above two observational periods. Coverage was significantly better during the South polar night and the Northern fall periods (mapping orbits) due 2 hr orbit instead of 12 hr orbit during the north polar night (SPO orbits). Figs. 3.3 and 3.5 (to be discussed below) display spatial distributions of the cloud echoes over the North and South Pole respectively. The most extensive cloud formations at both poles are confined to the region over the residual ice caps. A small number of clouds can be associated with topographic features (such as craters) off the ice caps. MOLA detected extensive cloud formations just off the south polar layered deposits, in the 70°S-80°S latitude band (see below).

Fig. 3.1 illustrates the occurrence of the clouds as a function season on Mars. The number of cloud returns is binned in 1° of L_s for both SPO and Mapping observation

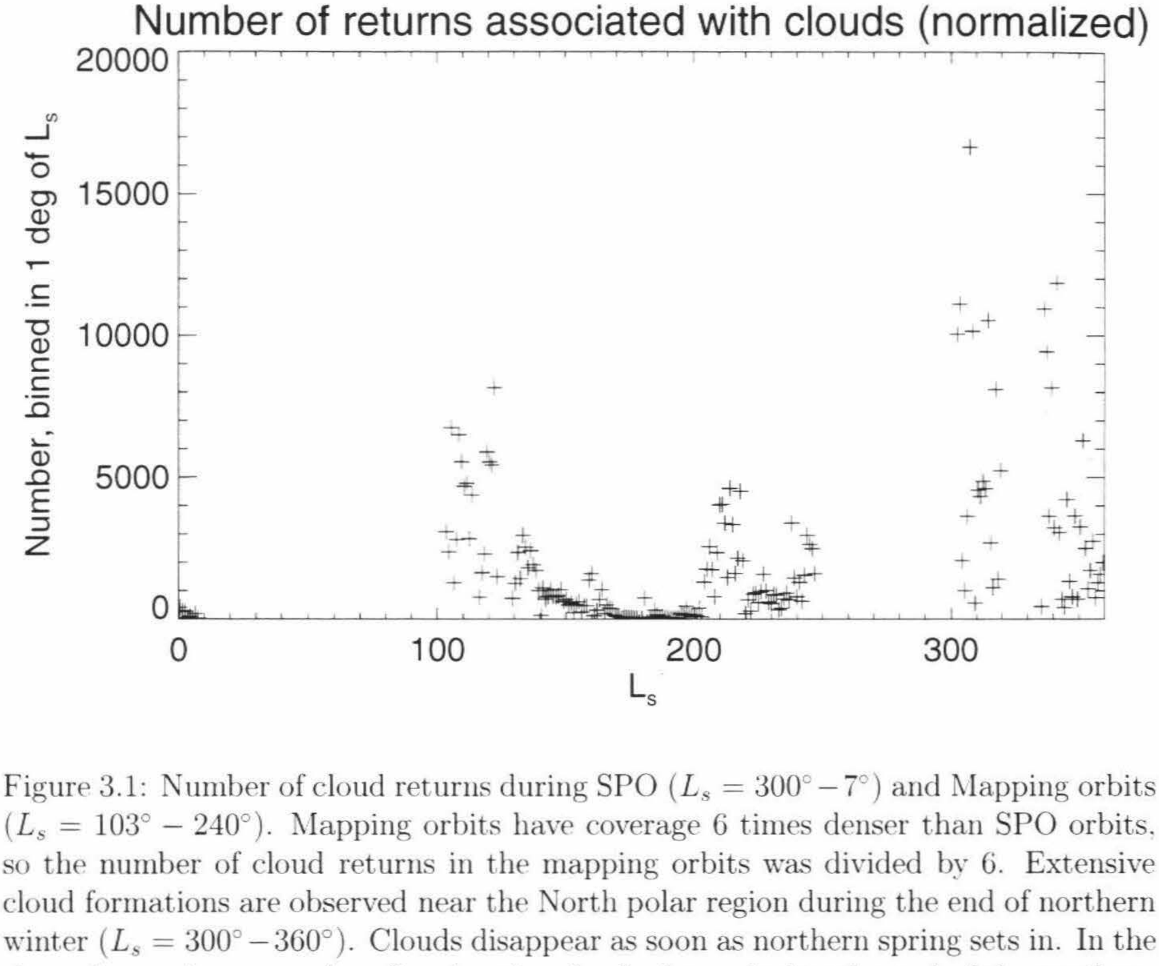

Figure 3.1: Number of cloud returns during SPO ($L_s = 300° - 7°$) and Mapping orbits ($L_s = 103° - 240°$). Mapping orbits have coverage 6 times denser than SPO orbits, so the number of cloud returns in the mapping orbits was divided by 6. Extensive cloud formations are observed near the North polar region during the end of northern winter ($L_s = 300° - 360°$). Clouds disappear as soon as northern spring sets in. In the time of mapping campaign, South polar clouds decay during the end of the southern winter. Clouds reappear over the North pole after $L_s = 195°$. Note that the start of the dust storm season ($L_s = 220°$) coincides with a drop in number of cloud returns.

periods. The number of returns during the Mapping mission is divided by 6, to account for a denser coverage. The periapsis altitude was twice as low for the SPO orbit ($\sim$ 200km) than for the Mapping orbit ($\sim$ 400km). Moreover, the periapsis location drifted slowly near the North Pole of Mars during the SPO orbit. In other words, the lowest point of the orbit was right over the pole, which created preferential conditions for cloud observations. We did not adjust this graph for possible difference in number of cloud returns due to different altitudes of periapsis. The most extensive cloud formations were observed over the North polar ice cap in the end of the northern winter ($L_s = 300° - 360°$). From the start of the mapping observations ($L_s = 103$) to the end of the southern winter, MOLA detected extensive cloud formations in the South polar region, especially over the South polar layered deposits. Practically, no clouds have been observed in the south polar region after $L_s = 150°$. Clouds reemerge over the North polar region around $L_s = 195°$. They exhibit same structure and reflective properties as clouds, observed in the end of the northern winter. Cloud densities drop significantly right after the start of the dust storm season ($L_s = 220°$). The atmosphere warmed up due to the presence of dust lifted by the dust storm and higher temperatures prevent forming CO_2 clouds. Now we introduce a cloud classification based on reflective properties and location patterns.

Latitudinal and height distribution of clouds are shown in Fig. 3.2. Colors represent returns in channel 1 (black) and channel 4 (blue). Data used to construct this picture covers the north and south winters. It can be clearly seen that most of the channel 4 cloud returns are observed poleward of 80° for both poles and those are returns from type 1 clouds. Polar clouds are the highest in altitude and from near the ground all the way up to 15km in absolute elevation over the reference ellipsoid. Sharp returns in channel 1 (type 2) are observed in the latitude band from 70° to 80°N. Type 2 clouds are generally observed closer to the ground and they are spread in altitude from the ground up to about 7 km. Table 3.3 has statistics on how many returns were registered in each of the 4 channels for both types of clouds. In the following sections, we detail observations of the clouds for North and South polar regions separately.

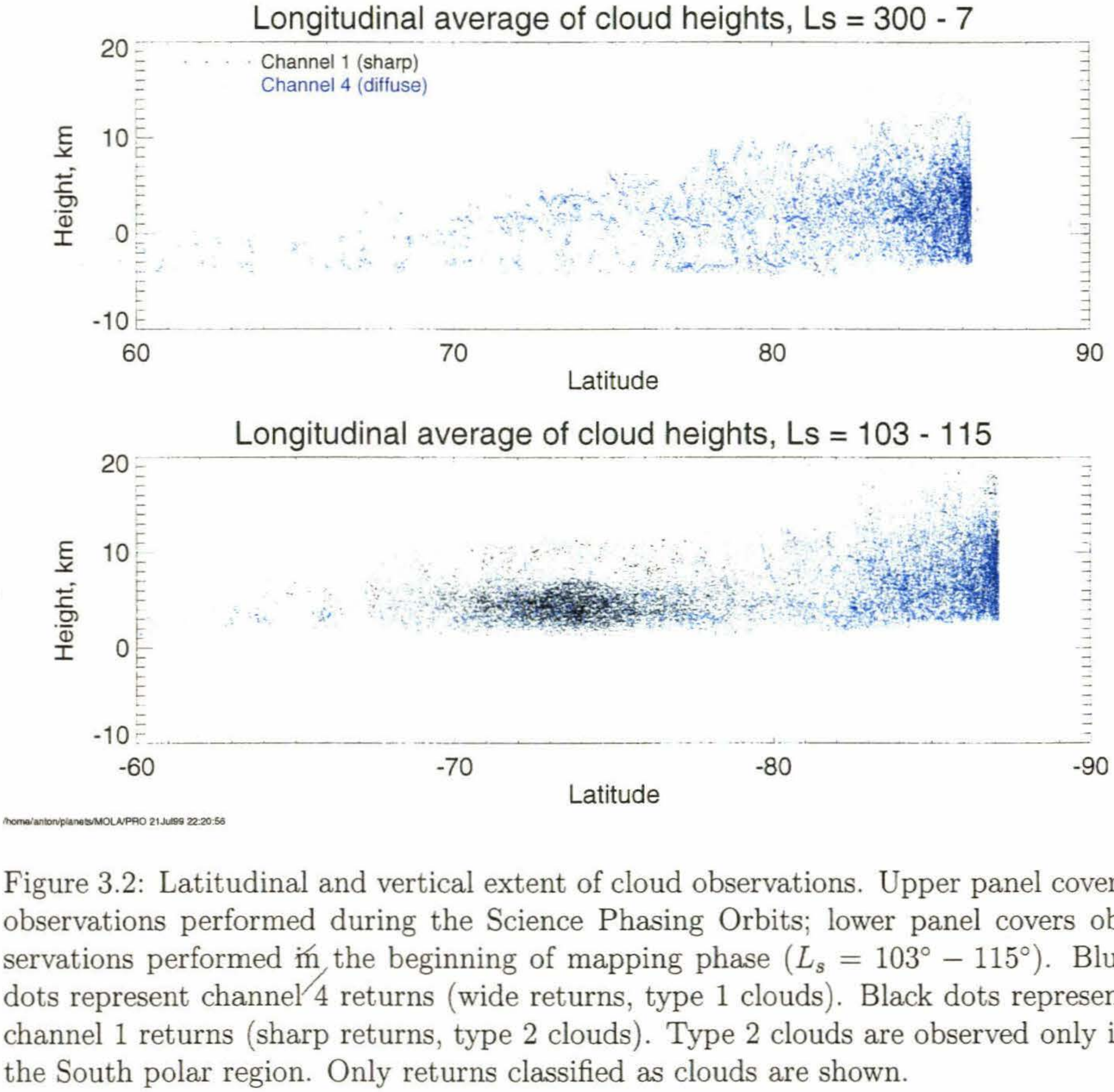

Figure 3.2: Latitudinal and vertical extent of cloud observations. Upper panel covers observations performed during the Science Phasing Orbits; lower panel covers observations performed in the beginning of mapping phase ($L_s = 103° - 115°$). Blue dots represent channel 4 returns (wide returns, type 1 clouds). Black dots represent channel 1 returns (sharp returns, type 2 clouds). Type 2 clouds are observed only in the South polar region. Only returns classified as clouds are shown.

3.4.1 North Polar Region

Cloud observations in the North polar region were performed from $L_s = 300°$ to $L_s = 7°$ in the SPO period and from $L_s = 195°$ to $L_s = 240°$ in the mapping period. During the SPO period, MGS orbit had a period of 12 hours with periapsis near the North Pole. This created a perfect opportunity for night cloud detections, since the link margins were the highest over the North Pole. Clouds can be unambiguously identified as a group of individual returns (usually more then 10) over the ground level that came within 0.2 sec from each other. The clouds are very diffuse structures. Usually the returned pulse width is very wide and channel 4 triggers. We will call these clouds "type 1 clouds." Type 1 cloud tops are diffuse, averaged over the footprint. In the South polar region, MOLA detected a large number of returns, when channel 1 triggered to a signal from a cloud. We call them "type 2" clouds and they will be discussed in the next section.

Summary of north polar night cloud observations is shown in Fig. 3.3. Most of the returns are concentrated over the North residual ice cap. Details of a cloud structure from orbit 222 are shown on Fig. 3.4 . The linear sawtooth structure, clearly seen on many passes, is possibly formed by alternating condensation and evaporation of $C0_2$ gas, due to temperature variations in the propagating wavefronts. To explain this structure Pettengill and Ford (1998) suggested gravity waves which follow a dry CO_2 ice adiabat (-4.3K/km). Water ice and dust particles may serve as nucleus for condensation.

During the mapping orbits, first clouds appeared in the North polar region after $L_s = 195°$. Their reflectance properties and spatial structure were very similar to those observed during the SPO observations. Intensity of cloud formation dropped significantly after the dust storms started ($L_s = 220°$). As the season progressed towards the Martian winter, cloud locations moved south of the residual ice cap. At $L_s = 240°$ cloud returns were detected as far south as 72°N.

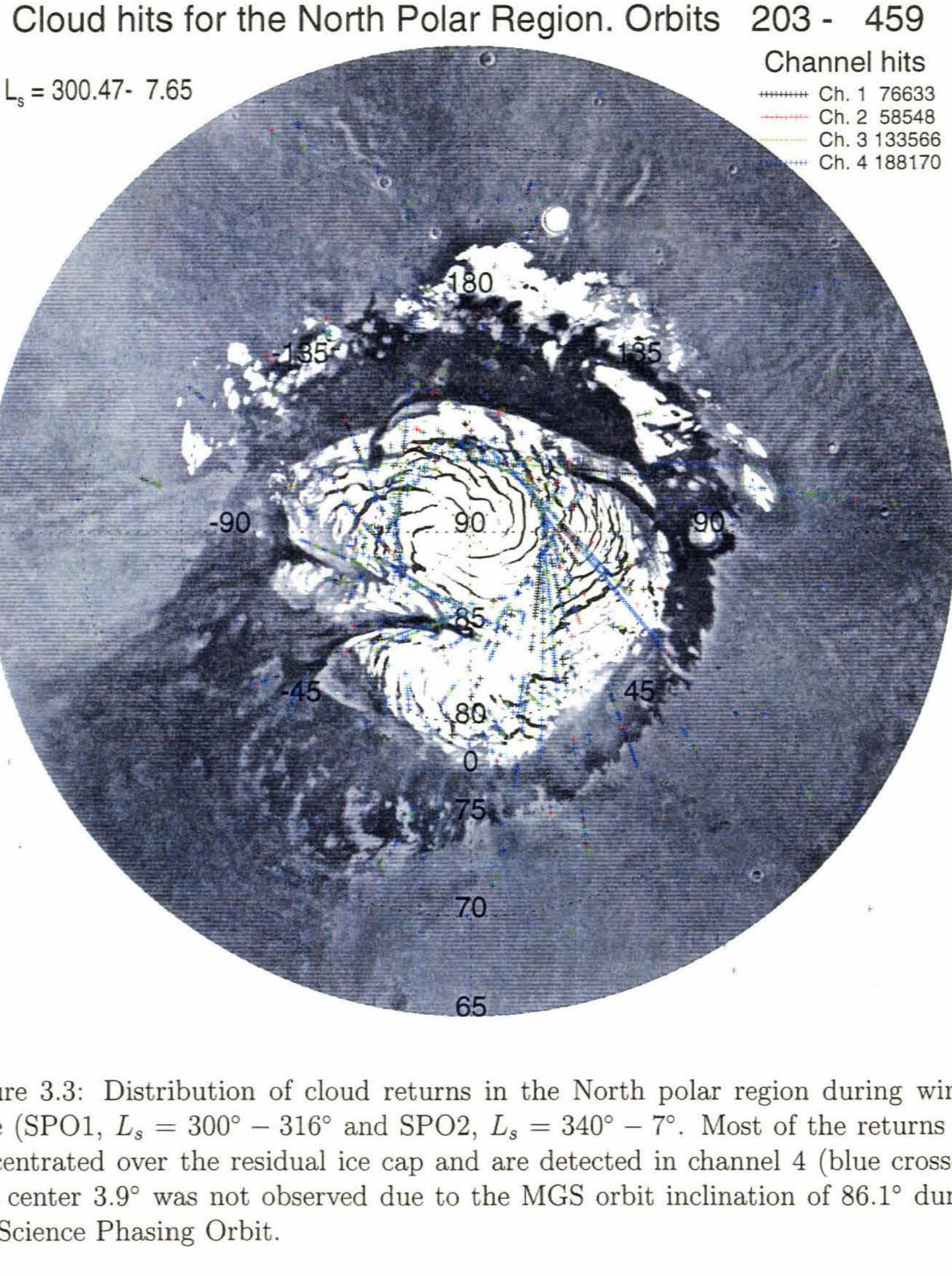

Figure 3.3: Distribution of cloud returns in the North polar region during winter time (SPO1, $L_s = 300^\circ - 316^\circ$ and SPO2, $L_s = 340^\circ - 7^\circ$. Most of the returns are concentrated over the residual ice cap and are detected in channel 4 (blue crosses). The center 3.9° was not observed due to the MGS orbit inclination of 86.1° during the Science Phasing Orbit.

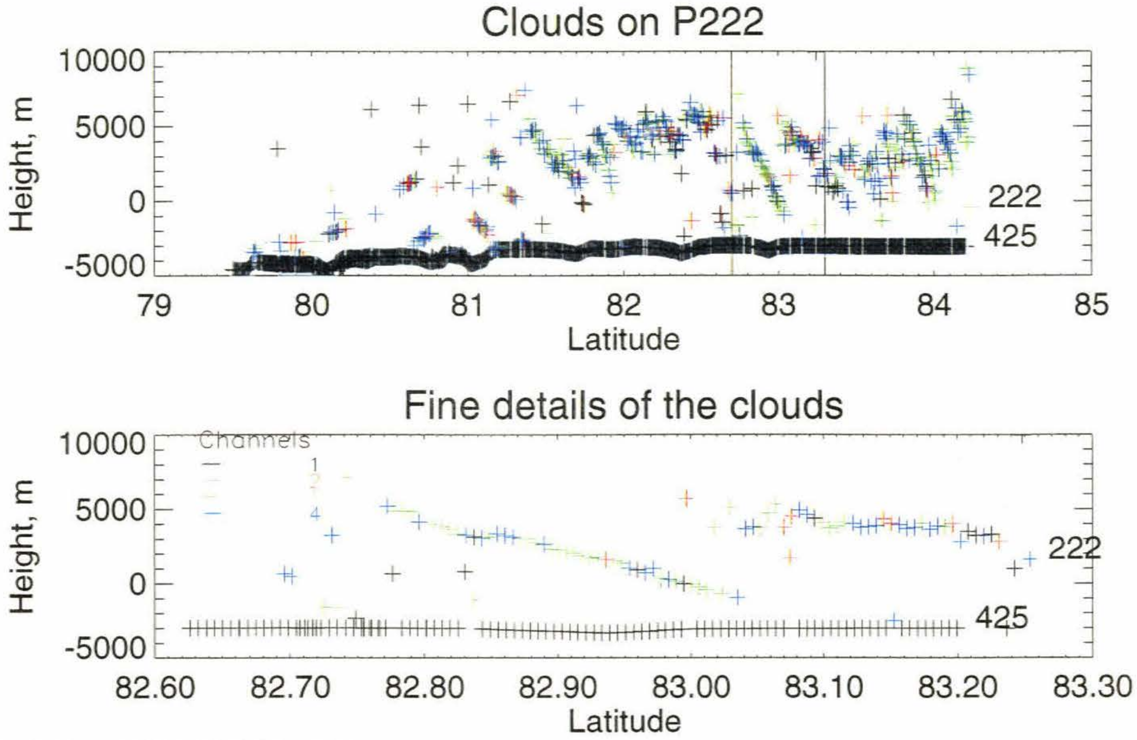

/home/anton/planets/MOLA/PRO 23Jun99 15:21:44

Figure 3.4: Fine details of a cloud observed during pass 222. Upper panel shows a general view at high vertical exaggregation. Black ground curve is taken from Path 425, which was not obscured by clouds and lies adjacent to the track 226. Lower panel shows detail of cloud. Slopes of individual cloud structures vary from almost flat to about 20 − 25°. Almost all signal returns from the clouds are registered in channel 3 or 4. Black crosses are returns in channel 1 (usually from the ground); blue crosses are returns in channel 4 (cloud returns).

3.4.2 South Polar Region

Mars Global Surveyor started mapping operations in March 1999. This time corresponds to the middle of Martian southern winter ($L_s = 103°$). The orbit has became circular with a period of 2 hours and periapsis altitude increased to about 380 km. Such an orbit provided much more extensive temporal coverage of the South Pole, compared to the North Pole coverage, where MOLA passed over only once in 12 hours. Even though range from MGS to Mars increased, we still detected returns from the clouds. They were as extensive as during the SPO orbits. Example of cloud coverage during the mapping orbit is shown in Fig. 3.5.

We can separate cloud structures or patterns observed over the South pole into two types. Fig. 3.6 illustrates both types. Type 1 cloud pattern is very similar to the North polar clouds. They look like a flat line of returns, forming about $0° - 20°$ slopes. Returns from this type of clouds are usually detected by channels 3 and 4. Channels 1 and 2 trigger very rarely. These returns are located predominantly over the polar layered deposits. Type 2 clouds are confined in the 70°S-80°S latitude band and appear episodically over almost all of the longitude range. They do not exhibit as distinct cloud tops like the clouds over the residual caps, but spread out from the ground up to about 7km elevations over the ground. The most surprising difference from type 1 clouds is that most returns were observed in channel 1, which has a very narrow filter width of 3m. This channel is supposed to trigger to ground returns only! Cloud height latitudinal distribution is shown in Fig. 3.2. We will discuss the implications for nature of these clouds in the section 3.6.2. Type 2 clouds were only found over the South polar layered deposits. However, such clouds could have possibly formed in the North polar region before the period of MOLA observations. Only a very small number of clouds with sharp tops was observed after $L_s = 125°$, which corresponds to $L_s = 305°$ during the northern winter, when SPO observations started. Both types of the observed clouds also appear to be correlated with the low emission zones reported by the IRTM instrument on board the Viking Orbiter spacecraft (Kieffer et al. (1977)) and were later interpreted as a snowfall by Forget

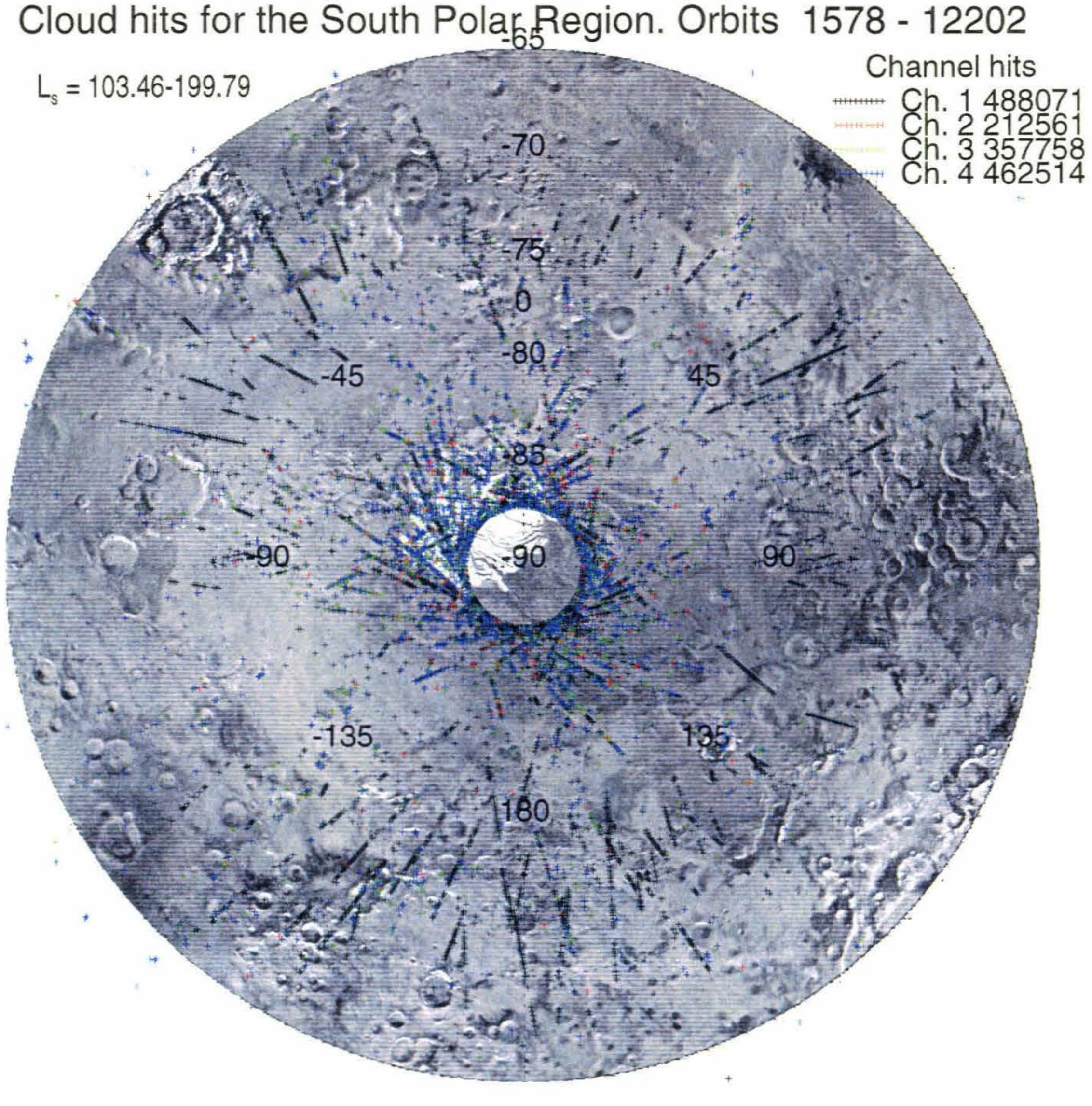

Figure 3.5: Distribution of cloud returns over the South polar region for $L_s = 103.47^\circ - 199.79^\circ$ (southern winter). The area shown is south of 65°S. This dataset covers 8 consecutive days during the mapping observations. Black crosses are returns in channel 1; blue crosses are returns in channel 4. Cloud formations in the 68°S - 75°S latitude band were not observed at the North Pole (c.f. Fig. 3.3). Most of the returns in these clouds are in channel 1. See Fig. 3.6 for details of vertical structure.

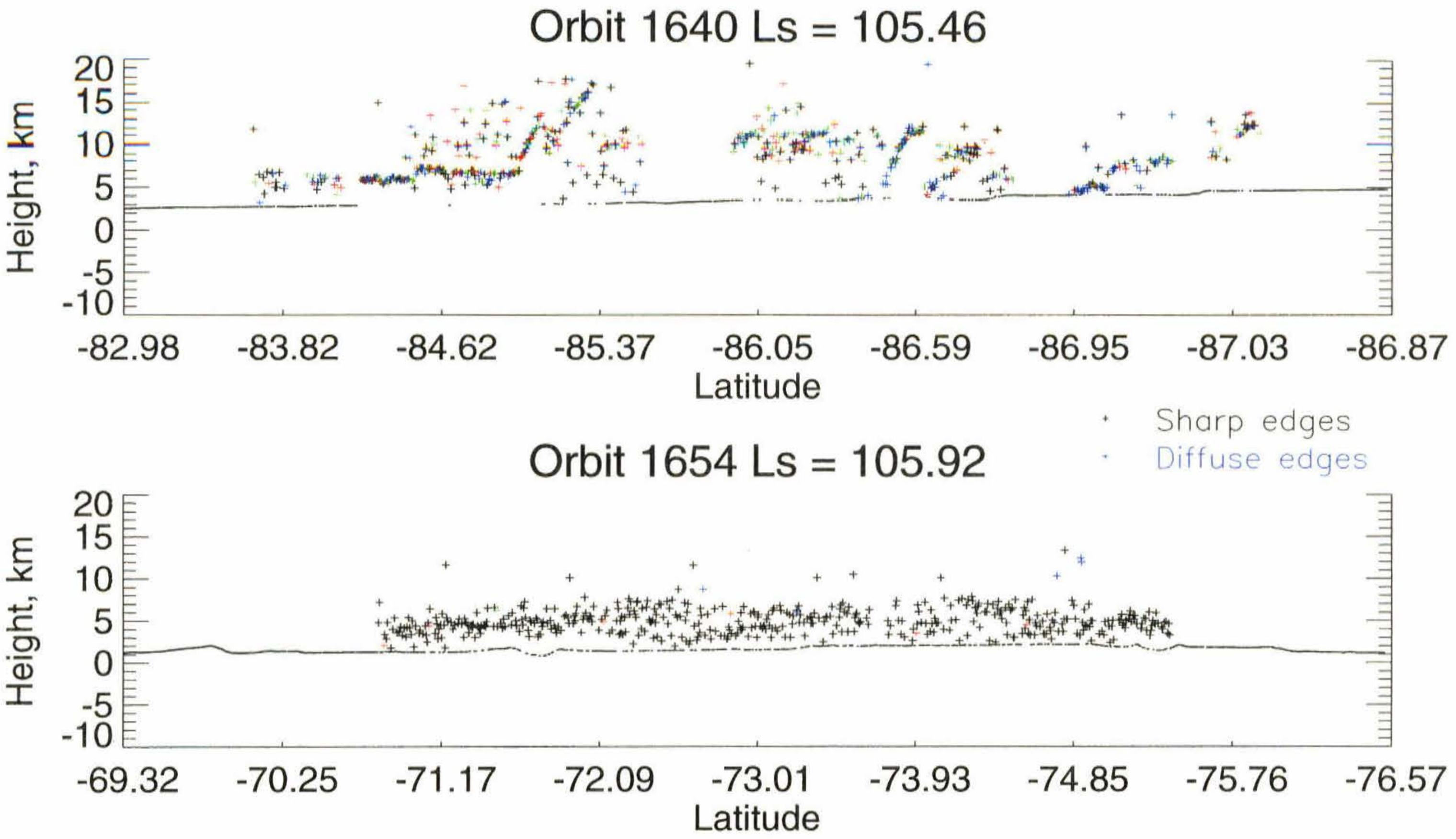

Figure 3.6: a. (upper panel) Example of a cloud structure over the permanent ice cap - type 1 cloud. Most of the returns correspond to a diffuse (or gaussian) cloud top. b. (lower panel) Example of a cloud structure near southern permanent ice cap - type 2 cloud. Most of the returns correspond to a very sharp (delta function) cloud top.

et al. (1998). Low brightness temperatures in the polar regions were also reported by the TES instrument in Titus et al. (1999). We will compare TES and MOLA data in section 3.7.

3.5 Cloud opacities

We were able to use MOLA reflectivity data to estimate optical density of the North polar clouds. On several occasions. MOLA received unsaturated return from the ground through the cloud cover over the ice cap. Assuming a reasonable value for polar ice cap albedo (0.5) we can estimate an upper bound for a cloud opacity to be 1.7. We believe that optical density of the reflecting clouds is possibly smaller. Summary of these observations is shown in Table 3.2. Due to high sensitivity of the MOLA detector. return energy measurements are mostly saturated. even in the high cloud density regions. We were not able to obtain unsaturated reflectivity measurements in the South polar region.

Region	Assumed albedo	Estimated opacity
70-80N	0.4	0.6
84N	0.55	1.7

Table 3.2: Atmospheric opacity during the north polar night

3.6 Model

Cloud echoes are detected when the backscattered energy integrated over a receiver range window exceeds a set threshold. This primarily occurs in the clouds. filling the MOLA beam with sharp tops on scales of a few meters to the order of about 100 meters. The maximum pulse width MOLA is able to measure is about 160m (two-way). In other words. MOLA can only sense top 80m in the cloud. Since the range gate is closed after the first detection. we do not have any information about the underlying surface or atmosphere under the layer of detection. In this section we present a method to computing volume backscattering coefficient based on received power and pulse width which are measured by MOLA.

3.6.1 Cloud reflections

Consider a single particle with scattering cross section σ (isotropic scatterer). The scattering geometry appropriate for MOLA is illustrated in Fig. 3.7. Power reflected from a particle can be written as

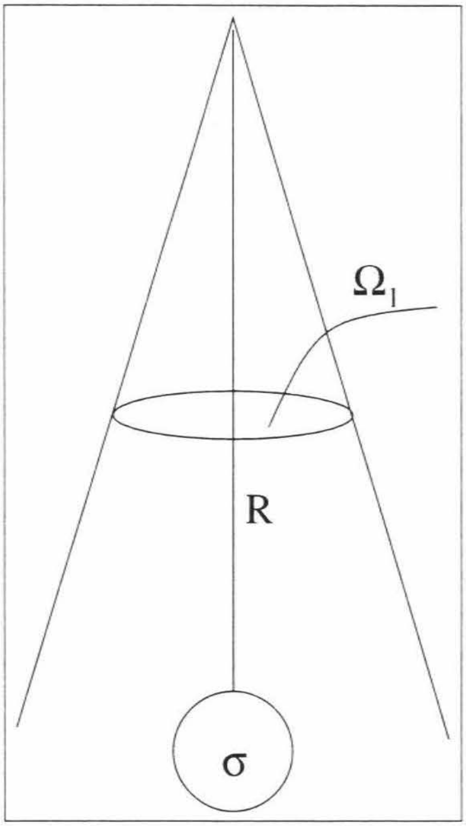

Figure 3.7: Solid angle illustration. Here Ω_l - is the solid angle of the laser beam, R is the range from the laser to a particle and σ is the scattering cross-section of a particle.

$$P_r = \frac{P_t}{\Omega_l}\frac{\sigma}{R^2}\frac{1}{4\pi}\frac{A_r}{R^2} \tag{3.1}$$

where Ω_l - is the solid angle of the laser beam. R is the range from the laser to the particle, σ is scattering cross section of the particle, P_t - transmitted power and A_r - area of the receiver. For N particles per unit volume, the total cross section can be written as

$$\Sigma = Vol * N * \sigma \tag{3.2}$$

where Σ - total cross section, Vol - the considered volume which is calculated using

$$Vol = R^2 \Omega_l \frac{1}{2} c T_f \tag{3.3}$$

where c - speed of light and T_f - is the receiver filter width during the open window time. Then we can calculate total return from a cloud:

$$P_{r_c} = \frac{P_t}{8\pi} \frac{A_r}{R^2} c T_f N \overline{\sigma} \tag{3.4}$$

where $\overline{\sigma}$ is the average cross section of particles constituting the cloud. This cross section can be calculated using the formulation for a particle size distribution (Hansen and Travis (1974))

$$\sigma_{sca} = \frac{\int_{r_1}^{r_2} \pi r^2 Q_{sca}(x, n) N(r) dr}{\int_{r_1}^{r_2} N(r) dr} \tag{3.5}$$

where Q_{sca} - scattering efficiency, which can be calculated assuming Mie scattering, $x = \frac{2\pi r}{\lambda}$ - particle size parameter, n - refraction coefficient for CO_2 ice (for example) and N(r) - particle size distribution. Information obtained by MOLA does not allow us to distinguish composition of the clouds, whether they are made of water or CO_2 ice. However, it has been suggested (e.g., Gierasch and Goody (1968), Paige (1985)) that CO_2 clouds may exist at this period. Value for n is taken to be $n_r = 1.404$ and $n_i = 2.31 * 10^{-6}$ from Warren (1986).

Using the above formulation, we can make some assumptions on the returned pulse shape. As expected, a return from a flat filled surface is very close to a gaussian. A return from a cloud has a much lower amplitude and has a much wider pulse width, due to a very diffuse reflector. Weak, but detectable, reflections can be received from all depth layers of the cloud. This is very similar to the expected signal from type 1 clouds. MOLA has a sister instrument, Shuttle Laser Altimeter (SLA) (Garvin et al. (1998)). It is very similar to MOLA in design. SLA-02 is a hybrid instrument combining ranging electronics, modified from the Mars Observer Laser Altimeter (MOLA-1) design, with a high-speed digitizer used to record the Earth backscatter return amplitude as a function of time, which makes it possible to record the return signal shape and avoid saturation issues. Shape of the return from Earth cirrus clouds can be used as analog to Martian cloud returns. Fig. 3.8 illustrates waveforms obtained from the Earth ocean surface and a cloud over the ocean. Ocean surface can be considered as ideal reflector due to its extremely flat surface.

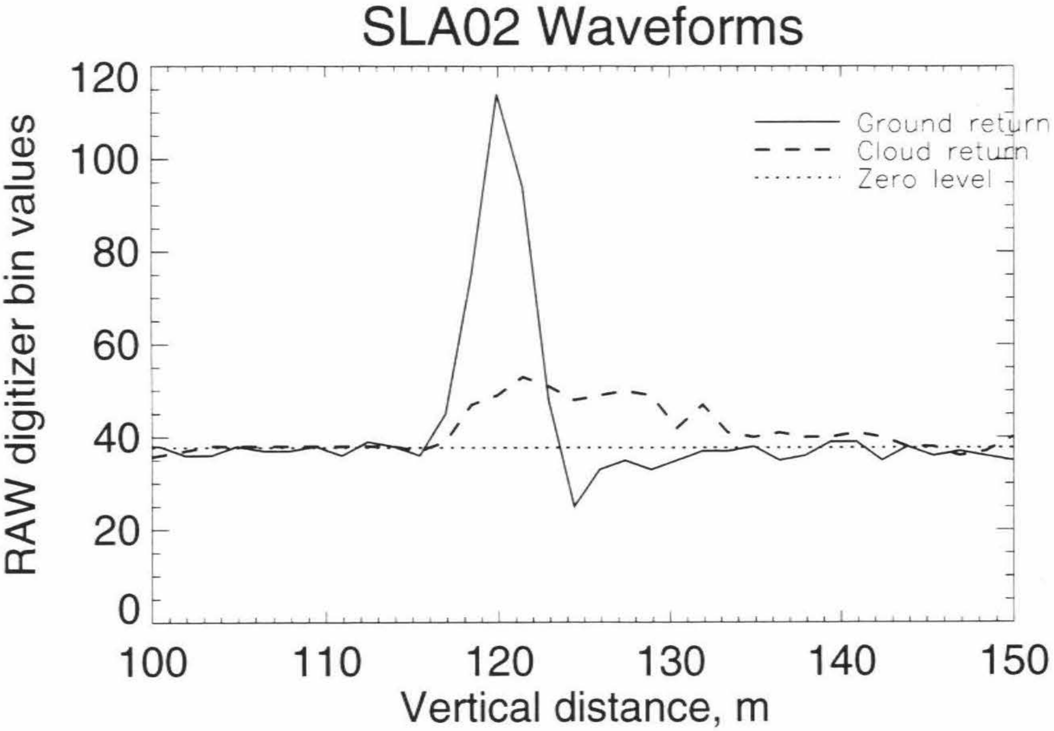

/home/anton/planets/MOLA/PRO 25Jun99 18:53:17

Figure 3.8: Raw SLA-02 waveforms. Returned signal shape from an ocean surface (solid line); returned signal shape from a cloud over an ocean (dashed line).

We have created an instrument model to investigate cloud structures that may produce signatures observed by MOLA. Our model has 4 gaussian filters of different width, which correspond to the MOLA filters. We input to the model a number density profile and compare the output with MOLA reflectivity and pulse width data. We chose two structures as input: narrow gaussian (5m FWHM, to match with channel 1 or 2 returns) and wide gaussian (80m FWHM, to match with channel 4 returns). Modeled MOLA output is shown in Fig.3.9. The goal of the modeling was to check which channel would trigger in response to various vertical cloud structures.

We considered two input clouds structures: a very narrow (in MOLA filters sense) about 5m and a wide cloud - about 100m. As we expected channel 2 triggers first to the narrow gaussian and channel 4 triggers first to the second input form, wide gaussian. The input cloud structure should be even narrower (1m thick) than in the considered case for channel 1 to trigger. Clearly, the output of the model will also have a gaussian form. In reality the cloud shape possibly is not gaussian and these simple assumptions have to be modified. MOLA does not digitize the shape of the returned signal. The Variable Gain Amplifier (VGA) and Wavefront Digizitzer were only implemented on the SLA-02 instrument. The return from an Earth cloud is not a gaussian in most cases. Analogy with Earth clouds from SLA-02 experiment (e.g., Fig. 3.8) and other experiments suggests that cloud returns have a sharp leading edge and then exponentially fall off to 0. MOLA has a very short time between threshold crossings. Translated into vertical distance it corresponds to only top 80m of the reflecting cloud. Detector is "on" for the leading edge of the cloud return and the energy fall-off is small. From the above analogies we can prudently approximate MOLA return signal waveform as a box. We can now calculate the backscattering coefficient β_π from MOLA received energy and returned pulse width. The following formulation was suggested by X. Sun (personal communication, 1999) to calculate the reflective energy received from the clouds.

$$\beta_\pi = \frac{EC}{W_y(ns)} * 3.3333 * \frac{R^2}{E_{laser}} * 1.416 * 10^{-13} \tag{3.6}$$

where EC - pulse energy raw counts (0-255), W_y - Measured Pulse Width at threshold,

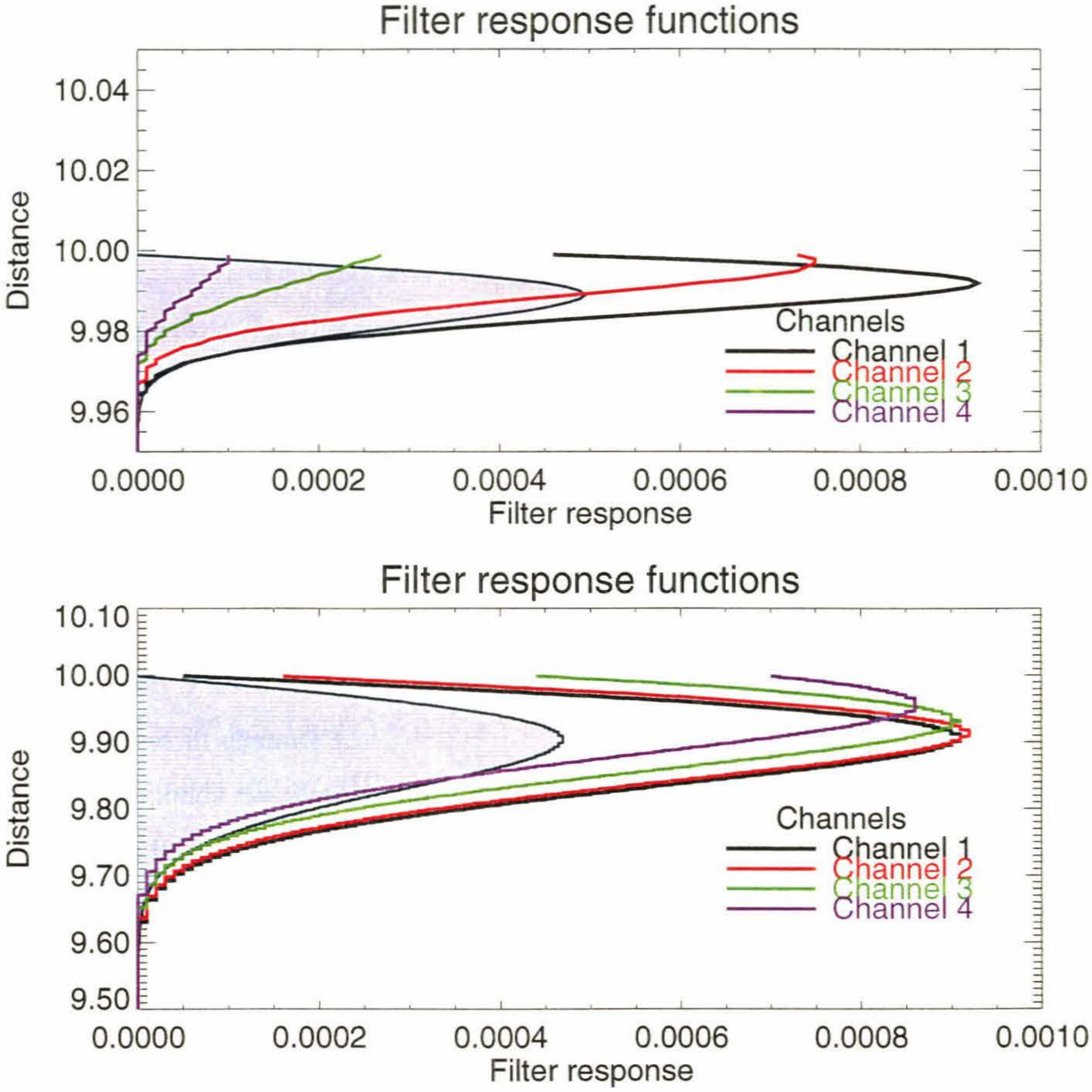

Figure 3.9: Output of the MOLA instrument model for two different cloud structures. Displays modeled response for a 5m (upper panel) and 500m (lower panel) thick clouds. The vertical scale of the figures is significantly different to show the details. The assumed cloud number density profile is shown in grey. For the 5m thick cloud the response of channel 2 will the trigger first. For the wide 500m cloud channel 4 will trigger first. We think that "narrow" 5m thick clouds are the best model for type 2 clouds (south polar clouds off the layered deposits) and "wide" clouds are the best model for the type 1 clouds (polar clouds over the caps). However, in both cases clouds could continue down to the surface, but information from MOLA is restricted to the upper 80m of the cloud layer.

ns (see section 3.3). R is the MOLA range (cm) and E_{laser} is the emitted laser energy. Constant coefficients reflect scaling from engineering to metric units. This formulation is applicable only where energy counter and pulse width counter are out of saturation. Eq. (3.6) is similar to Eq. (3.4), expressed in values reported by the MOLA telemetry. Here EC corresponds to received power P_r, W_y corresponds to returned pulse width cT_f and E_{laser} is transmitted laser energy P_t. Values of backscattering coefficient and comparison with values for Earth clouds will be discussed in the next section.

3.6.2 Backscattering coefficient

As was mentioned above, we can distinguish two cloud types. Both cloud types are illustrated in Fig. 3.6. Type 1 clouds (Fig. 3.6a) are mostly detected by MOLA's channel 4, which is the widest of all channels and measures pulse widths up to 540ns (80m one-way). Such response is caused from a relatively diffuse cloud top, compared to the returns in channel 1.

Type 2 clouds are distributed uniformly within 5-7 km altitude. They appear as broken clouds, not obscuring the surface completely as do type 1 clouds. As shown in Fig. 3.6b, most of the returns are in channel 1. Response from a cloud in this channel indicates a very sharp top, especially compared to clouds of type 1. The width of a pulse necessary to trigger detection for type 2 clouds is only 3m, where as type 1 is 80 meters. This indicates high values of particle number density gradients right at the top of the clouds. The best interpretation for type 2 clouds are patches of forming CO_2 clouds on a scale of about 200 m each, 1-5 km apart.

Simple statistics on reflectivity and pulse width for both types of clouds are presented in Table 3.3. Type 1 clouds have a much wider pulse than type 2 cloud returns. Here reflectivity is a ratio of the received energy to the emitted energy. More discussion of this parameter can be found in Chapter 4.

Computed volume backscattering coefficients (β_π) in Tables 3.4 and 3.5 allow easy comparison of MOLA derived values and expected values for standard particle size distributions from Deirmendjian (1969) for water clouds on Earth. We think that

Cloud type	Channel 1	Channel 4	Reflectivity	Pulse width, ns
Type 1 (north), orbit 226	15	48	0.02 ± 0.01	400 ± 200
Type 1 (south), orbit 10825	20	45	0.03 ± 0.01	400 ± 200
Type 2, orbit 10013	94	2	0.005 ± 0.004	8 ± 7

Table 3.3: Reflective properties of the clouds. Channel 1 and Channel 4 columns display number of hits in the respective channel.

Cloud type	Pass number	$\beta_\pi, 1/(m^3)$
Type 1 (north)	226	1.7e-4
Type 1 (south)	10819	2.2e-4
Type 2 (south)	10012	8.0e-4

Table 3.4: Backscatter coefficient β_π at 1.064 μm for different types of polar night clouds on Mars

Cloud type	N, cm^{-3}	r_m (μm), α, γ	β_π,Water ice $1/(m^3)x10^{-4}$	β_π, CO_2 ice $1/(m^3))x10^{-4}$
Cumulus cloud C1	100	4.0, 6.0, 1.0	19.1	12.4
MOP cloud	100	2, 8, 3.0	16.2	9.1
Haze L	100	0.07, 2.0, 0.5	2.6	1.1
Haze M	100	0.05, 1.0, 0.5	5.2	2.1

Table 3.5: Backscattering coefficients at 1.064 μm for various types of Earth cloud distributions. CO_2 ice clouds can not be observed on Earth and are presented for comparison. r_m, α and γ are the parameters for the modified gamma distribution.

most of the clouds observed by MOLA are composed of CO_2 due to extremely low temperatures during the winter season. To compile Table 3.4 we applied Eq. (3.6) to every cloud return data from 3 tracks, which are representative of both cloud types in the north (type 1 only) and the south polar regions. Average values of backscattering coefficients were computed for each of the tracks and are shown in Table 3.4. Backscattering coefficients in Table 3.5 are calculated assuming Mie scattering, for both CO_2 ice and water ice, using corresponding refraction coefficients. Following Deirmendjian (1969) we used a modified gamma distribution with parameters r_m (particle radius, μm), α and γ. Note that on Earth Hazes L and M are formed by liquid droplets. It is doubtful that suspended liquid water particles can exist under Martian conditions. Hazes may be formed by water ice particles. Type 2 clouds typically exhibit stronger backscattering than type 1 clouds. Type 2 clouds may be closer to cumulus or MOP (mother-of-pearl) clouds [1]. Their morphology (height distributions) suggests broken up clouds that spread over 7km in elevation. Type 1 clouds, commonly observed over the layered deposits, appear to be haze-like and flat.

Clearly, there is no reason to expect Earth water cloud particle size distribution to be the same on Mars. Clouds are forming in completely different temperature-pressure regime. It is also very important that CO_2 is the main constituent of the atmosphere, while on Earth water is a relatively minor component. A microphysical model is required to model possible properties for the MOLA observed clouds, given conditions of Mars polar night.

Similarly unknown is the particle number density N for Eq. (3.4). It also has to be modeled or assumed. It appears impossible to deconvolve one number density and cross section from the information obtained by MOLA only. A microphysical model for CO_2 ice formation along with pressure-temperature information from observations or GCMs should be used to model these parameters. MOLA cloud elevations can be used as input to such model and the product of N and $\overline{\sigma}$ is a very good constraint. Moreover, scattering properties of CO_2 ice crystals are poorly known at this time.

---

[1] **"mother-of-pearl"** or nacreous clouds are thin wave clouds that form at great heights (up to 10 kilometers) and occasionally are observed in the stratosphere (at 20 to 30 kilometers) over the mountains of Norway, Scotland, Iceland, and Alaska.

3.7 Comparison with the TES polar night data

Performing simultaneous measurements of Mars' phenomena is one of the major goals of the Mars Global Surveyor mission. The Thermal Emission Spectrometer (TES) and the MOLA instruments were able to carry out observations during the north and south polar nights. Here we would like to discuss brightness temperature measurements made by the TES instrument and compare them to the data obtained by the MOLA instrument.

The Thermal Emission Spectrometer is a thermal infrared interferometer/spectrometer with additional broadband visible and thermal channels (Christensen et al. (1992)). Six detectors in a three-by-two array simultaneously take spectra covering the spectral range from 200-1600 cm^{-1} (6-50μm), with a selectable sampling of either 5 or 10 cm^{-1}. A pointing mirror allows TES to view from nadir to above the forward and aft limbs, where the atmosphere is observed without direct contribution from the surface. Each pixel subtends 8.3 mrad of view. For the North polar region during the Science Phasing Orbit, spatial resolution was about 10km. This value is higher for the Mapping period of observations since the periapsis of the Science Phasing Orbit was lower ($\sim 200km$) than for the Mapping Orbit ($\sim 380km$). For comparison, MOLA shot-to-shot distance is about 300m and the footprint itself is about 100m.

Quality polar night observations were only possible at longer wavelengths ($>$ 15μm) due to low signal-to-noise ratio. We will concentrate our comparison on brightness temperatures measured at two wavelengths: 18 μm and 25 μm . We will refer to them from here on as to T18 and T25 correspondingly. T18 is the most sensitive to the surface temperature, and it is far enough from the T15 CO_2 absorption band. Differences between T18 and T25 is an indicator of a grain sizes on the surface. The data for these two wavelength bands were provided to us by T. Titus and H. Kieffer of the TES team.

It is well known that grain size has an effect on the emissitivity of the surface material. The larger the grain, the less transparent it is to the infrared radiation. For example, if the surface is covered by freshly formed, unpacked snow, the apparent emissivity will be much lower than that of pure ice or well packed snow. There are two possible explanations for the observed apparent low brightness temperatures. Either grain size is significantly larger or the atmosphere is not transparent (clouds) and the instrument senses atmospheric temperatures at the heights of the clouds. These hypotheses were first suggested by Kieffer et al. (1977).

Figs. 3.10 and 3.11 illustrate comparison of MOLA cloud echoes with TES' T18 and T25 temperatures taken on orbits 222 and 226 ($L_s \sim 300°$, north polar night). No sun insolation is received during this time near the pole. T25 temperatures exhibit some correlation with the cloud height data, but it is not full correlation. Consider track 222. The coldest temperature at 86°N (T = 120K) corresponds to the most extensive cloud formation in the MOLA data. However, the cold spot at 85°N (T = 130K) does not correspond to any of the observed clouds in the MOLA data. Same pattern can be seen in track 226. The TES brightness temperatures in the region over the pole, north of $\approx$ 83°N, reach values of about 125K. At the same track, cold spot at 82°N coincides with very low cloud density. Data in T18 are more interesting. The minimum brightness temperature on track 222 (T18 = 138K) is located right over the most extensive and highest cloud formation in the MOLA data. In track 226, minimum cloud temperatures also correspond to dense clouds. T18 brightness temperatures are lower than the expected blackbody temperature of polar ice in winter.

Comparison of the TES and the MOLA data in tracks 222 and 226 suggests that T25 temperatures are possibly due to the grain size effects of snow at the ground and the atmosphere is transparent at this wavelength. Snow grains might have just fallen from the atmosphere or formed on the ground. T18 channel also observes some of the grain size effect, but the extremely low temperatures are due to atmospheric effects. Minimum brightness temperatures in both T18 and T25 occur in the same places in both tracks and are possibly observed in the atmosphere when the ground is completely obscured by the condensing ice particles. MOLA and TES simultaneous observations suggest that large grains of CO_2 form in the atmosphere and fall out, or in other words, CO_2 snowfall. It has been suggested before by Forget et al. (1998) as

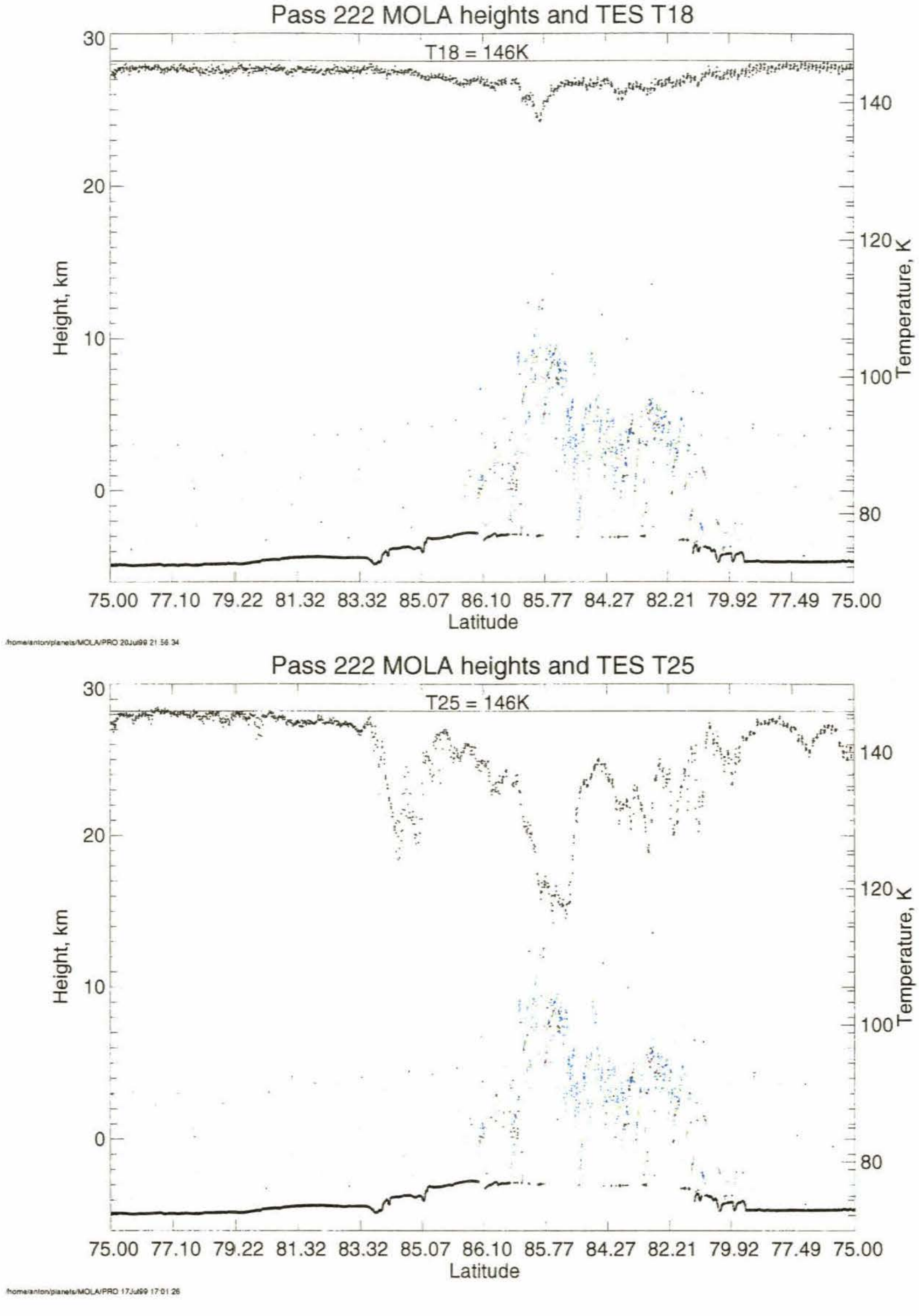

Figure 3.10: Comparison of the TES brightness temperature data with the MOLA cloud observations. Data shown are for track 222, north of 75°N. MOLA cloud observations are shown by colored dots in the bottom part of the graphs. Brightness temperatures are shown in the upper part of both graphs. Temperature minimum at 86°N correlates well with the extensive cloud formation.

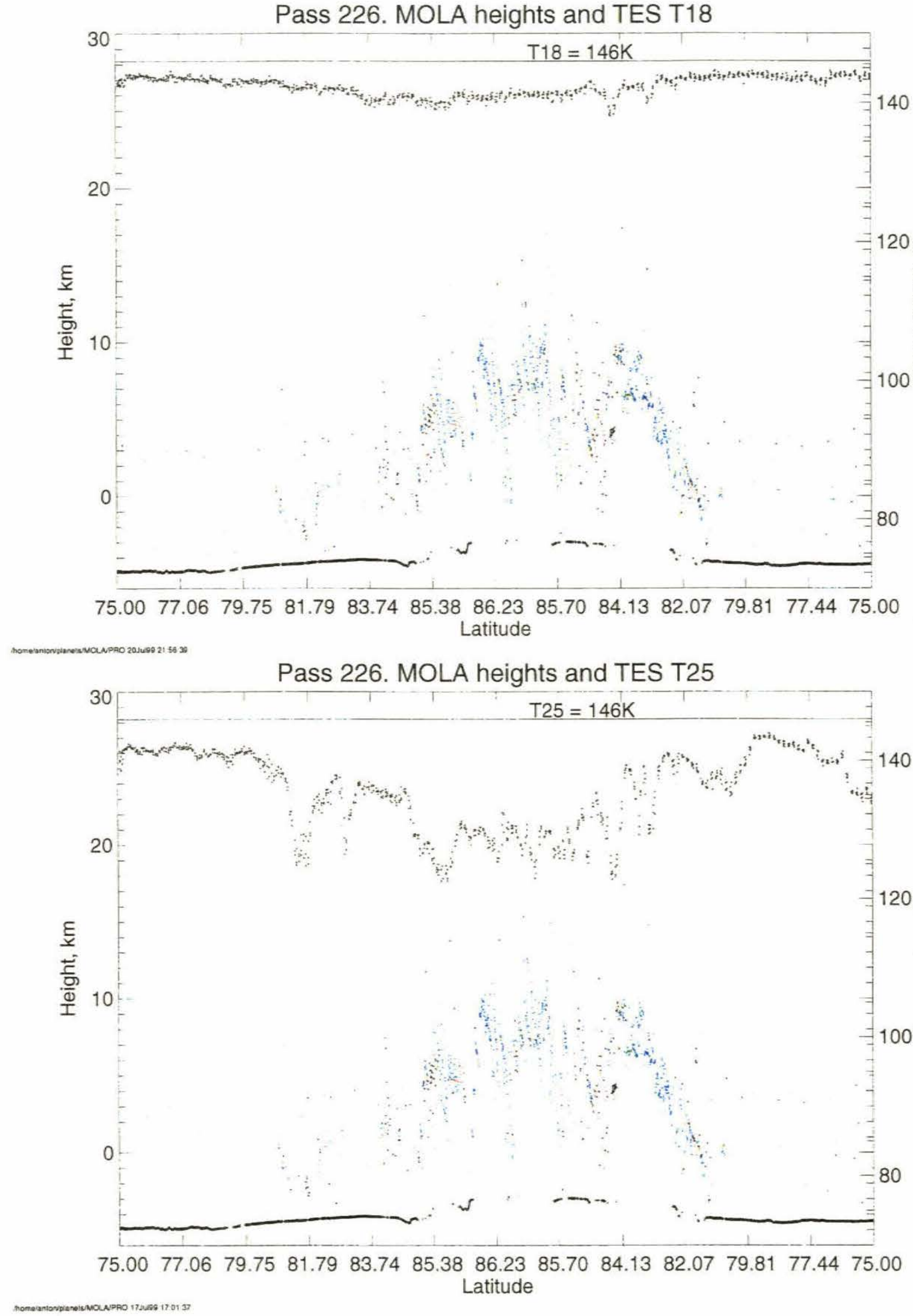

Figure 3.11: Same as Fig. 3.10 for track 226.

an explanation for the low brightness temperatures the Viking IRTM data. We should note, however, that observed low brightness temperatures still can be interpreted as a grain size effect. However, the correlation of MOLA cloud observations and TES brightness temperature measurements significantly weakens that hypothesis.

3.8 Discussion

MOLA observations of the cloud structures are the first direct measurements of this kind. Clouds were observed during north and south winter, when the polar regions are shrouded in absolute darkness. Although MOLA can not distinguish the composition of the clouds, they most likely are composited of CO_2 ice. No significant cloud reflections were observed during the day time. Occasionally, MOLA has registered cloud reflections during the night time in locations out of the polar regions on the planet. These could be returns from the dust particles, covered by a thin layer of water ice. A thin layer of ice is a very effective backscatter as opposed to an ordinary dust grain.

Existence of two types of clouds is very intriguing. Pettengill and Ford (1998) suggested gravity waves, excited by the ice cap topography, to explain for the type 1 clouds, which were observed in both North and South polar regions over the NPIC and SPLD. Type 2 clouds have not been yet explained. They occur very close to the terminator on the night side. Possibly they form where temperatures fall below the condensation level during the night time. We do not understand yet why they form in three distinct areas of the South polar region (Fig. 3.5). We need to investigate contributions of radiative and adiabatic cooling to the process of the cloud formation. Most of the cloud observations occurred after winter solstice in both hemispheres. Science Phasing Orbits cover the period from $L_s = 300°$ to $L_s = 7°$ and Mapping observations started from $L_s = 103°$ (c.f. Table 2.1). Predictably, a lot of clouds were forming before the winter solstice. Indeed, right after $L_s = 190°$ clouds reappeared in the North polar region (Fig. 3.1). It will be a very interesting period of observations. The MGS Radio Science Experiment (e.g., Hinson et al. (1999)) have performed numerous occulations, which yielded high-resolution temperature-pressure profiles. We hope to use these data in conjunction with the TES brightness temperature measurements to fully quantify radiative processes in the polar regions.

Combined observations of the low brightness temperature areas and MOLA cloud structures suggest that MGS instruments observe CO_2 snowfall. Simultaneous observations of clouds and low brightness temperatures are possibly due to an ongoing snowfall. Low brightness temperature zones without any cloud detections are possibly due (1) a recent snowfall, (2) condensation of CO_2 on the ground, (3) an ongoing snowfall, but undetected by MOLA. A more meticulous analysis of the TES and MOLA data will help to distinguish between these possibilities. This work has analyzed only two passes out of about 200 for the Science Phasing Orbits. An enormous amount of data for the South polar night now exists and has about 1500 passes near the pole with an interval of 2 hours. Observations of CO_2 fall out rates and their spatial extent have important implications for the global CO_2 cycle. Most Mars GCM do not take into account process of CO_2 condensation and cloud formation, and hence lower emissivity values for the polar regions. However, some studies found (e.g., Forget (1998)) it was necessary to use artificially low values for the modeled ice cap emissivities to account for a condensation rate of CO_2 in the atmosphere lower than expected.

Backscattering coefficient (β_π) calculations allow first order comparison of Mars CO_2 clouds and Earth water vapor clouds. Clouds that have a similar backscatter coefficient would probably appear similar to a human eye (if illuminated). The results of the calculations are shown in Tables 3.4 and 3.5. β_π for Martian clouds of type 1 is similar to the β_π of hazes on Earth. Type 2 South polar clouds have a similar value of the backscattering coefficient to the MOP clouds. This result appears to be counterintuitive, because the morphology of polar clouds (type 1) is similar to flat strata. South polar clouds appear as a fog, rather than MOP clouds. We would like to point out again that condensation of CO_2 in the Martian atmosphere and condensation of water vapor in the Earth atmosphere are two completely different processes. No direct information on the particle sizes distribution of the Martian clouds can be retrieved from this analysis.

CO_2 ice clouds are important as a part of thermal atmospheric flux (e.g., Pierrehumbert and Erlick (1998)), if the particle size is significantly large. They are effective scatterers in the infrared. If the particle size is small ($< 10\mu m$), no snowfall will occur as the particles will stay suspended in the atmosphere. Ice particles this small will be transparent for the infrared radiation. It is not possible to calculate mean particle size from MOLA backscattering coefficient measurements alone. A microphysical model of CO_2 crystal formation is required to obtain information about particle sizes and number densities. In the light of the MGS cloud observations and latest radiative balance modeling by Forget et al. (1998), it is apparently unlikely that particles are small in size. We think that clouds are formed from crystals more than 10 μm in size. Dust grains and water ice particles can act as nucleation centers.

3.9 Conclusions

MOLA cloud height observations present first direct observational evidence for existence of polar night clouds. No other instrument is able to perform these measurements with such quality and reliability. Extensive coverage during SPO and mapping orbits is an excellent dataset allowing analysis of spatial and temporal variations of the cloud heights. We can identify two types of clouds on the basis of spatial occurrence and reflective properties. Two types of clouds exist possibly due to different mechanisms of their formation. Backscattering coefficient of the cloud tops can be extracted from returned energy and pulse width measurement. We performed comparison with the Earth water vapor clouds based on values of the backscattering coefficient. This comparison suggests that type 1 clouds (polar clouds) are similar to a haze and type 2 clouds (clouds in the 70°S-80°S latitude band) are similar to the mother-of-pearl clouds.

A microphysical model of CO_2 condensation is required to calculate mean particle size and particle number density. Comparison with the TES data suggests that MGS instruments performed observations of the ongoing snowfall or its effects. CO_2

condensation and fall out is an important process in the global cycle of CO_2 in the Martian atmosphere. It can now be quantified and included in Mars GCMs. The MGS Radio Science temperature-pressure profiles will provide us with more insight into radiative properties of the clouds and cloud forming conditions. MOLA and TES observations of the polar regions during the winter nights provide us information which fills an important gap in our knowledge of polar atmospheric processes on Mars.

Chapter 4 Reflectivity observations in the MOLA investigation

The MOLA instrument has provided us a unique dataset of the reflective properties of the Martian surface. Reflectivity is a product of the albedo of the planet and the atmospheric transmissivity. In this chapter we will present the reflectivity dataset, obtained mostly during the mapping orbit. MOLA has obtained unsaturated reflectivity data from about 80% of the planet. We will also analyze possibilities to create maps of the normal albedo of Mars, uncontaminated with the atmosphere. These maps can then be used to calculate opacity. MOLA derived opacity is found to be similar to the observations by Viking Landers. General opacity trends at 1 μm are consistent with the $9 \mu m$ opacity, measured by the MGS Thermal Emission Spectrometer. Large topographic features allow investigation of vertical structure of the atmosphere and calculation of an atmospheric scale height. Scale height values are generally lower (2-6km) than the atmospheric scale height (10km). This suggests that aerosols are concentrated in the first few kilometers from the surface. Seasonal dependencies for the scale height measurements in the Hellas Basin are briefly discussed.

Some parts of the material presented in the following chapter was published among the collection of the MOLA Science Team papers in Ivanov and Muhleman (1998).

4.1 Introduction

Mars Orbiter Laser Altimeter (MOLA) is an instrument on the Mars Global Surveyor spacecraft. A general description of the instrument can be found in Zuber et al. (1992). The laser operates at 1.064 μm , emitting 8-nsec-long pulses. MOLA measures topography, surface reflectivity and returned pulse width. First tracks of data were acquired during the contingency orbits in September-November of 1997. The first scientific results are discussed in Smith et al. (1998). Later, many more data were acquired during the Science Phasing and Mapping Orbits. Table 2.1 summarizes information about periods of data collection.

In this chapter we will concentrate on the discussion of reflectivity measurements. Reflectivity (R) is a ratio of returned laser energy to the emitted laser energy, adjusted for distance and the Lambert reflection law. It is affected by the albedo (A) of the underlying terrain and extinction of the photons from the laser beam by atmospheric aerosols and can be expressed as $R = A * e^{-2\tau}$, where τ is a total atmospheric opacity. MOLA monitors the emitted power and measures the reflected energy from the ground and the returned pulse width. Small deviations from the Lambert law are expected, see below.

Calibration of the instrument was performed in the laboratory, and it is believed to be accurate to about 10% at worst. MOLA detector was constructed to be very sensitive to the incoming signal. When on Mars, it turned out that incoming signal was much stronger than expected. As a result energy measurements are saturated in about 60% of the data. Later in the mission, the laser energy decreased slightly ($\approx$ 10%) and the average atmospheric opacity has increased. Currently, data are available for about 80% of the Martian surface. Data over the brightest areas such as Tharsis region and seasonal ice cap are still saturated. Unsaturated reflectivity data are also obtained when the ground is obscured with non-reflective clouds.

Opacity or albedo can be inferred from the reflectivity measurement, if one of them is known from some external dataset. In section 4.4 I will present an algorithm to calculate the normal albedo of Mars at the MOLA wavelength using the

TES $9\mu m$ opacity measurement performed by Smith et al. (1999b). To calculate atmospheric opacity (section 4.5) we used the albedo dataset compiled by Plescot and Miner (1981) from the IRTM measurements. We will discuss necessary corrections which should be applied to this dataset, before it can be used at the MOLA wavelength. The red filter, radiometrically calibrated Viking Color MDIMs can also be used as first order estimate for albedo (Eliason et al. (1992)). It offers a much better spatial resolution than 1° × 1° IRTM bolometric albedo dataset, but atmospheric effects have a much greater effect.

We will present a method for calculation of the aerosol scale height using the reflectivity data in section 4.7. The method is based on the analysis of the total atmospheric opacity as a function of elevation. We have chosen large topographic features as study areas, where unsaturated reflectivity measurements are available for a large range of elevations. We will discuss tracks across the Valles Marineris, Olympus Mons, Alba Patera and numerous tracks across Hellas Basin.

4.2 Available datasets on albedo and opacity of Mars

4.2.1 Albedo

The surface markings on Mars have been the object of study by the earth-based astronomers for many centuries. The planet has been known to have strong, variable contrast in color and albedo. The annual growth and retreat of the polar ice caps, formation of the polar hoods, yellow clouds, and blue hazes dominate this variability. The surface also shows a regional contrast between bright and dark terrain more than of a factor of two. Improved abilities of the telescopes early in the 20th century led many researchers to draw maps of the albedo markings. The advent of the photographic photometry even allowed resolution of > 500km features. The situation changed considerably with the start of spacecraft exploration of Mars. On the basis of Mariner 9 pictures, a detailed relative albedo map was compiled.

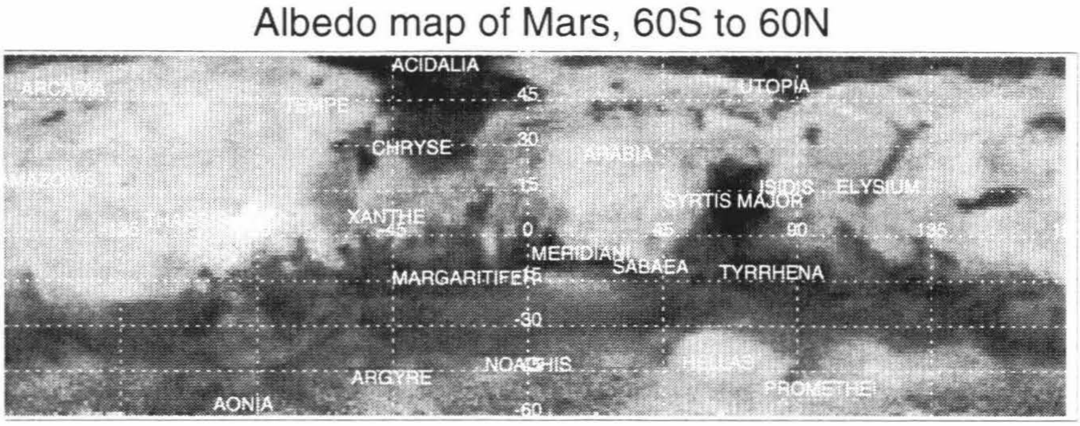

Figure 4.1: Greyscale representation of the albedo dataset compiled by Plescot and Miner (1981) from the Viking IRTM bolometric channel observations. The map provides global coverage from $60°S$ to $60°N$ at 1° by 1° spatial resolution. The albedo data for the polar regions 60 to the pole (not shown) was compiled by Paige et al. (1994). Some classical albedo features are shown at the map.

Infrared Thermal Mapper (IRTM) on board of the Viking Orbiter spacecrafts allowed first compilation of absolutely calibrated bolometric reflectivities of Mars. The IRTM contained solar band detectors which sample simultaneously in a bandwidth from $0.3\mu m$ to $3\mu m$, corresponding to the limits of significant solar illumination. Plescot and Miner (1981) constructed a bolometric albedo map for Mars from the Viking IRTM data. It is shown in Fig. 4.1. The map provides global coverage in longitude for latitudes $-60°$ to $+60°$ at 1° by 1° spatial resolution. The distribution of bolometric surface albedos is bimodal with typical, clear-sky, Lambert albedos of 0.16 and 0.27 for dark and bright regions, respectively. Atmospheric scattering effects were considered very crudely in that work. Using IRTM Emission Phase Function (EPF) sequences, Clancy and Lee (1991) found that in general the albedos derived by Plescot and Miner (1981) were brightened by the atmospheric scattering. Clancy and Lee (1991) have empirically found that bright areas are darker by about 10% and dark features are about 25% darker. This is the best approach for the atmospheric correction of this dataset attempted so far.

Paige et al. (1994) and Paige and Keegan (1994) presented first albedo and thermal inertia maps for the north polar and south polar regions with 0.5° and 1° spatial resolution respectively. Their work completed albedo and thermal mapping of the entire planet. The analysis of the IRTM dataset was aided by the results of a one-dimensional radiative convective model, which was used to calculate diurnal variations in surface and atmospheric temperatures, and brightness temperatures at the top of the atmosphere for a wide range of assumptions concerning aerosol optical properties and aerosol optical depths. One of the indirect results of these calculations showed that the effects of the Martian atmosphere on remote determinations of surface thermal inertia and albedo are more significant than have been indicated in previous studies.

The Mars Global Surveyor Thermal Emission Spectrometer (TES) is the next generation spectrometer, compared to IRTM. It also carries a bolometric channel, similar in characteristics to the IRTM detector. However, it has a much smaller field of view and hence much better resolution. TES has a great potential for deriving a global bolometric albedo dataset at high resolution. The TES albedo dataset was not available at the time of this writing. Atmospheric effects can be considered using independent atmospheric aerosol opacity calculation by Smith et al. (1999b).

Bell et al. (1999) reported on results of observations of Mars with the Hubble Space Telescope at a near-IR wavelength of $1.042\mu m$ between February 1995 and June 1997. The observations were conducted at a wavelength very close to the MOLA wavelength. The images were obtained at relatively high spatial resolution of about 20-30 km/pixel. The normal albedo of typical surface regions was derived from the multiple phase angle observations and was found to be 0.18 for dark regions and 0.36 for bright regions at $1.042\mu m$. The atmospheric correction was not applied as in the case with the IRTM observations, so the resulting albedo might have also been brightened by the atmospheric scattering.

4.2.2 Opacity

The primary source of the opacity in the Martian atmosphere is suspended dust. It is raised by the dust storms, dust devils and precipitates under gravity or together with water, condensing on the dust grains.

The Viking Lander cameras were capable of looking at the Sun as well as at the ground. By looking at the Sun, it was possible to determine the line-of-sight opacity of the atmosphere on a regular basis (Colburn et al. (1989)). These measurements constitute a prime dataset for the study of the opacity during the Viking mission. The Viking Lander opacity was measured using 670nm solar filter. Mars Pathfinder Lander has performed similar observations of the atmospheric opacity at wavelengths of 450, 670, 883, and 989 nm (Smith and Lemmon (1999)). The reported opacities were similar to those determined by the Viking landers. The blue filter variations suggested that submicron water ice particles with opacities as large as 0.14 were responsible for diurnal variations.

Santee and Crisp (1993) and Fenton et al. (1997) have derived the atmospheric opacity from the measurements by Mariner 9 infrared spectrometer. Martin (1986) used data obtained by the IRTM instrument. It has proven to be very useful for tracking dust opacities and dust storms, such as 1977a dust storm. Later work by Martin and Richardson (1993) included the second and more extensive planet-encircling dust storm observed by Viking, known as storm 1977b. Authors improved the method, developed by Martin (1986) and were able to reach greater time resolution and smaller noise. A later reanalysis of the work by Martin (1986), was performed by Toigo and Richardson (1999) to complete the analysis of this dataset and perform comparison with the Viking Lander visible opacity data.

The most recent column-integrated infrared opacity data is available from the MGS Thermal Emission Spectrometer. Smith et al. (1999b) employed infrared spectra to derive dust opacity at $9\mu m$ wavelength and water ice opacity. These data were taken simultaneously with the MOLA reflectivity data. We plan to use the TES opacity data to derive MOLA normal albedo. We will discuss an algorithm in section

4.4.

4.3 MOLA reflectivity

Each reflectivity measurement is actually a measurement of the returned energy from the surface. Reflectivity is calculated from the number of photons registered by the MOLA detector between the threshold crossings. The following equation is used:

$$R = \frac{E_r * \pi * D^2}{E_{tr} * A_r * \eta}, \tag{4.1}$$

where E_r - received optical pulse energy (Joule), D - range to the Martian surface, E_{tr} - emitted laser power, A_r - receiver telescope entrance aperture area (m^2), η - receiver optics transmission. The received optical pulse energy E_r (in Joules) can be calculated by dividing the received pulse area (A, volts×ns) by the detector assembly responsivity (R_{det}, volts/watt).

$$E_r = \frac{A \times *10^{-9}}{R_{det}}. \tag{4.2}$$

More details on the calculation of the received pulse area, corresponding errors and other calibration issues can be found in the MOLA instrument calibration document by Abshire et al. (1999).

The MOLA footprint of the surface is about 100 m in diameter for the mapping configuration ($\approx$ 400km altitude). It was changing during the hiatus and science phasing orbits due to the elliptical nature of the orbit. Shot-to-shot distance is about 300 m. Clearly, the sampling along the track is much denser than across the track, especially for the non-mapping orbits. A sample coverage plots for the Pathfinder landing and the proposed Mars Polar Lander sites are shown in Fig. 4.2. The MPL site is much better sampled, because more orbits cross at the poles.

The reflectivity dataset can be represented as three parts, corresponding to major Mars Global Surveyor observing campaigns: hiatus, Science Phasing Orbits and Mapping Orbits.

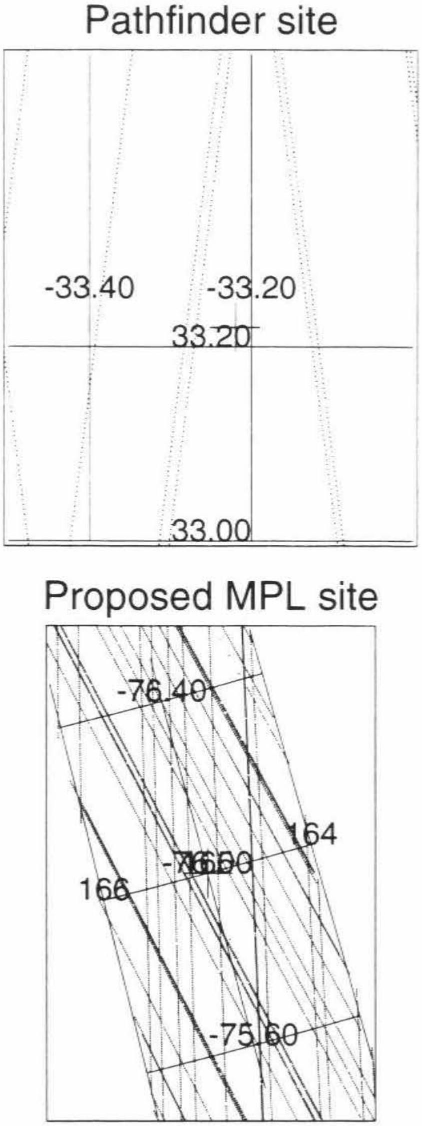
Pathfinder site

Proposed MPL site

Figure 4.2: MOLA ground track coverage for the Mars Pathfinder (upper panel) and the Mars Polar Lander (lower panel). The MPL site is much better sampled, because more orbits cross at the poles. The individual returns are shown as dots. The coverage for the South polar region is so dense that they appear as lines. These examples use data from eight months of Mapping orbits(March - October 1999).

Hiatus dataset is the smallest one of all. Data from only 17 highly elliptical orbits were acquired during this period. The range to the surface of the planet varied from 200 km to 800 km. The coverage is very sparse (see Fig. 4.3). The tracks mostly cover the Northern hemisphere and uniformly spread in the longitude. At large range distances from the planet, the MOLA reflectivity range came out of saturation even over the brightest regions of Mars, such as Tharsis plateau. This allows to estimate what is the maximum albedo of Mars we can expect at these wavelengths. For example, south part of track 24 lies over the flanks of Arsia Mons. Measured reflectivity value is 0.25. Assuming atmospheric opacity of 0.4 and opposition effect of about 30% (see discussion below), we can calculate albedo to be 0.43. This value is consistent with the maximum values obtained from the telescopic observations by Bell et al. (1999). It is the maximum reflectivity observed over the course of the mission.

Science Phasing Orbits cover the period from $L_s = 300° - 7°$. There is a pause in observations due to the solar conjunction from $L_s = 318°$ to $L_s = 336°$. Spatially, Science Phasing Orbits cover most of the Northern hemisphere north of about $20°N$. The best coverage was acquired north of $45°N$. About 50% of the data are saturated, because of short range to the planet's surface. Unsaturated data exists at the ends of the tracks, where the range is large and near the North Polar Ice Cap. Extensive cloud formations and polar hood were observed during that time. The clouds are the subject of the Chapter 3. Fig. 4.4 displays unsaturated reflectivity data collected during the Science Phasing Orbit.

On February 28, 1999, the MGS spacecraft finally started its mapping campaign. The orbit now reached the planned 2-hour sun-fixed orbit. The local time at equator crossings was either 2 am or 2 pm. The saturation problem restricted our initial coverage to the regions with very low albedos such as North Polar dunes, Acidalia Planitia and Syrtus Major. Currently, observations cover the range of L_s from 103° to 240°. The laser output energy decreased slightly since the start of the Mapping campaign, and this allows us to obtain more and more coverage of the planet's surface. Additionally, during the dust storm season, the opacity of the atmosphere increased

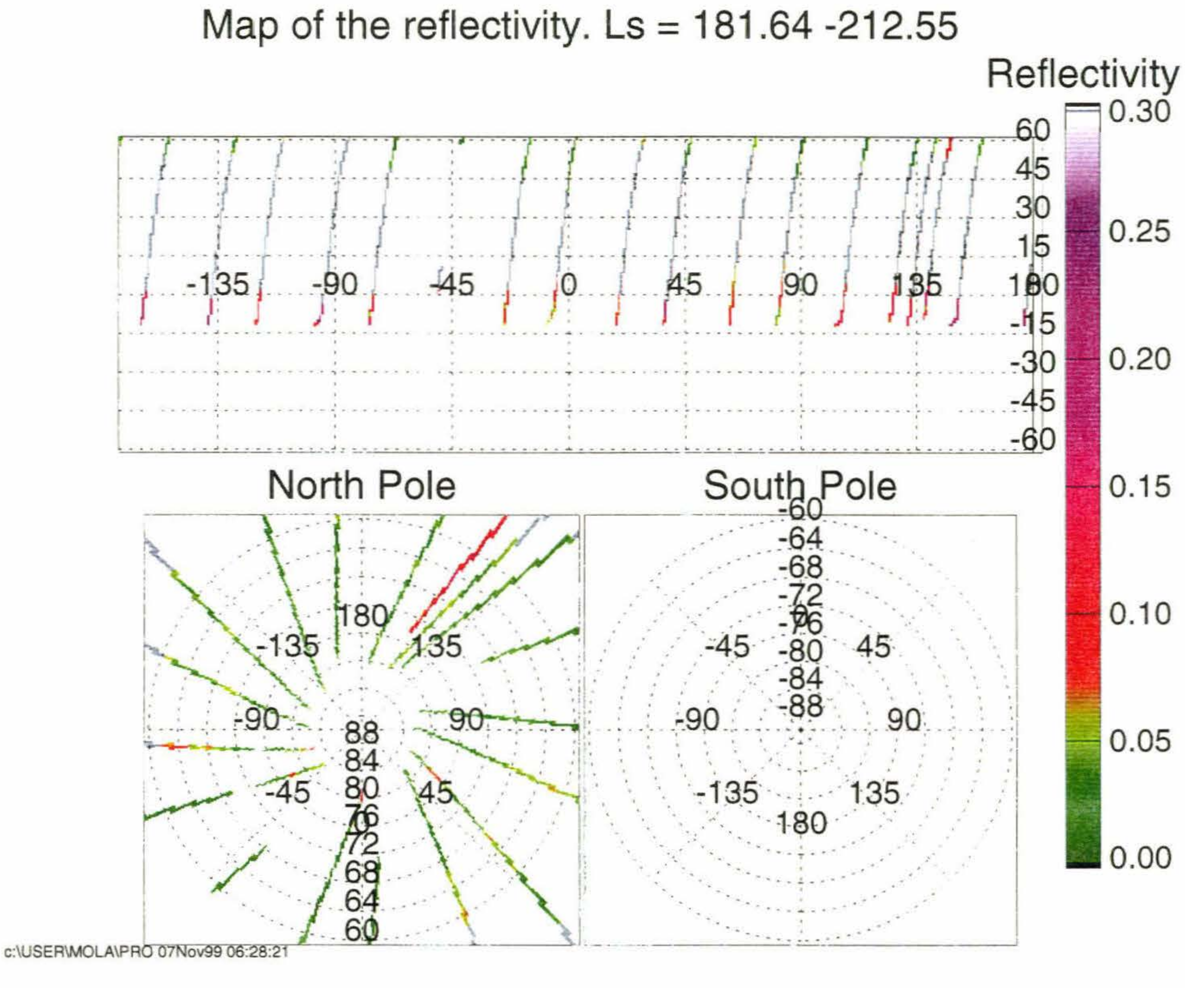

Figure 4.3: The reflectivities acquired during the hiatus orbit. L_s range covered by these orbits is 181° (track 03) and 198° – 210°. The spatial coverage is very sparse. At larger distances reflectivity measurement is out of saturation, allowing us to obtain maximum values, such as near the Tharsis ridge. No data have been collected in the Southern hemisphere. Grey color shows where the reflectivity measurement was saturated.

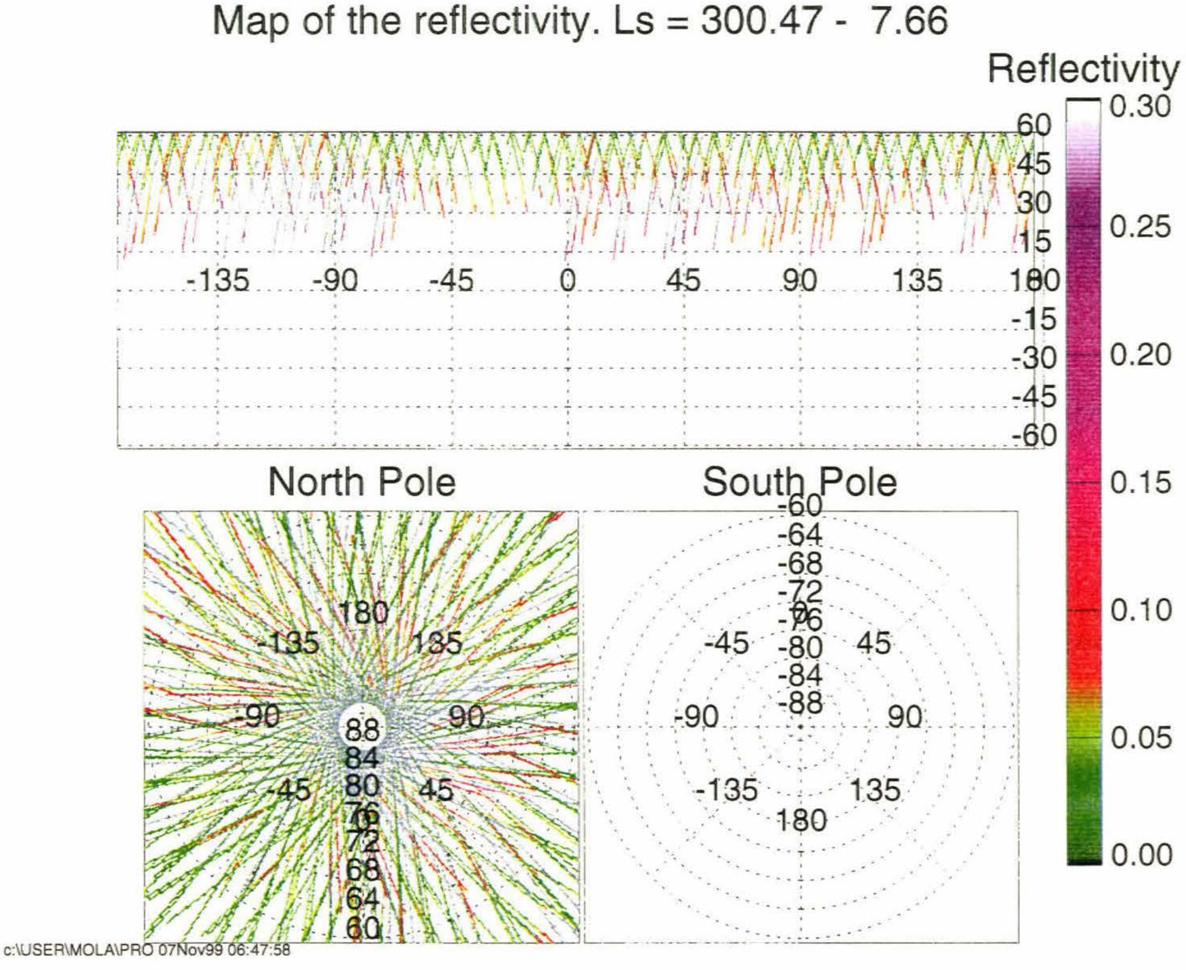

Figure 4.4: The unsaturated reflectivities collected during the Science Phasing Orbit ($L_s = 300° - 328°$ and $L_s = 336° - 7°$). The tracks cover Northern Hemisphere north of $20°N$, with most of the unsaturated reflectivity data lying north of about $45°N$. Data are saturated due to short range distance to Mars. No data has been collected over the Southern hemisphere. Grey color shows where the reflectivity measurement was saturated.

significantly. MOLA obtains unsaturated reflectivity measurements from almost 80% of the planet. Tharsis Plateau is the brightest area on Mars and has not been mapped yet. The South polar areas are still covered with CO_2 frost at the time of this writing, and returns are saturated. The reflectivity maps for the Mapping campaign are presented in Figs. 4.5-4.7. Each map is compiled from about 50 days' data, binned at 0.4° × 0.4° resolution. Data in individual bins were averaged. These maps cover three different seasons. Fig. 4.5 displays data for $L_s = 103 - 134$ (middle of southern winter/northern summer). Most of the reflectivity data are saturated, because the laser energy reaches the maximum output over the course of the mission and the atmosphere is very clear. The boundary of the seasonal frost is at about $40°N$. Fig. 4.6 displays data for $L_s = 164° - 191°$ (beginning of southern spring/northern fall). These data were collected after the threshold of the channel 1 detector was raised to the maximum value. This allowed us to better register high energy returns. The saturation problem was not solved, although the saturation level raised about 5%. The pulse width measurement is unsaturated for practically the whole planet. Fig. 4.7 displays data for $L_s = 204° - 234°$ - the dust storm season. The dust storms are raging in the Margarifter Terra and Ma'adim Valles areas. The North polar area is also very dark in reflectivity due to polar hood activity. The Southern hemisphere starts showing the unsaturated values. The boundary of the seasonal frost is at about $72°S$ at this point ($L_s = 234°$). In some areas on the South polar region MOLA received unsaturated measurement of reflectivity even before the seasonal frost has melted. These regions might be related to the "cryptic" region, observed by the Thermal Emission Spectrometer (Titus et al. (1999)). "Cryptic" region appeared very dark in the broadband albedo channel, but there were no differences in the brightness temperature measurement. It might be interpreted as black or transparent CO_2 ice.

4.4 Calculation of albedo

The primary goal of the reflectivity measurement in the MOLA investigation is to compile the global map of normal albedo of Mars at $1.064\mu m$ wavelength. As for

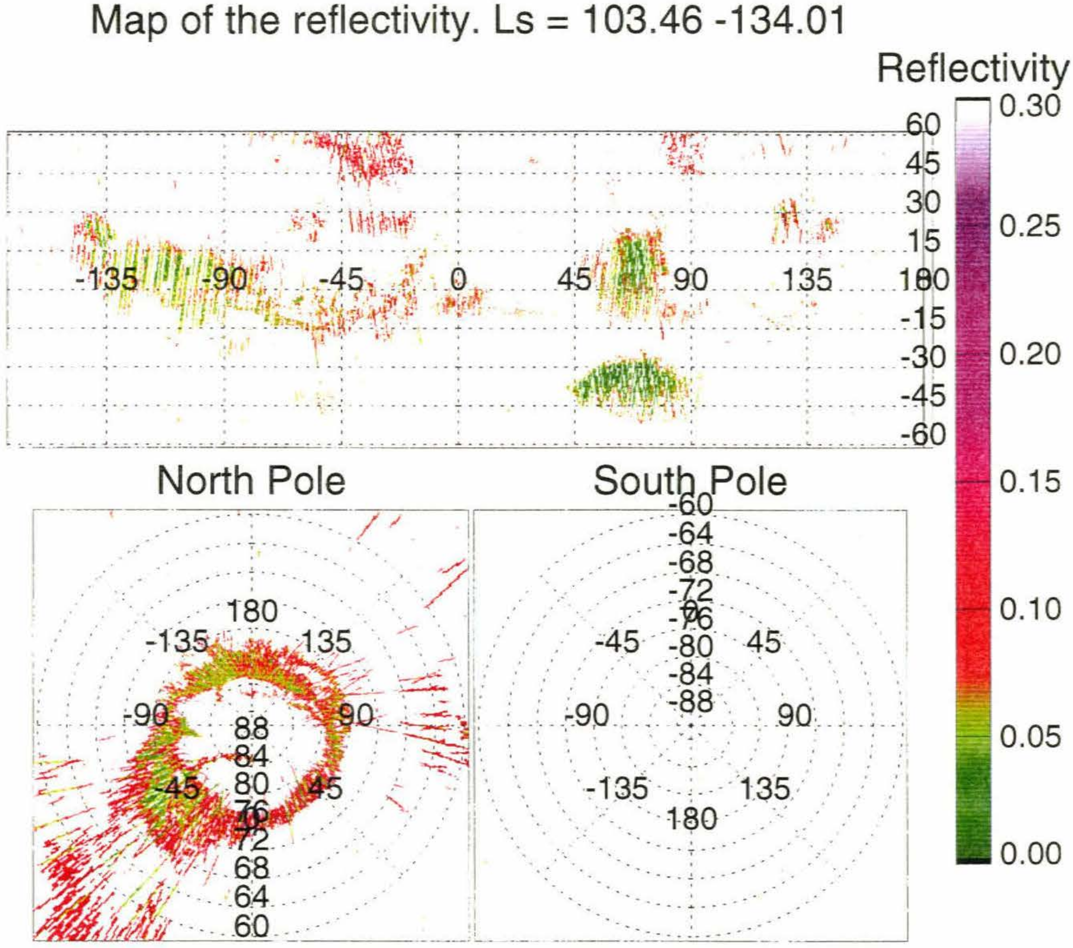

Figure 4.5: Reflectivity map for $L_s = 103° - 134°$. This figure includes data from the first 50 days of the Mapping mission. The laser energy output is high and the atmosphere of Mars is clear. Most of the reflectivity measurement is saturated. The data in the Tharsis region are possibly due to the aphelion water cloud belt. Also visible are Hellas Basin, Syrtus Major and North Polar Dunes. Saturation data is shown as white here, except for the 3° around the poles, where no data exists.

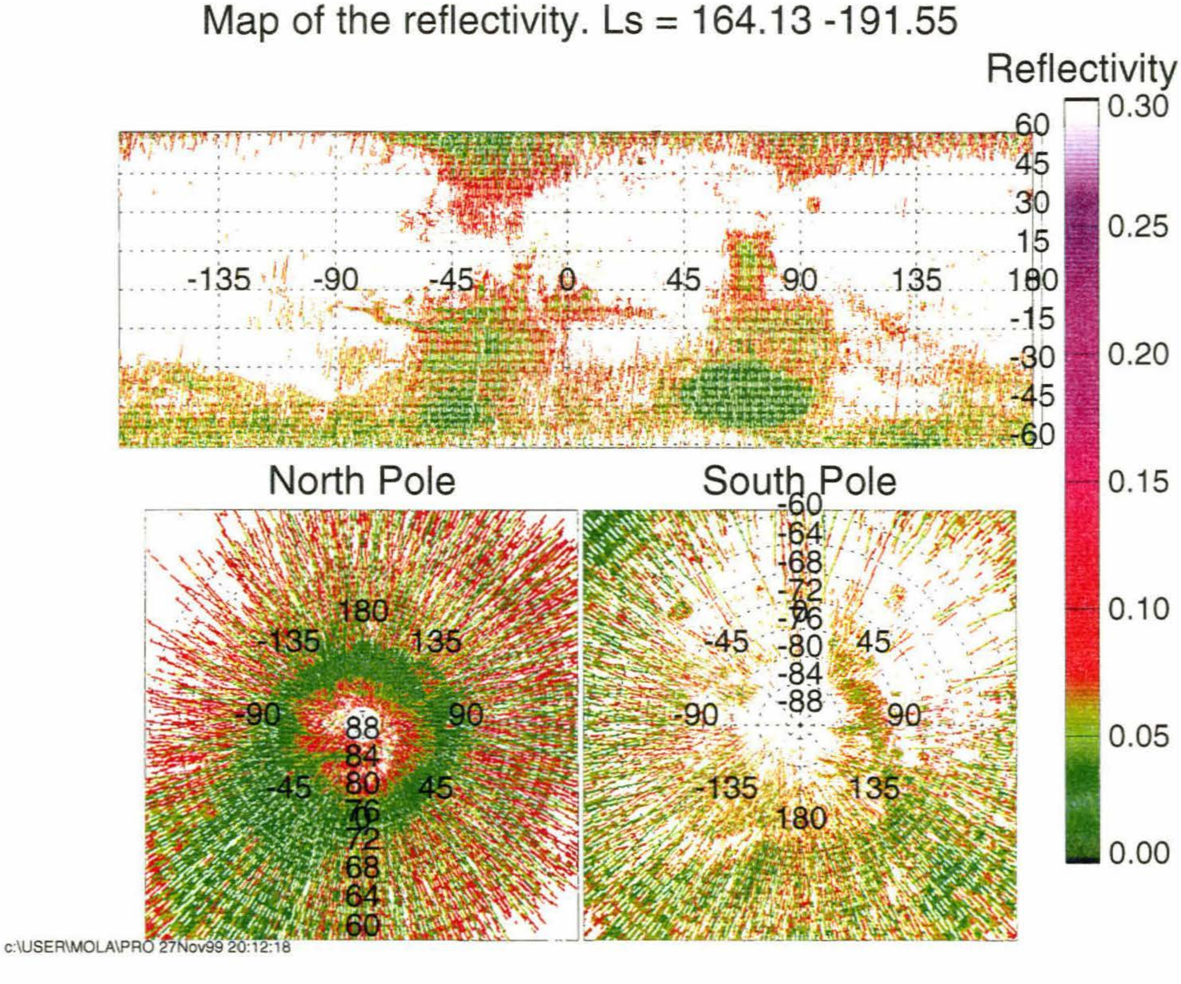

Figure 4.6: Reflectivity map for $L_s = 164° - 191°$. The output laser energy has decreased slightly. The threshold on the channel 1 detector has been increased to raise the saturation level. Average atmospheric opacity has also slightly increased. Now more areas are visible in reflectivity. North Polar Dunes and the residual north polar ice cap are clearly seen. Low reflectivity values in the Southern Hemisphere are possibly due to opacity, created by sublimating seasonal ice cap. Same saturation color as in Fig. 4.5.

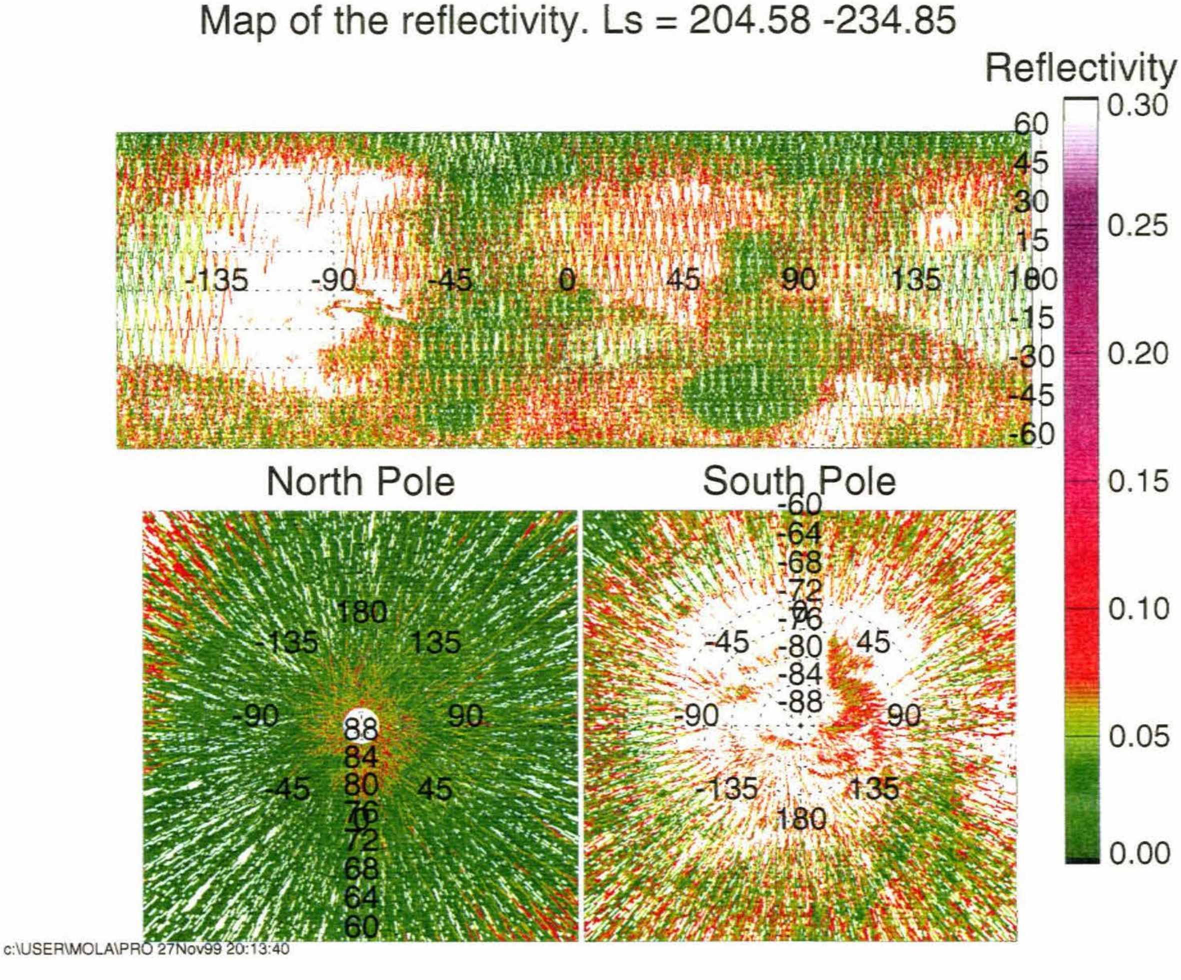

Figure 4.7: Reflectivity map for $L_s = 204° - 234°$. This figure includes the data from the dust storm season. Average atmospheric opacity is at its maximum. Dust storms have been observed in the Margarifter Terra, Ma'adim Valles and in Prometheus Terra regions. The Northern Ice Cap is not seen as bright, due to a cloud cover. Polar night CO_2 clouds have started to appear during this season. In the South Polar regions seasonal ice cap is retreating. Returns are still bright enough, except for the "cryptic region," to saturate the detector. Same saturation color as in Fig. 4.5.

all other nadir-looking instruments, we have to remove the atmospheric attenuation. Opacity in the MOLA experiment is primarily due to the extinction of photons from the laser beam. We will demonstrate calculation of the MOLA albedo using atmospheric opacity simultaneously measured by the TES instrument.

MOLA albedo is calculated from the Beer's law:

$$A_{MOLA} = \frac{R * exp(2 * \tau)}{O}, \tag{4.3}$$

where R - is the measured reflectivity, τ - extinction atmospheric opacity at $1.064\mu m$, O - is the amount of opposition effect. The increase of the returned signal amplitude due to the opposition effect for the MOLA measurement on Mars is not known exactly, but believed to be about a 30% increase over the Lambert backscatter (B. Hapke, personal communication). See discussion in section 4.5. We assume Lambert scattering phase function, which is safe for zero phase angle observations. We will have to use more complicated forms of phase function (Minnaert) for off-nadir observations. We will show in section 4.8 that roughness of the reflecting surface does not significantly affect reflectivity measurements.

To calculate the opacity at the MOLA wavelength, we propose to use the opacity calculated from the depth of the $9\mu m$ dust absorption band (Smith et al. (1999b)). The total atmospheric opacity can be written as a sum of dust and water atmospheric opacities. Gaseous atmospheric opacity can be written as

$$\tau = \int_0^{\inf} N(z) k_e(z) dz, \tag{4.4}$$

where $N(z)$ - particle number density and $k_e(z)$ - extinction coefficient. The latter can be written as

$$k_e(z) = \int_0^{\inf} \pi a^2 N_s(a, z) Q_{ext}(a, n_i, \lambda) da, \tag{4.5}$$

where a - radius of the particles, $N_s(a, z)$ - particle size distribution, Q_{ext} - scattering efficiency, n_i - imaginary index of refraction, λ - wavelength. Clearly, the most important factors for the calculation of the extinction coefficient is the knowledge of the particle size distribution $N_s(a, z)$ at the time of the measurement and extinction efficiency Q. Opacity at any wavelength can be calculated if these parameters are known exactly. It is a very time dependent characteristic and it is very hard to perform a direct measurement for either of them. A number of measurements have been performed to deduce characteristics of the dust particle distribution. A good review of this problem and suggested numbers from various investigations can be found in Pollack et al. (1995). The parameters for the water ice particle size distribution are known very poorly. In this work, we will use the reflectivity data for the season when water ice opacity is in its minimum. The extinction coefficient is usually calculated using Mie formulations of spherical or oblate spherical particles. The exact form of the individual dust particles is not known. The refraction coefficient at each particular wavelength is usually taken from the spectrum of montmorillonite 217b, first suggested by Toon et al. (1977). Clancy et al. (1995) have suggested the palagonite spectrum as an alternative to the montmorillonite. In practice, a scaling factor can be used to infer opacity at the MOLA wavelength from the $9\mu m$ dust opacity, measured by the TES instrument. The scaling of the dust opacity in the infrared compared to the MOLA wavelength is very important for the determination of albedo. It may contribute up to 20% of the error. Depending on the particle size distribution, this ratio may vary very widely. For instance, the contribution of the submicron particles is poorly known. It affects solar wavelengths opacity much stronger than in the infrared. Moreover, water haze particles can be a major source of opacity, especially during the aphelion. It should be added to the dust opacity. Observational evidence so far consists of the simultaneous observations, in time and place, by the Viking Orbiters and Viking Landers. Martin (1986) compared $9\mu m$ dust opacities calculated from the IRTM instrument with the Viking Lander's visible opacities for the time period between $L_s = 180^\circ - 270^\circ$. He determined that the ratio of 2.5 is most consistent with opacity data for that period. Clancy et al. (1995) provided a separate measurement of this key opacity ratio based on the analysis of Emission Phase Function (EPF) observations in the IRTM solar and $9\mu m$ channels. Their derived ratio is > 2 for visible opacities less than 1 and appear to increase with increasing opacity. However, the authors quote high uncertainties in the visible/IR-ratio for high values of visible opacity (> 1). Recently, Toigo and Richardson (1999) reanalyzed observations by Martin (1986) and supported the value of 2.5 for the visible to IR opacity ratio during the dust storm season. In addition, they have found that water ice haze may contribute up to 50% of total opacity during northern spring and summer seasons. This suggests that water ice contributes to the visible opacity much more than it was thought before. The deviations of the ratio during the mapping mission can be illustrated by comparing $9 \mu m$ opacity with the MOLA $1 \mu m$ opacity. In Fig. 4.8 we show the visible-to-IR ratio as a function of season from $L_s = 100°$ to $L_s = 240°$, measured

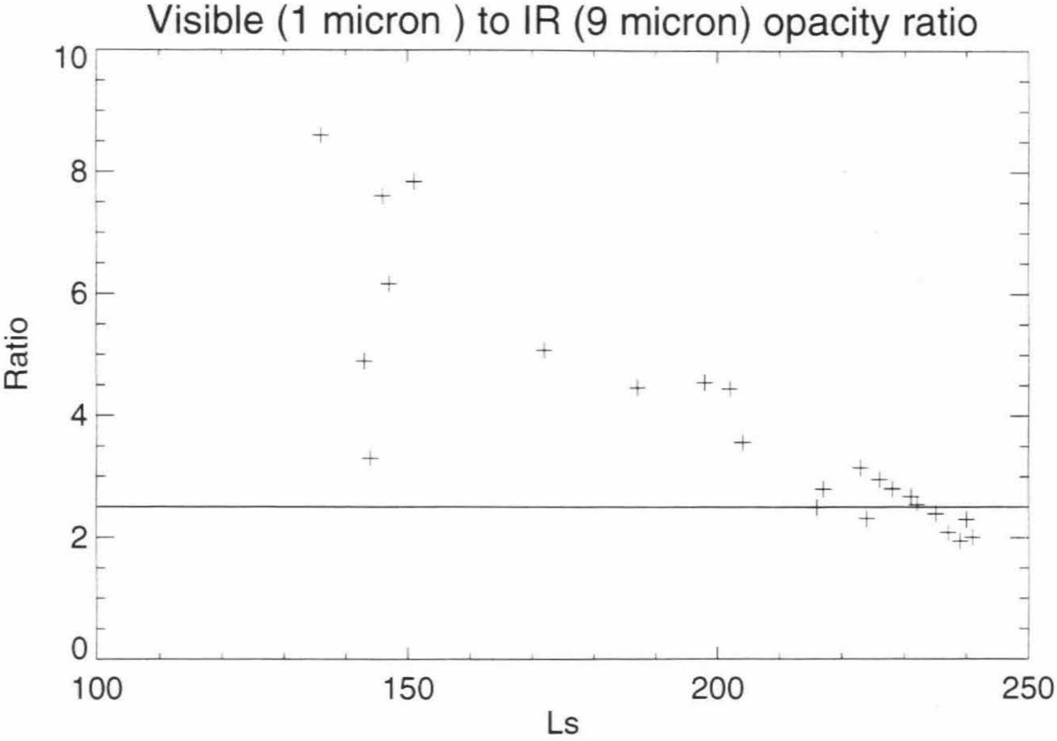

Figure 4.8: Visible ($1 \mu m$) total opacity to IR ($9 \mu m$) dust opacity ratio during the mapping period of observations. The high values of ratio during the southern winter are due to enhancement in small submicron particles in the atmosphere. Possibly, water ice clouds are composed of small, reflective particles that do not contribute to the $9 \mu m$ dust opacity. In the dust storm season ($L_s = 220° - 240°$) the ratio is very close to 2.5. Decreasing trend in this season is due to increasing number of larger dust particles. Data are from $1° \times 1°$ square in the Syrtus Major area (22°N, 295°W).

in the Syrtus Major area (22°N, 295°W). MOLA opacity data were matched to the $9\mu m$ opacity data. The algorithm for calculating the opacity from the MOLA reflectivity measurement using the Plescot and Miner (1981) albedo dataset is described in section 4.5. Clearly, the ratio is very high during the southern winter, when extensive water ice cloud belt is forming in the equatorial regions. The high values of ratio are due to enhancement in small submicron particles in the atmosphere relative to the dust storm season period. In the latter season ($L_s = 220° - 240°$) the ratio is very close to 2.5.

For this work we decided to accept the value of 2.5 for the visible-to-IR opacity ratio. We selected MOLA data from the dust storm season ($L_s = 220 - 240°$) for our albedo calculations. Toigo and Richardson (1999) showed, based on the IRTM opacity data set, that during this season water hazes contribute a minimal fraction of the dust opacity. We assume that the dust is the only scattering aerosol in the atmosphere during this time. The TES instrument is able to measure water ice opacity, and we hope to use it to justify our assumption.

Full dataset of TES opacities was not available at this time. We were only able to demonstrate this algorithm for a small region on the planet. We chose Syrtus Major as our test region. Returns from this region were mostly unsaturated. For the course of the mission, there were no significant dust storm activity observed in Syrtus Major during dust storm season. We compared MOLA derived albedo and the Plescot and Miner (1981) albedo dataset. The results are shown in Fig. 4.9. MOLA albedo was calculated assuming the visible to IR opacity ratio of 2.5 and 30% returned signal enhancement due to the opposition effect. Plescot and Miner (1981) albedo was corrected for wavelength and atmospheric effects (Clancy and Lee (1991)). All these correction are discussed in detail in the next section. The general agreement is very good. The results of MOLA albedo calculations are consistent with the Viking IRTM derived albedo data set. The variations of the particle size distribution of the dust in the atmosphere are the most important source of error, which can constitute as much as 30% of the albedo value. However, comparison with the Viking albedo data in Fig. 4.9 suggests that this error is much smaller. We hope to constrain the error

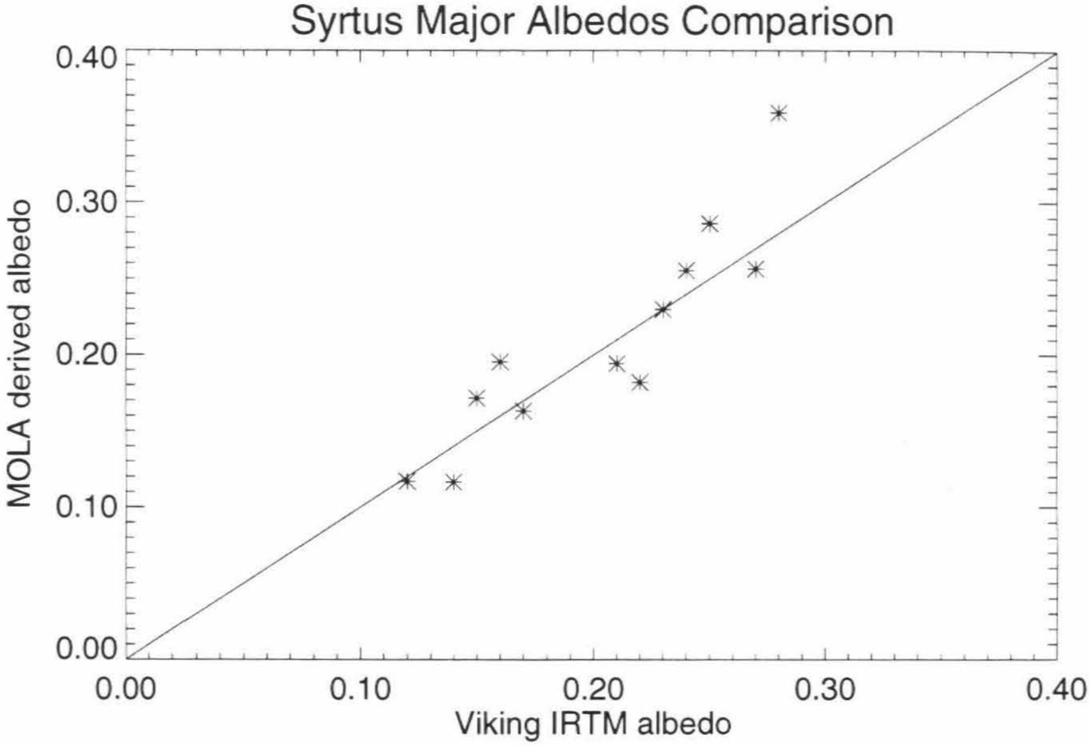

Figure 4.9: Comparison of MOLA albedo and Viking IRTM albedo. The solid line is the locus of equal albedos. Only data from the dust storm season ($L_s = 220^\circ - 240^\circ$) were used to construct this picture. Data come from the Syrtus Major region ($20^\circ - 26^\circ$N and $290^\circ - 300^\circ$W). MOLA albedos were corrected for the opposition effect. The Viking IRTM data were corrected for the wavelength and atmospheric effects (Clancy and Lee (1991)). Spectral properties of the surface materials and variability of the particle size distribution in the Martian atmosphere are the major sources of error.

by analyzing many crossovers or nearby passes. For example, during the dust storm season there can be up to 3 tracks crossing 1° × 1° square. Much more data from the mapping orbits will be available for similar processing. The presented algorithm can be employed for putting together a global albedo map of Mars at the MOLA wavelength.

4.5 Calculation of atmospheric opacity

Reflectivity is a product of the albedo of the surface and atmospheric transmissivity. In the previous section, we calculated surface albedo using the TES $9\mu m$ dust opacity as a proxy for the opacity at $1\mu m$ wavelength. Below, we will demonstrate the use of the Plescot and Miner (1981) albedo data set to derive atmospheric opacity.

MOLA laser presents a unique opportunity to calculate the total atmospheric opacity. However, albedo at the MOLA wavelength ($1.064\mu m$) should be known. The best available data sets of MOLA global albedo were discussed in the section 4.2.1. The most extensive dataset is the Plescot and Miner albedo, compiled from the observations by the broadband bolometric channel of the IRTM instrument. A similar dataset can be compiled from the bolometric channel at the TES instrument. Digital data for TES albedo were not available at the time of this writing. The Hubble telescope observations by Bell et al. (1999) are the closest in wavelength. Practically none of the authors have addressed the question of an atmospheric contamination. Plescot and Miner (1981) state that they have used the clearest period of the Martian atmosphere to compile the dataset. Clancy and Lee (1991) have empirically deduced atmospheric corrections for the albedo from the Emission Phase function observations. A similar correction can possibly be applied to the HST observations. The amount of atmospheric scattering will depend on the total optical depth during the season of observations. TES solar albedo channel has the same problems, although atmospheric correction can be introduced using the atmospheric opacities derived simultaneously (Smith et al. (1999b)). The use of radiometrically calibrated images is also problematic. Besides the lightning effects (shadows, bright cliffs) they are affected by the dust scattering and illumination. Only very clear images with favorable geometry can be used, such as in case of Valles Marineris described below. We hope that we will be able to compile an albedo map from the MOLA reflectivity measurement and use it as the base map of the opacity calculations.

All of the MOLA observations are performed at 0 phase angle. Consequently, the laser returns are enhanced by the opposition effect. The amount of this effect is not known, but is probably about 30% (B. Hapke, personal communication).

4.5.1 Corrections

In this study we adapted the Plescot and Miner (1981) albedo dataset. Some corrections have to be applied to this dataset before we can use it as a base for the opacity calculations.

Bolometric channel bandwidth range from $0.3\mu m$ to $3\mu m$. It can be shown that integrated albedo over this range will be the most heavily weighted by the spectral properties at the $0.6\mu m$. Viking imaging camera had a central wavelength of $0.6\mu m$. Reflectance spectrum of Mars has a slope in the region $0.5\text{-}0.7\mu m$. Fig. 4.10 displays visible spectrum of Mars for the visible and near-IR wavelength. The reflectance is brighter at the MOLA wavelength than at the Viking camera wavelength. We suggest to apply a scaling factor of 1.2 to correct for the reflective properties at the MOLA wavelength for dark terrains. This number is higher for brighter terrains. Any error in this scaling factor will introduce an offset for the resulting MOLA opacity. This value correlates well with the ratio of corresponding peaks in the bimodal distribution of Martian albedo observed by IRTM distribution and the HST distribution. Plescot and Miner (1981) albedo distribution peaks at .16 and .27 for dark and bright terrain. HST albedo distribution from Bell et al. (1999) peaks at .18 and .36 correspondingly.

The opposition effect for the MOLA wavelength has not been studied in any detail. Hapke et al. (1998) have investigated this effect in detail and arrived at the conclusion that it is caused by both coherent backscattering and shadow hiding in roughly equal amounts. Researchers have reported on efforts to determine the opposition effect

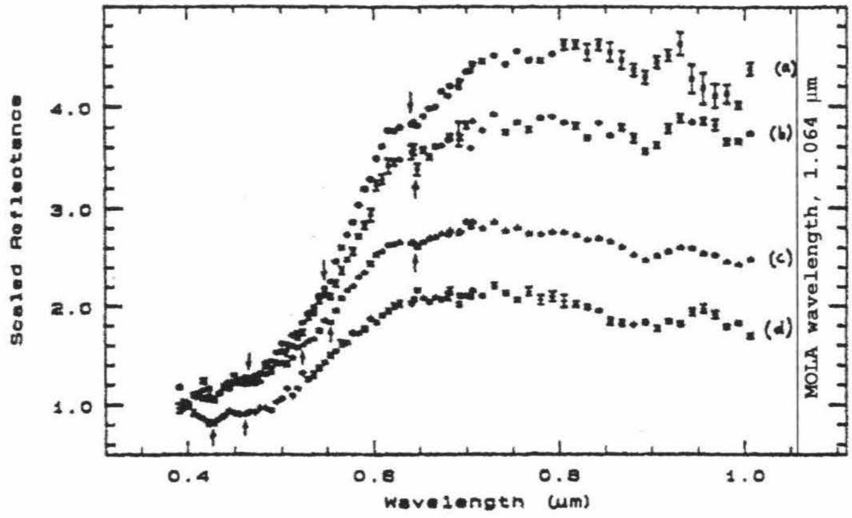

Figure 4.10: Martian reflection spectra for the region of $0.3\mu m$ to $1.0\mu m$. Dark features are characterized by a bottom line (d) and bright features are characterized by a top line (a). (figure from Bell et al. (1989))

for lunar samples. Various estimates of the amount of this effect are suggested by laboratory (e.g., Nelson et al. (1998)) and theoretical studies (e.g., Shkuratov et al. (1999)). Magnitude of the opposition effect varies, depending on the microphysical structure of the surface and may vary from 30% to 50%. In this work, we adopt value of 30% for the opposition effect for all surfaces on Mars.

We suggest the following formula for calculation of the albedo at the MOLA wavelength from the Plescot and Miner dataset:

$$A_{MOLA} = A_{PM} * C * S * O, \tag{4.6}$$

where A_{PM} - albedo from value from Plescot and Miner (1981) dataset, C - atmospheric correction from Clancy and Lee (1991), S - spectral correction and O - magnitude of the opposition effect, taken to be 1.3.

Finally, the opacity can be calculated using the Beer's law:

$$\tau_{MOLA} = -0.5 \times \log\left(\frac{R}{A_{MOLA}}\right), \tag{4.7}$$

where τ_{MOLA} - total atmospheric opacity at the MOLA wavelength, R - measured reflectivity and A_{MOLA} - albedo at the MOLA wavelength, estimated from Equation 4.6.

For this work we have decided to use mostly the Plescot and Miner dataset and perform only one case study with the Mars Viking images to compare the results. To use the Viking MDIMs images we will apply a geometrical correction as described in Thorpe (1981). Moreover, we will assume an atmospheric scale height of 10km and account for it in the airmass calculation. These images also have an atmospheric component from the scattering by the suspended aerosols. To minimize the atmospheric bias, we have used Viking images at a given location which were taken when the atmosphere was the clearest, i.e., at L_s = 30° - 50°. Atmospheric opacity was taken from Viking Lander observations (Colburn et al. (1989)) for the same season. We did not use images with high phase angles (> 50°) to avoid brightening of the surface albedo by the aerosols and surface phase function effects. Low phase angle allow us to minimize forward scattering effects of the dust in the images. Since the wavelength of the red filter of Viking Orbiter Camera is 0.55 μm to 0.70 μm , we had to use the Mars average scaling factor of 1.2, same as for the bolometric albedo maps, to convert albedo at the wavelength of the red filter to 1.064 μm . This is consistent with spectroscopic observations of the average Martian surface in visible and infrared wavelengths (Soderblom (1992)), as well as with newly published composite spectra of Mars by Erard and Calvin (1997).

4.6 Examples of opacity calculations

We have used the procedure for opacity calculations described above to calculate opacities for selected regions on Mars. The seasonal trends of the opacity can be best illustrated for some very dark regions, where MOLA has unsaturated opacity data since the start of the mission. Comparison with Viking Landers optical depth is also helpful to check MOLA derived opacity against other opacity data. We have chosen two places: Acidalia Planitia (47N, 33W) and Syrtus Major (22N, 295W).

The latitudes were chosen to be similar to the latitudes of the Viking Landers. No unsaturated reflectivity data were available for the landing sites until $L_s = 200°$. Unsaturated reflectivity data were selected for a $3° \times 3°$ square in latitude and longitude, which corresponds to $\approx 128km \times 180km$ rectangle on the surface. The albedo of the surface for both regions was taken from Plescot and Miner (1981) dataset and corrected to the MOLA wavelength using Equation 4.6. The results are shown in Fig. 4.11. Only daytime data were selected for MOLA and Viking Lander. The data for

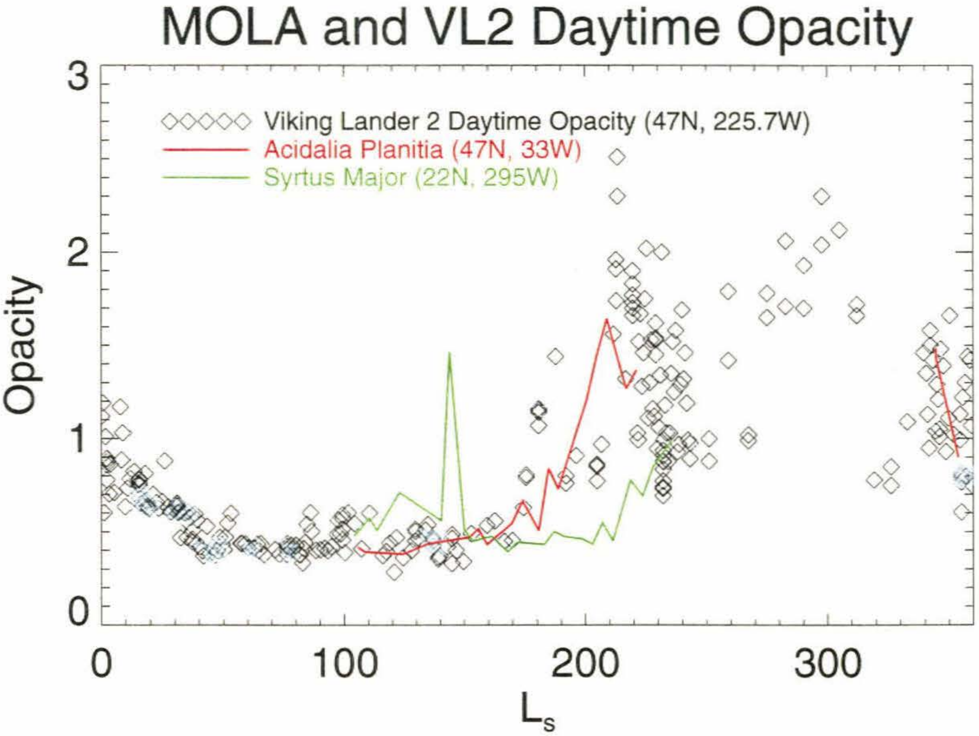

c:\USER\MOLA\PRO 08Nov99 07:44:04

Figure 4.11: Comparison of MOLA and Viking Lander 2 daytime opacity. Data are collected in $3° \times 3°$ box in latitude and longitude. Viking Lander coordinates are $47°N, 225°W$. MOLA opacity was calculated from the reflectivity measurement using the method described in section 4.5. The Acidalia Planitia data (red line) follows the same trend as the Viking Lander Opacity. The spike in the Syrtus Major data (green line) at $L_s = 143°$ is possibly a local dust storm and constitutes an average of about 300 individual measurements. Acidalia Planitia data for $L_s = 300°$ is taken during the SPO orbits.

Acidalia Planitia clearly follows the same trend as the Viking Lander opacity. The major source for the opacity in this region are possibly water ice clouds, which start to condense as fall sets in in the Northern Hemisphere. The Syrtus Major opacity start to rise only when the dust storm season starts, i.e., around $L_s = 220°$. The spike at $L_s = 143°$ is real and constitutes an average of about 300 individual measurements. A local dust storm lasted over this region for a very short time. Mars Pathfinder Lander (Smith and Lemmon (1999)) has performed observations of the atmospheric opacity at several wavelengths, including 986nm, which is very close to the MOLA wavelength. They concluded that opacity at this wavelength is similar to that reported by the Viking Landers. Extinction efficiencies for Viking Landers, Pathfinder and MOLA wavelengths are not significantly different for the particle size distribution that exists on Mars. We do not expect opacities to differ significantly.

Unlike solar reflectance measurement instruments, MOLA carries its own "light source." The night viewing is as good as the daytime. Fig. 4.12 displays daytime and nighttime opacities for the regions discussed above. Due to orbit characteristics of the MGS, we were not able to pass over the same region within one or two days. Within 10-15 days between the measurements, opacity can change not only due to the condensation of water ice clouds, but also due to global dust opacity changes. From Fig. 4.12 we can not observe any significant difference between daytime and night opacities for the period of observations.

4.7 Scale height calculation

MOLA has obtained a large number of unsaturated opacity measurements on the slopes of large topographic structures, such as Olympus Mons, Alba Patera, Valles Marineris and Hellas Basin. Slopes on these structures are fairly small ($\approx 2°$, with the exception of Valles Marineris), so they do not affect assumptions in the calculation of the reflectivity from the returned energy measurement. The reflectivity increases as the signal comes from higher and higher terrain, because there is less scattering by the atmospheric dust. This presents us with an opportunity to calculate the aerosol scale height at these locations. We will still need an estimate of albedo of the topographic

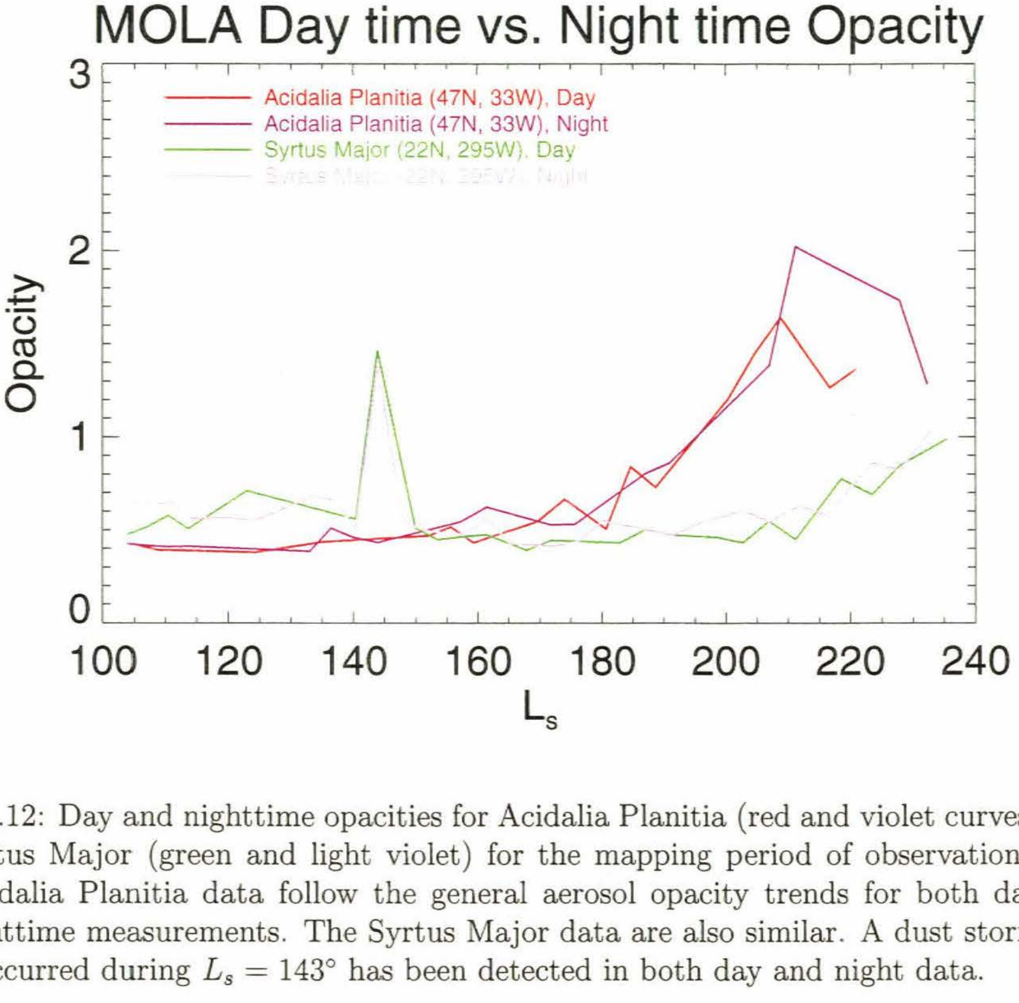

Figure 4.12: Day and nighttime opacities for Acidalia Planitia (red and violet curves) and Syrtus Major (green and light violet) for the mapping period of observations. The Acidalia Planitia data follow the general aerosol opacity trends for both day and nighttime measurements. The Syrtus Major data are also similar. A dust storm which occurred during $L_s = 143°$ has been detected in both day and night data.

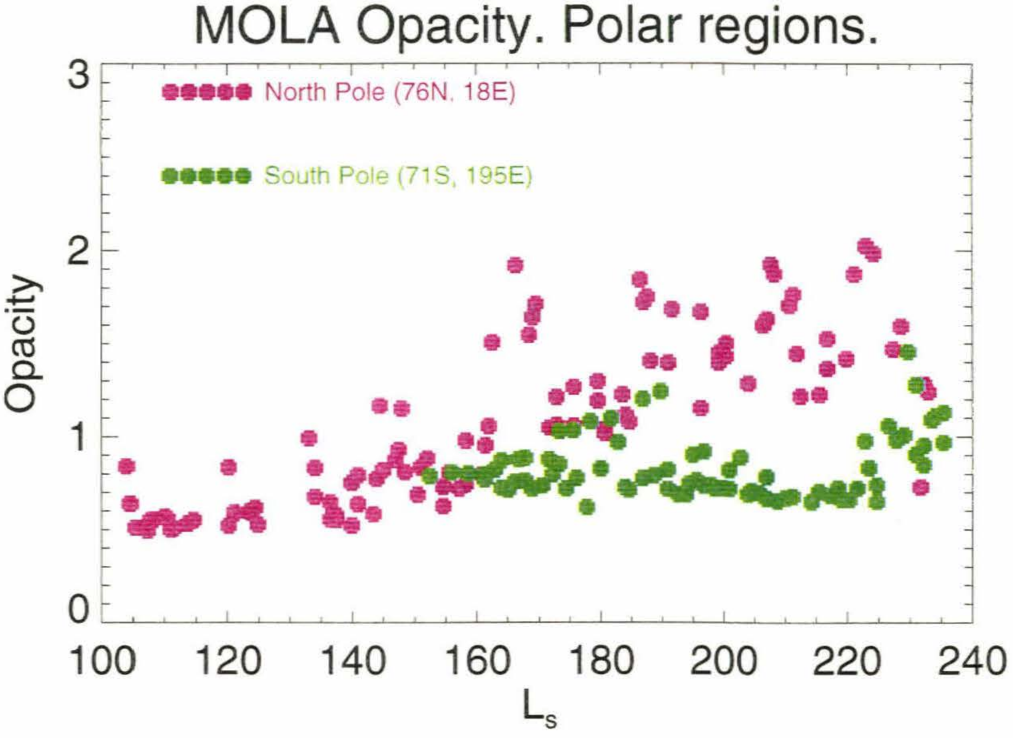

Figure 4.13: North and South polar region opacities. North polar region data (blue dots) follow the seasonal trend. Opacity increases towards the fall. More water vapor condenses in the atmosphere, as temperatures become lower. Note the outliers which are apparently over the average trend. Those are possibly local dust storms or cyclones. Large atmospheric systems were passing over the cap and were observed by the MOC. The South polar data (green dots) starts only at about $L_s = 150°$ and stays the same over the observed time, except for the period $L_s = 175° - 190°$. This opacity increase is possibly due to the formation of the South polar hood.

feature. We will use the datasets and corrections discussed in section 4.5 as a source for this estimate.

4.7.1 Olympus Mons

At the start of the mapping orbits ($L_s = 103°$), MOLA has returned a significant amount of unsaturated returns across Olympus Mons. This surprised us because not only does the laser beam propagates through a thin atmosphere, but this is one of the brightest and highest places on the planet. Possibly the cause of the opacity are bands of daytime clouds, which form during the summertime. Clouds were first seen around $L_s = 103°$ and disappeared by $L_s = 130°$. These clouds are the source of significant opacity and can be seen in the Tharsis region in Fig. 4.5. It is likely that the equatorial cloud belt has existed before the start of the mapping campaign. MOC and TES data confirm this observation.

We located two tracks on the flanks of the volcano. They both lie on the northern slope and the local time is 2 pm. The original reflectivity data for track 10097 is shown in Fig. 4.14. The upper panel shows the elevation profile, and the lower panel displays observed reflectivity and pulse width. The exponential trend in the reflectivity data can be seen in this data. The flat part of the curve is the saturation level. Using the Plescot and Miner albedo dataset, it is now easy to calculate the opacity. Dependence of the opacity vs. elevation can be used to find the aerosol scale height at this location. Fig. 4.15 illustrates change of opacity with height for two tracks, which lie over the volcano. Dependence of optical depth τ vs. height z can be represented in form

$$\tau(z) = \tau_0 exp\left(-\frac{z - z_0}{H}\right), \tag{4.8}$$

where τ_0 is the total opacity atmospheric opacity at elevation z_0. We can fit this function to the data displayed in Fig. 4.14 and find values of τ_0 and H. Inferred scale heights have a similar structure. From 10 to 18km (data is saturated over 18km altitude, so no scale height calculation were possible) opacity follows a very nice exponential law with scale heights around 10km (1593 : 9.5km, 10097 : 10.7km).

Below 10 km down to 6km, where data existed, negative constant or negative scale heights are observed. The opacity through the cloud is possibly decreasing. The cloud possibly becomes thinner towards the edge.

4.7.2 Alba Patera

Four tracks (339, 340, 358 and 394) with a good quality reflectivity data were obtained over the Alba Patera during the Science Phasing Orbit Period ($L_s = 338° - 352°$). All tracks were acquired around 7am local Martian time. No unsaturated data exists yet for the mapping orbit period. We have applied the same approach as discussed before for the Olympus Mons. The resulting opacity vs. height dependencies are shown in Fig. 4.16. Opacity distribution with height is similar for tracks 340 and 394. The vertical structure of opacity is interesting and appear to have two or three different scale heights. Best fit scale heights for track 339 are 0.87 and 2.94km. For track 394 there are three different scale heights: 1.15, 1.84 and 3.54km. These scale height breaks are possibly due to structure of the atmospheric boundary layer. Dust, which is the major scatterer here, is not distributed uniformly. It is most concentrated in the first kilometer from the ground, where scale heights are about 1km. Over 4km the aerosols seem to be uniformly distributed (the highest part of the track 394). The opacity for the track 358 is higher than for other tracks, because a local dust storm occurs nearby, just north of the Alba Patera. Increase in the opacity is most probably due the dust particles. The inferred scale heights are, however, similar to all other calculations.

4.7.3 Hellas Basin

The deepest and largest crater basin on Mars has the largest amount of unsaturated reflectivity measurements due to high concentration of aerosols. We present observation for three different seasons $L_s = 105°, 143°, 172°$. Scale height fits are shown in Figs. 4.17 and 4.18. We chose the northern rim of the basin as a location for our measurement. The height difference is almost 4 km. All observations were performed

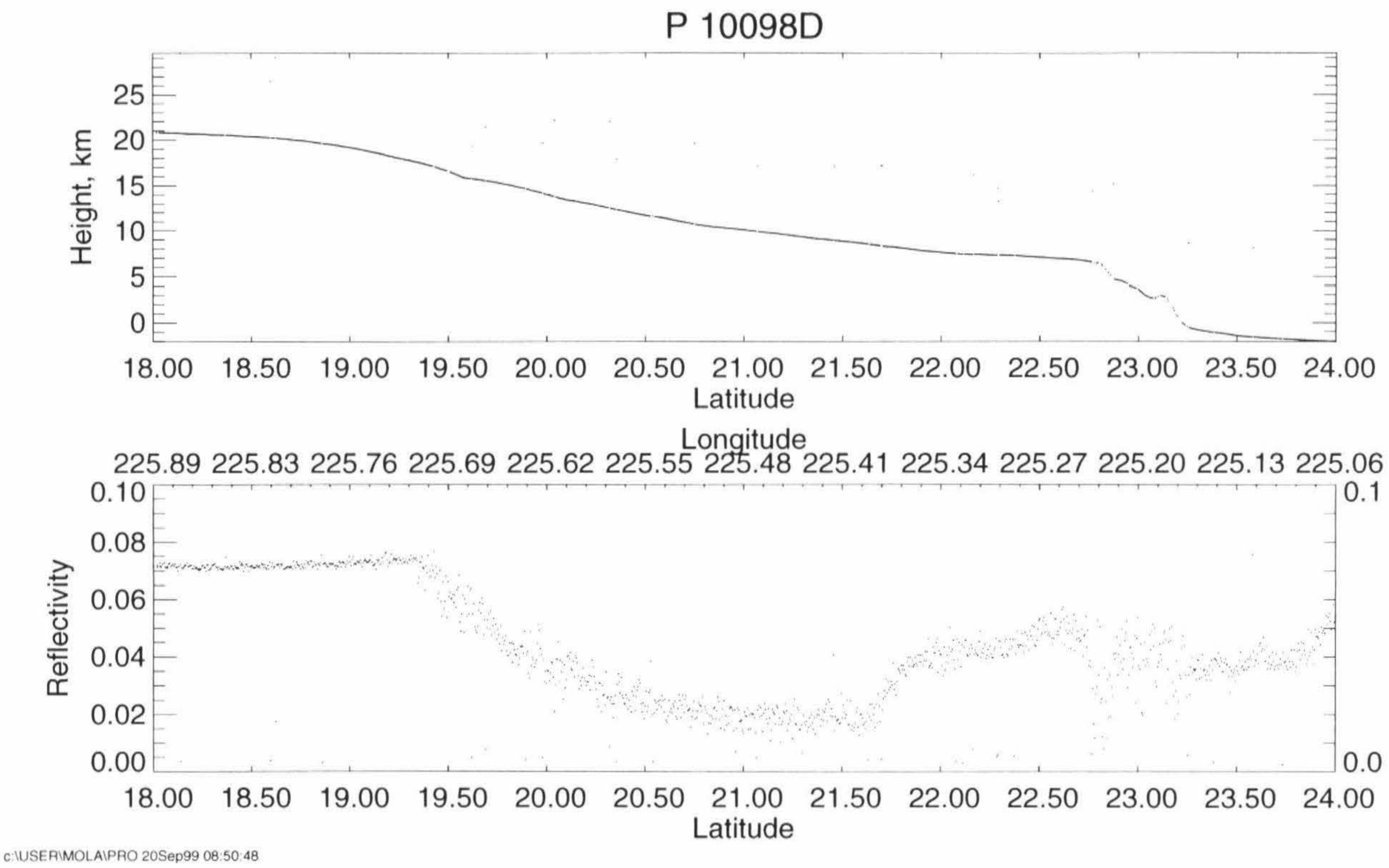

Figure 4.14: Topography (upper panel) and reflectivity (lower panel) data over the Olympus Mons volcano for orbit 10097. The track is located on the northern slope of the volcano. This data was taken at $L_s = 110°$. Note exponential like rise of reflectivity with height. The data is saturated over 18km.

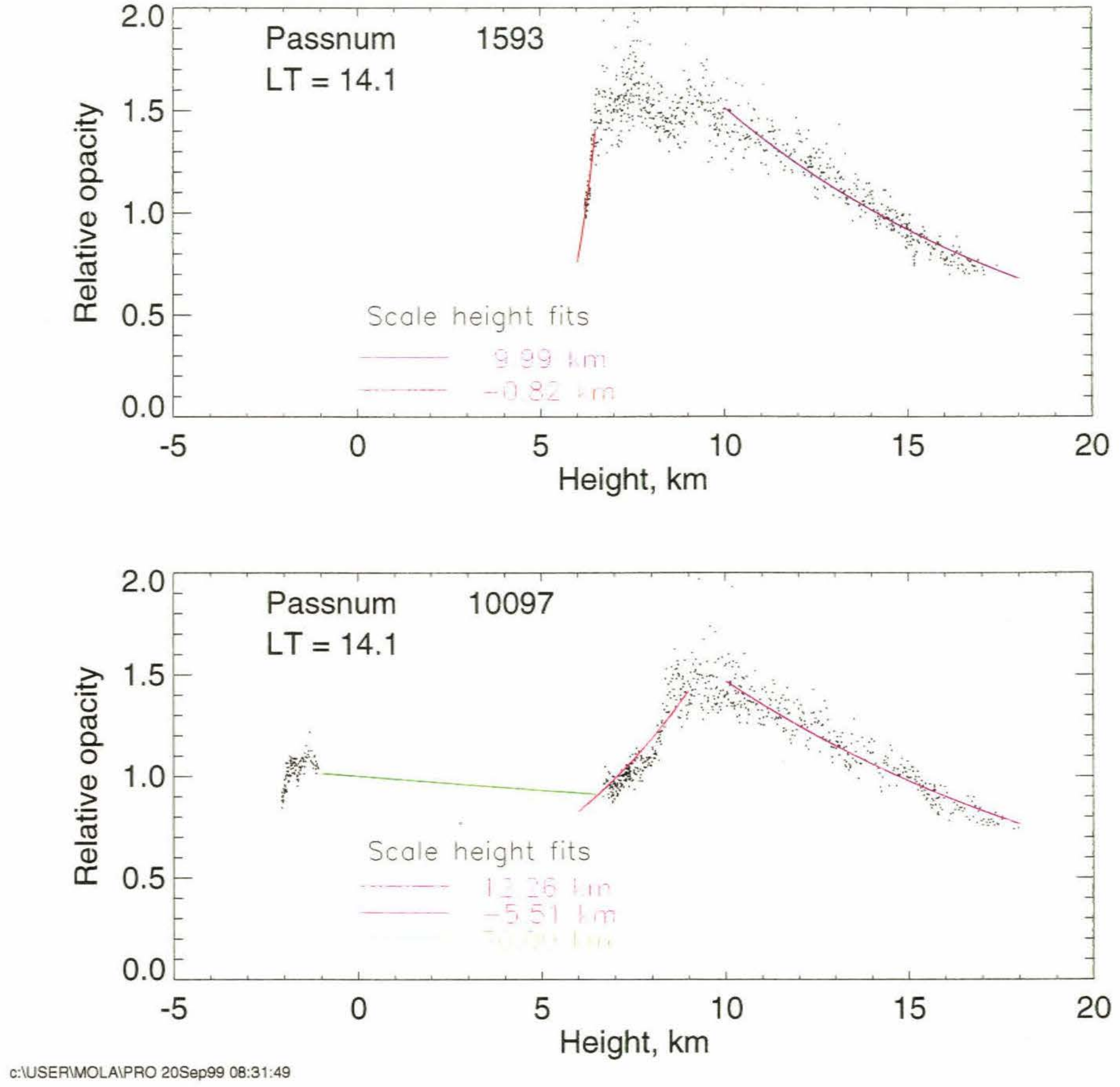

Figure 4.15: Opacity vs. depth dependence for the tracks over the Olympus Mons volcano. Two tracks are shown taken during $L_s = 110°$. Both curves can be fit using a scale height of about 10km. The negative scale heights below 6km elevation possibly correspond to an inversion layer in the atmosphere or the edge of the cloudy region. High scale height values (70km) correspond to a uniformly mixed layer in the atmosphere.

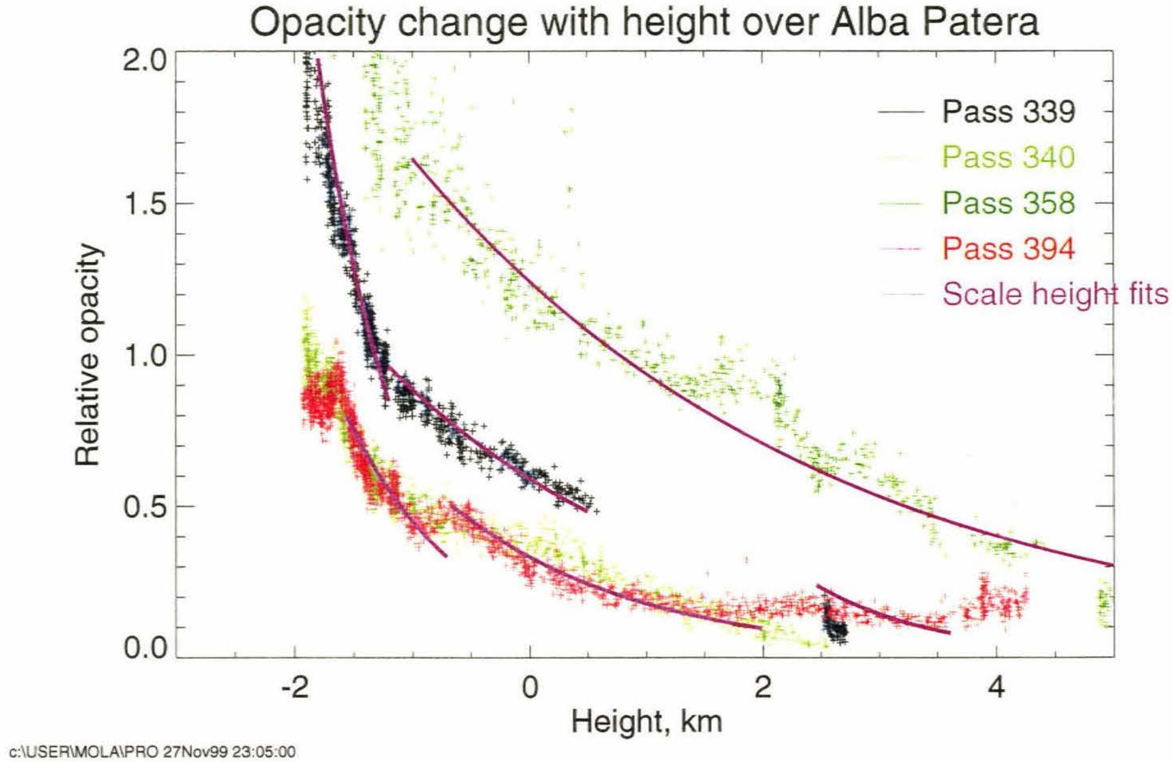

Figure 4.16: Opacity vs. height dependence for the Alba Patera volcano. All tracks were taken during the Science Phasing campaign ($L_s = 338° - 352°$). Tracks are best fit with different segments of scale heights, ranging from .7 to 3.5 km. For example, opacity variation with height for track 339 is best fit with scale heights of .7 and 2.5km. Aerosols are most concentrated within first km from the surface. Opacity for the track 358 is higher due to the dust storm, occurring at the time of observation north of the Alba Patera. The derived scale height for track 358 is 3.5km.

either at 2 am or 2 pm local time. The Hellas Basin is historically known to be very dusty. During the southern winter the floor of Hellas was covered with the frost which we accounted for in the opacity estimate. Evaporating CO_2 frost and clouds contributed to the opacity and scale height observations as well.

Table 4.1 summarizes the observations. The lowest scale heights were seen during the southern winter. CO_2 or water clouds condense near the ground and contribute to the opacity. The data taken at night (2 am) tends to have larger scale height than the daytime observations. Scale heights derived from the data around $L_s = 143°$ are maximum for this dataset. Atmosphere warms up and clouds disappear. Dust is raised higher in the atmosphere. $L_s = 172°$ are lower than that around $L_s = 140°$. We could not observe any significant day/nighttime variations in scale height magnitude (see Table 4.1). Optical density of the atmosphere near the rim of the Hellas Basin does not depend on the time of day, and it is mostly due to the dust particles suspended in the atmosphere. However, we found that wintertime and late spring nighttime scale heights are statistically lower than daytime. Seasonal variations in the dust content and large scale atmospheric processes (such as storms) define variations of opacity.

Feature name	L_s	Local time	Scale height, km	Comments
Olympus Mons	105	2 pm	9.5	Water Cloud on the northern
	111	2 pm	10.7	flank of the volcano
Arsia Mons	338	7 pm	0.7,2.9	Aerosols are very close
	352	7 pm	3.5	to the surface
Hellas Basin	105	2 am	3.5 ± 0.8	Hellas is covered
	105	2 pm	3.0 ± 0.6	by the seasonal frost
	143	2 am	5.0 ± 1.1	Frost starts to sublime
	143	2 pm	5.7 ± 2.2	Polar hood forming
	172	2 am	4.5 ± 1.4	Bare ground
	172	2 pm	5.0 ± 1.3	Clear atmosphere

Table 4.1: Atmospheric scale height observations

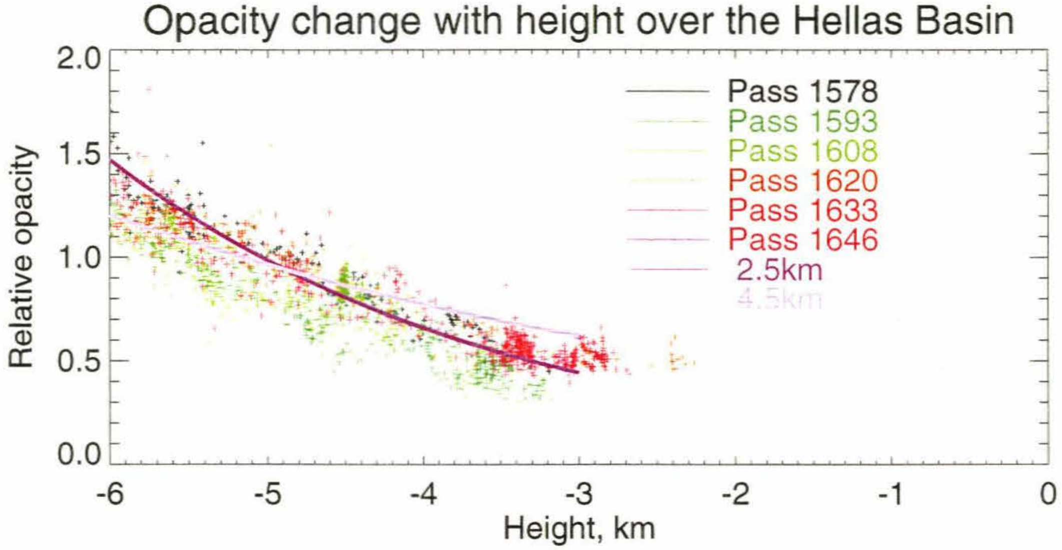

Figure 4.17: Opacity vs. scale height observations for the Hellas basin. Six tracks shown were obtained during $L_s \approx 105°$. Local time of all tracks is 2 am or 2 pm. The opacity data have similar values consistent from track to track. Also shown are the scale fits for tracks 1578 (2.5km) and 1646 (4.5km). These values are representative of the calculated scale heights.

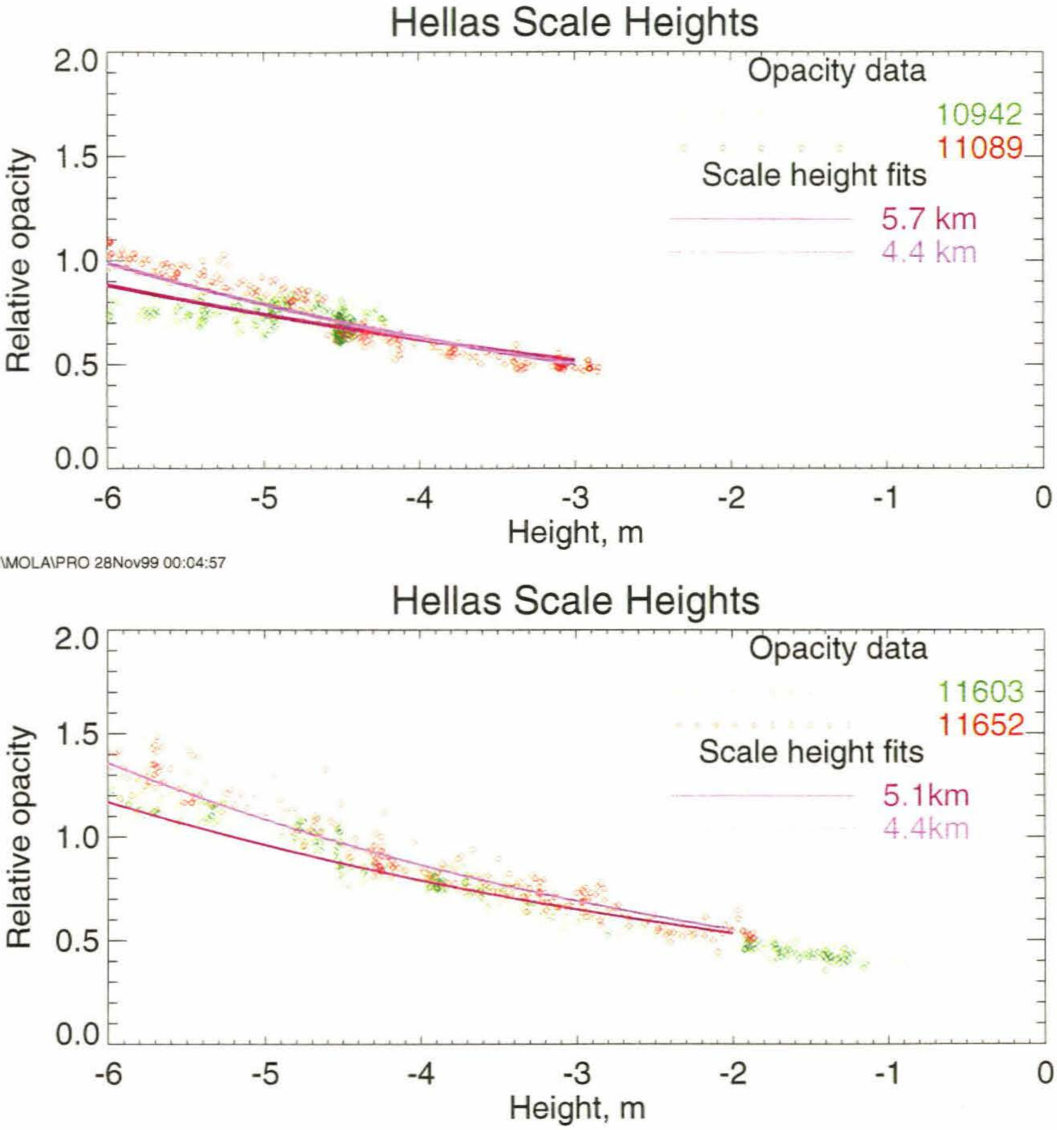

Figure 4.18: Opacity vs. scale height observations for the Hellas basin. The upper panel shows observations for $L_s = 142°$, the lower panel shows observations for $L_s = 172°$. The inferred scale heights are higher for the $L_s = 142°$, possibly because dust is spread out from the surface higher into the atmosphere. Higher opacity values are characteristic for the lower panel data ($L_s = 172°$). Dust is raised from the surface by winds and creates additional opacity, especially near the bottom of Hellas.

4.8 Opacity in Valles Marineris

During passes 26 and 35 MOLA ground tracks crossed Valles Marineris, the deepest and the largest canyon system on Mars. Using Viking Color MDIMs (sequence 583a) as described above to correct for the albedos of the canyon floor and walls, we were able to estimate opacity over the canyons. The resulting opacity over the canyons is plotted in Fig. 4.19. It is clear from the figure that the opacity inside the canyons is greater than the opacity on the top, apparently due to atmospheric aerosols inside the canyons. Roughness on the bottom of the canyons plays a little role in the opacity estimate. Corresponding pulse width data, which is a characteristic of surface roughness at about 100m scale, shows that there is no correlation with average opacity (Fig. 4.19), though the standard deviation increases, particularly on the canyon walls.

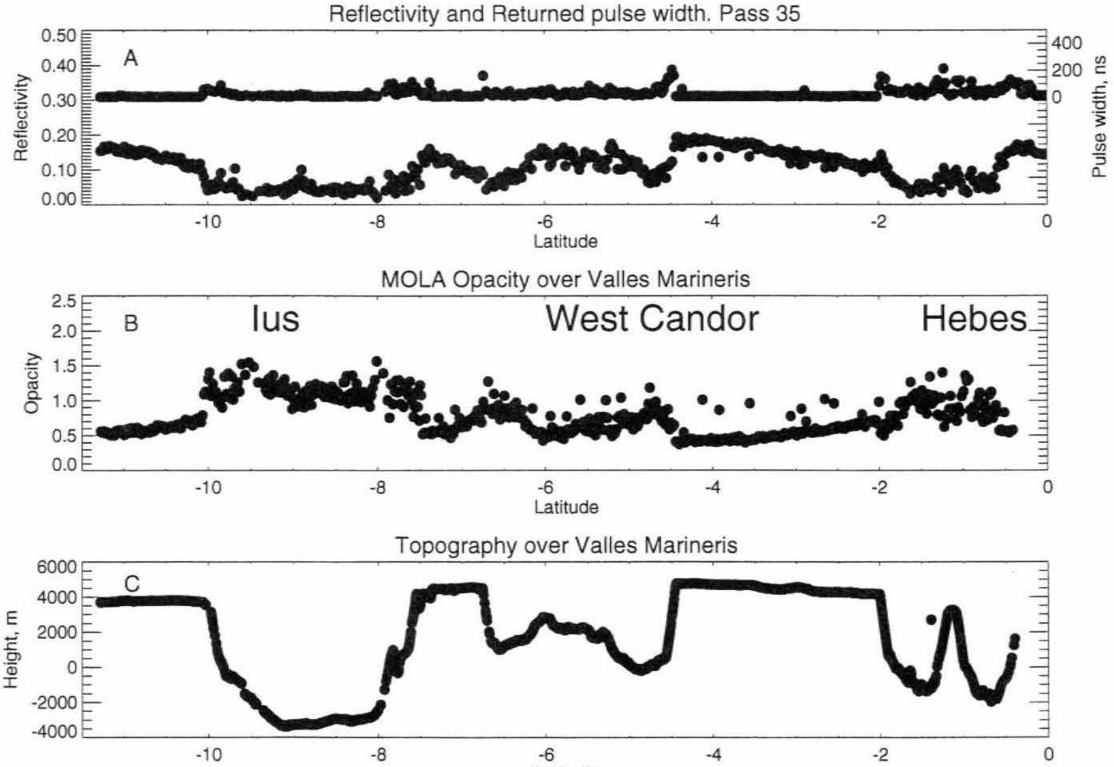

Figure 4.19: $1\mu m$ reflectivity and returned pulse width (A), MOLA atmospheric opacity (B) and topography (C) over the Valles Marineris in the latitude range $11°S$ to $0°N$ near longitude $77°W$ (pass 35). The heights are MOLA altitude track; the opacities were computed from MOLA reflectivity measurements.

Absolute opacity values, that we calculate from MOLA reflectivity using Beer's law, can be used to find the dependence of the opacity on the depth of the canyons. In each of the three canyons in Fig. 4.19, we subtracted opacities on the top of the canyon from opacity on the bottom of the canyon. MOLA opacity difference can be expressed as $\tau_1 - \tau_2 = -0.5\log(\frac{R_1}{A_1}\frac{A_2}{R_2})$. Ratio of the Viking albedo A_2/A_1 is insensitive to the absolute opacity in the image, and we assume that it does not vary significantly across the image. However, this ratio was corrected for the atmosphere inside the canyons, using dust scale height of 10km and canyons' depths from MOLA topography. Opacity difference values are plotted vs. corresponding change in altitude between top and bottom (Fig. 4.20). We can fit a straight line through all points, including (0,0). The single opacity measurement taken in Ius Chasm is shown on a aerosol scale height line of 10.0 km. Differenced opacity can be written as

$$\Delta\tau = \int_{bottom}^{top} N(z)k_e(z)dz, \tag{4.9}$$

where $N(z)$ and $k_e(z)$ are vertical distributions of aerosol number density and extinction cross section. The latter is a function of type of particle size distribution, effective particle size (r_{eff}) and variance of the distribution (v_{eff}). It is also a weak function of refraction index, because the Mie scattering function is fairly constant at this wavelength and our range of particle sizes. The linear nature of the fit to the data suggests that $N(z)$ and $k_e(z)$ are roughly constants. So we obtain:

$$\frac{\Delta\tau}{\Delta h} = N_0 k_{e0} \tag{4.10}$$

We can assume some particle size distribution parameters (r_{eff} and v_{eff}), refraction index for silicates ($n_i = 1.3 - 0.01i$), then calculate k_{e0} and N_0. Mie scattering formalism for spherical particles and lognormal distribution law were used to calculate k_{e0}. Several cases are shown in Table 4.8 along with the corresponding values for N_0. These estimates are performed assuming that there is only dust in the canyons. Clouds may be present in the canyons, and are perhaps likely, but at this point we can

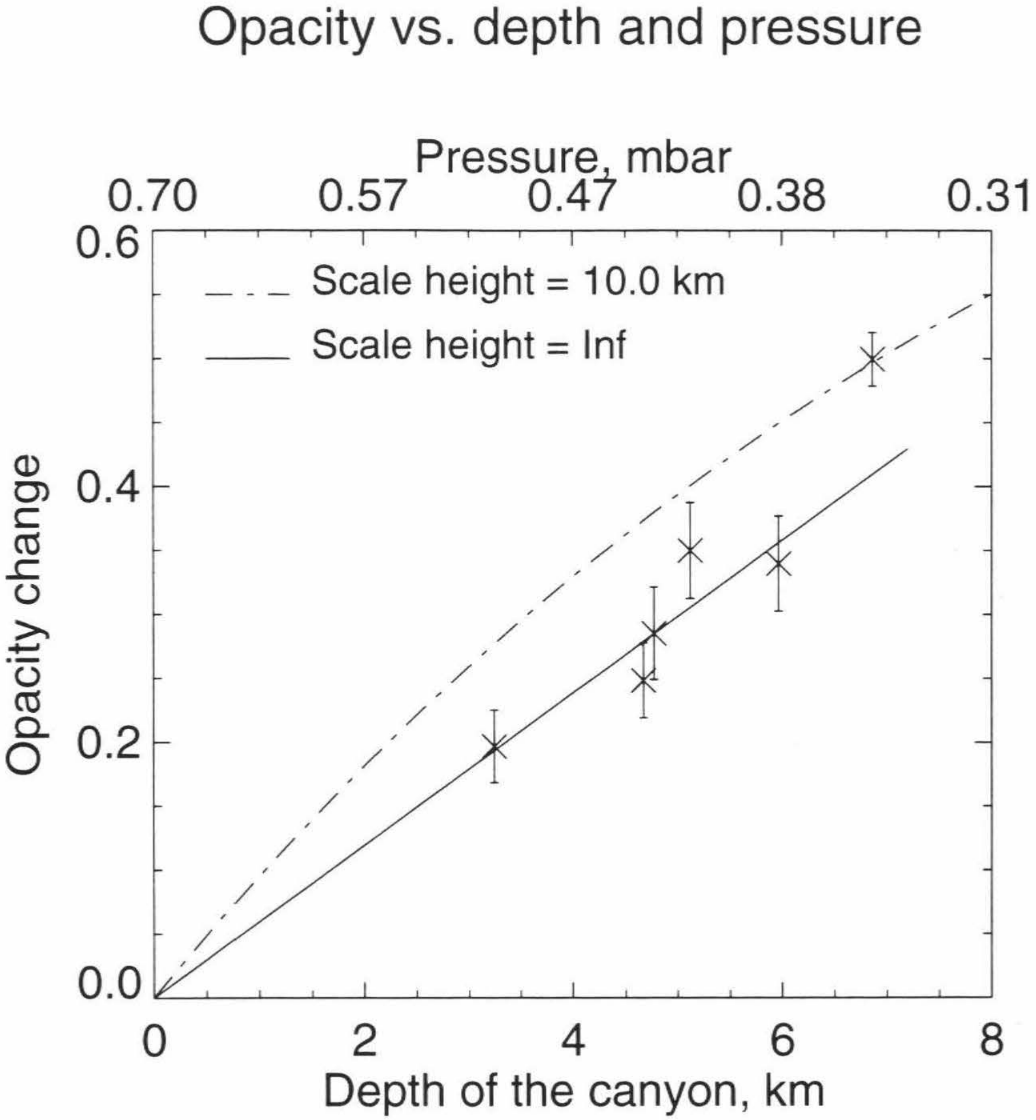

Figure 4.20: Opacity vs. depth and pressure inside Valles Marineris. The linear fit to the points suggest uniform mixing of aerosols inside the canyon. In the deepest canyon, Ius Chasm, mixing is exponential with a scale height of 10.0 km. Error bars show standard deviation of measured opacity. See text for error analysis.

not distinguish between extinction by dust and by clouds. Change of opacity in Ius Chasm is most consistent with the exponential law for number density distribution with scale height of 10.0 km. However, a higher number density of the particles can also explain this outlier from a linear fit.

Number density estimates in Table 4.8 are very crude and heavily depend on parameters of the distribution. The linear dependence of opacity from depth suggests that aerosols are well mixed inside the chasms. Strong winds inside the canyons may explain this distribution. Mars Observer Camera (MOC) images in Valles Marineris area (taken earlier) showed afternoon fogs inside the chasms (Malin (1997)). This may be the case for our observations. Results from the Thermal Emission Spectrometer (TES) should add significant information to this issue.

We must mention several error sources which contribute to the above numbers. They are: uncertainty in calibration of the instrument, Viking image albedo errors, the spectral scaling factor and non-Lambertian reflection from the surface. We estimate that each of those factors (except for the last one, which is relatively small) contribute about 10% error to the absolute opacity estimate at worst. However, since we are using difference of the opacity and, hence, ratios of the measured reflectivities and surface albedos, systematic error is taken out and random errors contribute about 5% uncertainty to the analysis. The effect of the spectral factor is not ratioed out, so overall uncertainty is about 15% for opacity difference numbers and is comparable with the spread of the measurements shown in Fig. 4.20. Finally, opacity difference and number densities are linearly correlated and same error estimates apply to numbers in Table 4.8. We also note that these observational errors are still minor compared to the lack of knowledge of the particle size distribution.

$r_{eff}, \mu m$	v_{eff}	$k_{e0}, \mu m^2$	Reference	Number density, cm^{-3}
1.85	0.5	8.31	Viking Lander[a]	7.17
1.52	0.5	5.83	Viking Lander[a]	10.23
1.8	0.8	4.55	Mariner 9[b]	13.12
1.9	0.25	14.52	Phobos 2[c]	4.11
0.4	0.2	0.61	Viking EPF[d]	98.32

---

[a] Pollack et al. (1995)

[b] Clancy et al. (1995)

[c] Chassefiere et al. (1995)

[d] Clancy and Lee (1991)

4.9 Opacity "events"

On several tracks we have observed rapid drops of reflectivity, spanning about 180 km. Pulse width values became smaller too. These changes were not correlated with surface albedo variations and we attribute them to opacity changes and call them "opacity events." Examples for passes 21, 24 and 30, which all occur at similar latitudes, are shown in Fig. 4.21. Opacity has changed by about 1-1.5 and in some places MOLA even lost the signal due to the opaque atmosphere. We have also observed reflectivity drops north of the shown locations ($70°N - 75°N$) on other tracks, but we were unable to derive opacity due to the poor quality of Viking MDIMs (clouds in the image, poor coverage).

Again, as in the Valles Marineris case, we can not determine whether dust or water or CO_2 crystals produce the higher opacities. The most probable cause of such events are water ice hazes. Hubble Space Telescope team reported observations of water hazes earlier in the season (Lee et al. (1997)) around same latitudes. The local time for MOLA observations was about 5pm and sun is about to set, so we can expect cold temperatures and condensation of water ice. We plan to use TES temperature inversions and limb observations (Christensen et al. (1998)) to check for correlations with our data. MOLA opacity events most probably occur inside the polar vortex, which is identified in the TES data.

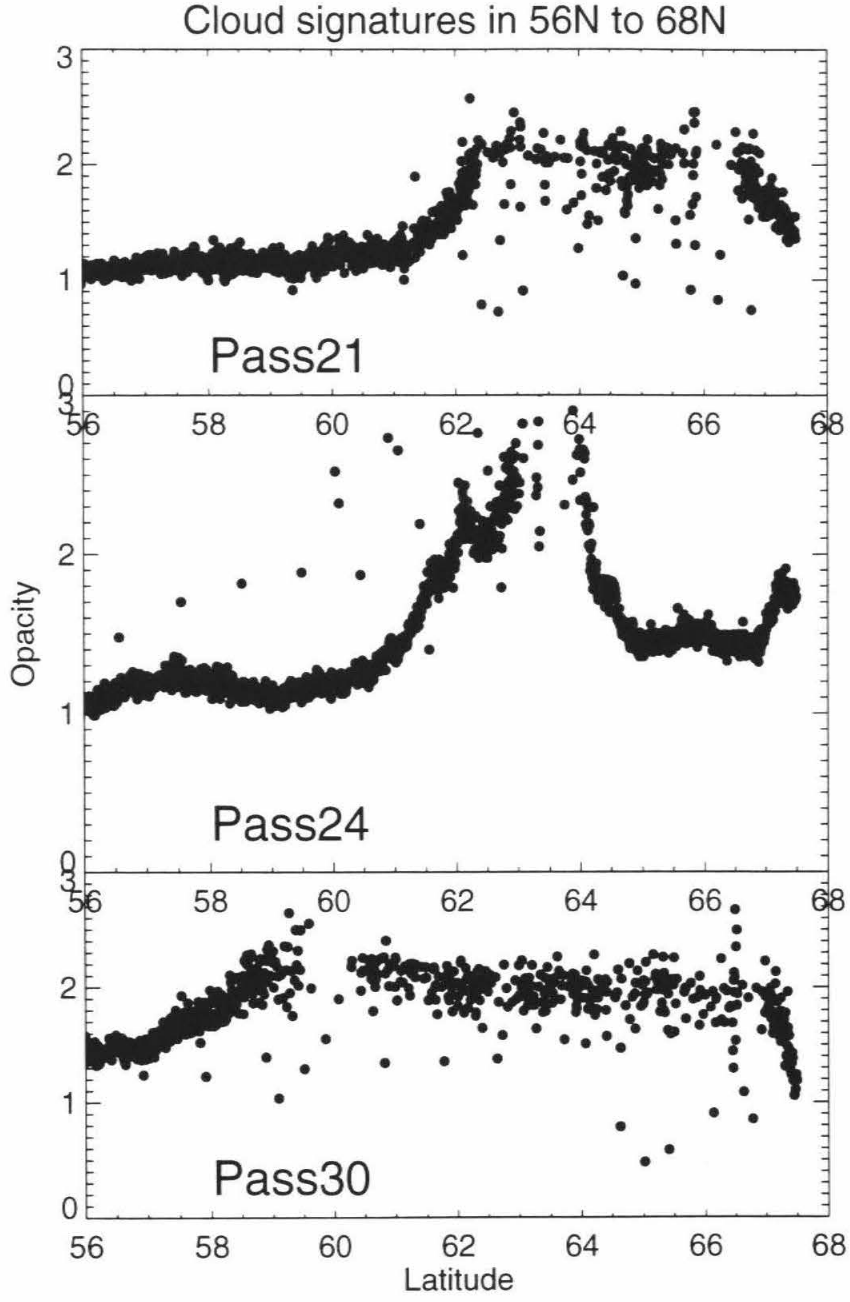

Figure 4.21: Opacity events on passes 21, 24, 30. Suggested explanation is that extinction of photons is due to condensing water or CO_2 ice clouds near the North polar vortex. Data was taken around $L_s = 200°$. Note that absolute values of opacity are very preliminary and may have uncertainties up 50%, though relative changes are very accurate.

4.10 Summary

In this work we have described the MOLA reflectivity dataset for the period through November, 1999 ($L_s = 235°$). The primary goal of the reflectivity measurement is to compile an albedo map of Mars at the MOLA wavelength ($1.064\mu m$). We demonstrated the algorithm which employs TES $9\mu m$ dust opacity and water ice opacity data for the albedo calculation. TES data were collected simultaneously with the MOLA data. More data will be analyzed in the near future as more opacity data becomes available to us.

We showed the utility of MOLA reflectivity measurement to derive opacities of the Martian atmosphere at 1.064 μm, using the albedo dataset compiled by Plescot and Miner (1981). The resulting opacities are consistent with the optical measurements by the Viking Lander spacecrafts and the TES $9\mu m$ dust opacity data. Discrepancies between TES opacity data and the MOLA opacity data allows more insight on the composition of the aerosols, suspended in the Martian atmosphere.

We used opacity changes at the large topographic features to derive aerosol scale heights in the first several kilometers of the Martian atmosphere. Dust scale height is in the range of 2-6 km for Hellas Basin and Alba Patera volcano. Water ice scale height, derived from the observations of aphelion water clouds near the Olympus Mons, is comparable with the atmospheric scale height of 10km. Results from the passes over Valles Marineris suggest that atmospheric aerosols are uniformly mixed in Hebes and Candor Chasms and have a scale height of 10.0 km in the Ius Chasm. Number density estimates vary from 4.11 to 98.32 gm^{-3}, depending on particle size distribution parameters. Large variations in the number density estimates illustrates importance of observations of the Martian atmosphere at different wavelengths.

We report observations of very low reflectivities, compared to expected values, over the regions with low albedo values. We suggest that large atmospheric opacity is the cause of these "events." Most probably they are due to water, condensing on the dust grains, and hazes. Dust storms are another source of high opacities.

Future work will include use of the TES data to aid our calculations of the surface albedo for the whole planet. After the map of surface albedo is completed, it can be used for independent measurements of opacity at the MOLA wavelength. Comparisons of $1\mu m$ opacity results with the $9\mu m$ TES opacity will further contribute to our knowledge of the particle size distribution in the Martian atmosphere, which is important for the understanding thermal balance of the atmosphere.

Acknowledgments

We wish to thank the entire MOLA team for the development of the instrument, its operating and the data collection and reduction. We thank Mike Smith and John Pearl of the TES team for useful discussions and especially for allowing us to use the TES opacity dataset. This work was supported by NASA Grant NAG5-4437.

Chapter 5 Summary and future research

This dissertation presents a part of the Mars Orbiter Laser Altimeter (MOLA) investigation, which is relevant to climatological processes of different time scales. The evolution of the polar ice caps and layered deposits is directly related to the history of the Martian climate. We suggest that sublimation is one of the most important processes shaping the residual polar ice caps. Sublimation acts on a shorter time scale than the ice flow. Formation of the polar CO_2 clouds and observations of opacity are important for characterization of the current state of the Martian atmosphere. Important comparisons have been performed with the MGS Thermal Emission Spectrometer data, which provide more insights into the polar atmospheric processes and properties of suspended aerosols. The normal albedo at $1.064\mu m$ wavelength can be derived from the MOLA reflectivity measurement, assuming a knowledge about atmospheric opacity. We presented some initial results of the albedo calculation algorithm, that employs TES $9\mu m$ dust opacity.

5.1 Sublimation of the ice caps

The ice sublimation model, presented in Chapter 2, addresses an important question about the history of ice caps formation. We studied the evolution of the form of the residual ice caps over a period of about 100 million years. We also attempted to quantify and simulate the mysterious spiraling troughs in the layered deposits. Our model was justified using very precise MOLA topographic data for the North Polar region. We found very good agreement between observed general shape of the ice cap and model results. We have also studied depth and slopes of almost 200 trough profiles in the North Polar Layered deposits. The sublimation model produced a reasonable agreement with a form of an "average" trough. We were also able to constrain the time scale for the formation of the ice caps between 10 and 100 millions of years.

although we favor the shorter time scale. The time scale for trough formation was found to be bounded by 1 and 16 millions of years. This time scale may be even shorter because we did not account for the wind erosion in our model.

With this model we have studied the change of form of the ice caps under simple assumptions. There are several experiments which can be performed with the model in the future. Feedback between water vapor in the atmosphere and sublimating ice can be introduced into the model. It will be possible to control total balance of water vapor over the ice cap. In this work, we have the water cycle which is similar to the observed by the MAWD instrument. The water balance can be significantly different for another orbital cycle. We considered the sublimation of the caps using the current Martian orbit. The inferred time scales for the formation of the observed shape are significantly larger than any of the known orbital variations. Introduction of these variations will greatly improve the quality of the sublimation model and may provide some clues to the formation of the layered terrains. Finally, boundary layer atmospheric processes near the Martian ice caps have not yet been quantified on Mars in detail. We had to assume large variations of the wind speeds (1-10 m/s) over the caps. This is one of the major source of time scale uncertainty. We hope that future Mars Polar Lander mission will provide excellent data on the summer environment of the South polar layered deposits. An ice flow model is necessary to understand evolution of the ice caps for periods longer than 100 million years. It is important to understand interaction of all physical processes acting in the polar regions and their relative time scales.

5.2 Polar clouds

The thermal balance of the polar regions depends greatly on the condensation of CO_2 in the polar night conditions. Chapter 3 discussed first comprehensive observations of the Martian polar clouds during the end of the northern winter ($L_s = 300° - 7°$), the southern winter ($L_s = 103° - 180°$) and northern fall ($L_s = 180° - 240°$). On the basis of the reflective properties and spatial occurrence, we can distinguish two major classes (types) of clouds. Type 1 clouds are observed right over the residual ice caps, poleward of 80°. These clouds appear as linear "sawtooth" structures, forming with $0° - 20°$ slope angles. Linear extent of one "tooth" is about 20km and horizontal extent ranges from 0 to 8km. The highest cloud return was detected at 20km above the surface. Type 1 clouds are usually detected in channel 4 (the widest channel). Type 2 clouds have been observed only in the southern winter and occupy a latitude band between 70°S and 80°S. These clouds do not exhibit linearity of the type 1 clouds. Type 2 clouds are spread out randomly in altitude from the ground up to 7km over the ground. Horizontal extent reaches 600km. Cloud tops are more reflective than tops of the type 1 clouds. Detections are very sparse, but usually channel 1 (the narrowest channel) triggers. Type 2 clouds are possibly clusters of condensate 300-600 m apart. Comparison with Earth water clouds, performed on the basis of volume backscattering coefficient, suggest that the Martian polar clouds would visually appear as haze (type 1) and mother-of-pearl (type 2) clouds. We have also performed comparisons with the simultaneous observations of the brightness temperature at 18 and $25\mu m$ by the MGS thermal emission spectrometer (TES). MOLA observations confirmed that low brightness temperature zones in the TES data are due to the CO_2 snowfall over the ice caps.

We hope that we will be able to complete our observations of the polar cloud formation in the northern polar winter, i.e., for L_s range from 240° to 300°. Reflective properties of the CO_2 ice are poorly known. For our calculations, we have assumed Mie scattering for spheres, but this might be far from reality. It is very important to use a microphysical model for CO_2 condensation to interpret MOLA backscattering coefficient in terms of scattering properties and ice grain sizes. Some general ideas for the conditions of CO_2 ice cloud formation were presented in Forget et al. (1998). It is now possible to establish a link between morphology of the clouds and processes of their formation. Pettengill and Ford (1998) and Colaprete and Toon (1999) suggested lee waves as a possible process for the formation of type 1 clouds. Section 3.7 discusses comparison of only two tracks of data from the MOLA and the TES instruments. Many more TES brightness temperature data and cloud distributions observed by

MOLA have to be analyzed. This comparison will enable us to distinguish between condensation of CO_2 on the ground and CO_2 snowfall.

5.3 Albedo and opacity

MOLA reflectivity measurement is a product of surface albedo and atmospheric transmissivity. Chapter 4 presents observations of the reflectivity for the duration of the MOLA mission up to $L_s = 240^\circ$. Saturation of the reflectivity measurement did not allow complete mapping of the planet. During the dust storm season, when the dust atmospheric loading was at its maximum, MOLA collected unsaturated reflectivity data from about 70% of the planet. The bright Tharsis region still remains very poorly mapped in reflectivity. We demonstrated derivation of the normal albedo of the surface or total atmospheric opacity from the reflectivity measurement. The resulting albedo is consistent with the Plescot and Miner (1981) albedo. To calculate the total atmospheric opacity we used the Viking IRTM albedo dataset compiled by Plescot and Miner (1981). Calculated values of the total atmospheric opacity are similar to the opacity values performed by the Viking Lander stations (Colburn et al. (1989)) and the Mars Pathfinder (Smith and Lemmon (1999)). Opacities derived for the north regions exhibit large deviations from a seasonal trend. These deviations are possibly due to the storms, passing near the North Polar Ice Cap in the northern summer and fall. Opacity observations in the South Polar regions display south polar hood activity over the seasonal trend ($L_s = 170^\circ - 190^\circ$). An algorithm for the calculation of an aerosol scale height is presented. It is based on the variations of opacity on large topographic features, such as Olympus Mons, Alba Patera and Hellas Basin. We found that values of the scale height ($1 - 6$km) are generally lower than the atmospheric scale height (~ 10km) near Alba Patera and Hellas Basin. Opacity in these regions is possibly due to dust. This suggests that dust is concentrated in the first few kilometers of the atmosphere. Observations of the scale height of the aphelion water cloud belt over Olympus Mons are consistent with the atmospheric scale height. In the Hellas Basin we observed some seasonal variation of the aerosol scale height. Day and night differences were not found to be significant.

One of the primary scientific objectives of the MOLA investigation is to compile a map of normal surface albedo at the MOLA wavelength. In section 4.4 we discussed an algorithm employing the $9 \mu m$ dust opacity, derived from the MGS Thermal Emission Spectrometer observations by Smith et al. (1999b) and presented some initial results. The values of albedo at the MOLA wavelength appear to be consistent with the Plescot and Miner (1981) dataset, after the correction suggested by Clancy and Lee (1991) is applied to the Plescot and Miner (1981) dataset. More data from the TES instrument will be available to us in near future, thanks to generosity of M. Smith, J. Pearl and B. Conrath from the TES team. Using the data from the mapping orbits, especially the data from the dust storm season, we will able to compile a map of the normal albedo at $1 \mu m$.

5.4 Conclusions

The MOLA investigation has contributed greatly to the knowledge about the planet Mars. The global topographic map of Mars with less than 5 m absolute error is considered to be one of the major results of the Mars Global Surveyor mission. This work presents the part of the MOLA investigation which is related to some issues of the Martian climatology. We discussed the sublimation of the Martian ice caps and supported our model with precise topography of the polar regions measured by MOLA. We suggested additional time constraints on the evolution history of the polar layered deposits. We added to the knowledge about the current state of the Martian atmosphere by measuring total atmospheric opacity at the MOLA wavelength. We demonstrated how normal albedo map can be compiled from the MOLA reflectivity measurement, when necessary MOLA and TES observations are available.

The MOLA investigation has only began. It will continue to provide high-quality data about our neighbor planet and will help us to resolve many puzzles about the planet Mars.

Bibliography

Abshire, J. B., Sun, X., and Afzal, R. S. (1999). Mars Orbiter Laser Altimeter: Reciever model and performance analysis. *in press, Applied Optics.*

Bell, J., McCord, T., and Owensby, P. (1989). High spectral resolution 0.3-1.0μm spectroscopy and imaging of Mars during the 1988 opposition. Characterization of Fe mineralogy. In *Fourth International Conference on Mars*, pages 67–68. Tucson, Arizona.

Bell, J., Wolff, M., Daley, T., Crisp, D., James, P., Lee, S., Trauger, J., and Evans, R. (1999). Near-infrared imaging of Mars from HST: Surface reflectance, photometric properties, and implications for MOLA data. *Icarus*, 138(1):25–35.

Blasius, K. R., Cutts, J. A., and Howard, A. D. (1982). Topography and stratigraphy of Martian polar layered deposits. *Icarus*, 50(2-3):140–160.

Brutsaert, W. (1965). A model for evaporation as a molecular diffusion process into a turbulent atmosphere. *Journal of Geophysical Research*, 70(20):5017–5024.

Brutsaert, W. (1982). *Evaporation into the atmosphere*. D. Reidel Publishing Company.

Chassefiere, E., Drossart, P., and Korablev, O. (1995). Post-Phobos Model For The Altitude And Size Distribution Of Dust In The Low Martian Atmosphere. *Journal Of Geophysical Research Planets*, 100(E3):5525–5539.

Christensen, P., Anderson, D., Chase, S., Clancy, R., Clark, R., Conrath, B., Kieffer, H., Kuzmin, R., Malin, M., Pearl, J., and Roush, T. (1998). Results From The Mars Global Surveyor Thermal Emission Spectrometer. *Science*, 279(5357):1692–1698.

Christensen, P., Anderson, D., Chase, S., Clark, R., Kieffer, H., Malin, M., Pearl, J., Carpenter, J., Bandiera, N., Brown, F., and Silverman, S. (1992). Thermal Emission Spectrometer experiment - Mars Observer mission. *Journal Of Geophysical Research-Planets*, 97(E5):7719–7734.

Clancy, R. and Lee, S. (1991). A New Look At Dust And Clouds In The Mars Atmosphere - Analysis Of Emission-Phase-Function Sequences From Global Viking Irtm Observations. *Icarus*, 93(1):135–158.

Clancy, R., Lee, S., Gladstone, G., Mcmillan, W., and Rousch, T. (1995). A New Model For Mars Atmospheric Dust Based Upon Analysis Of Ultraviolet Through Infrared Observations From Mariner-9, Viking, And Phobos. *Journal Of Geophysical Research Planets*, 100(E3):5251–5263.

Clifford, S. M. (1987). Polar basal melting on Mars. *Journal of Geophysical Research, B, Solid Earth and Planets*, 92(9):9135–9152.

Colaprete, A. and Toon, O. B. (1999). Simulations of carbon dioxide cloud formation at the Martian poles. In *BAAS*, volume 31(4), page 1179.

Colburn, D., Pollack, J., and Haberle, R. (1989). Diurnal-Variations In Optical Depth At Mars. *Icarus*, 79(1):159–189.

Cutts, J. A. and Lewis, B. H. (1982). Models of climate cycles recorded in Martian polar layered deposits. *Icarus*, 50(2-3):216–244.

Deirmendjian, D. (1969). *Electromagnetic scattering on spherical polydispersions*. American Elsevier Pub. Co.

Durham, W. B. (1998). Factor affecting rheological properties of Martian polar ice. In *1st International Mars Polar Science and Exploration Conference*, pages 8–9. LPI contribution no. 953, Lunar and Planetary Institute, Houston.

Dzurisin, D. and Blasius, K. R. (1975). Topography of the polar layered deposits of Mars. *Journal of Geophysical Research*, 80(23):3286–3306.

Eliason, E., McEwen, A., Allison, A., Batson, R., Soderblom, L., and Martin, M. (1992). Introduction to the Mars Mosaicked Digital Image Model (MDIM) CDROM volumes. Technical report, JPL.

Erard, S. and Calvin, W. (1997). New composite spectra of Mars, 0.4-5.7 μm. *Icarus*, 130(2):449–460.

Farmer, C. B., Davies, D. W., and LaPorte, D. D. (1976). Mars: northern summer ice cap, water vapor observations from Viking 2. *Science*, 194(4271):1339–1341.

Farmer, C. B. and Doms, P. E. (1979). Global seasonal variation of water vapor on Mars and the implications for permafrost. *Journal of Geophysical Research*, 84(B6):2881–2888.

Fenton, L., Pearl, J., and Martin, T. (1997). Mapping Mariner 9 dust opacities. *Icarus*, 130(1):115–124.

Fishbaugh, K. and Head, J. (1999). North polar region of mars: Topography of circumpolar deposits from Mars Orbiter Laser Altimeter (MOLA) data and evidence for asymmetric retreat of the polar cap. *Submitted to Journal Geophysical Research*.

Forget, F. (1998). Mars CO_2 ice polar caps. In Schmitt, B. and et al., editors, *Solar System Ices*, pages 477–507. Kluwer Academic Publishers.

Forget, F., Hourdin, F., and Talagrand, O. (1998). co_2 snowfall on Mars: Simulation with a general circulation model. *Icarus*, 131(2):302–316.

Garvin, J., Bufton, J., Blair, J., Harding, D., Luthcke, S., Frawley, J., and Rowlands, D. (1998). Observations of the Earth's topography from the Shuttle Laser Altimeter (SLA): laser-pulse echo-recovery measurements of terrestrial surfaces. *Phys. Chem. Earth,*, 23(9-10):1053–1068.

Gierasch, P. J. and Goody, R. (1968). A study of the thermal and dynamical state of the Mars atmosphere. *Planetary Space Science*, 16:615–646.

Haberle, R. and Jakosky, B. (1990). Sublimation and transport of water from the north residual polar cap on Mars. *Journal Of Geophysical Research-Solid Earth And Planets*, 95(B2):1423–1437.

Hansen, J. E. and Travis, L. D. (1974). Light scattering in planetary atmospheres. *Space Science Reviews*, 16:527–610.

Hapke, B., Nelson, R., and Smythe, W. (1998). The opposition effect of the moon: Coherent backscatter and shadow hiding. *Icarus*, 133(1):89–97.

Herkenhoff, K. E. and Murray, B. C. (1990). High-resolution topography and albedo of the south polar layered deposits on Mars. *Journal of Geophysical Research*, 95:14511–14529.

Herr, K. and Pimental, G. (1970). Evidence for solid carbon dioxide in the upper atmosphere of Mars. *Science*, 167:47–49.

Hinson, D., Flasar, F., and Tyler, G. (1999). Recent results from radio occultation measurements with Mars Global Surveyor. In *AGU Fall Meeting*.

Hofstadter, M. and Murray, B. (1990). Ice sublimation and rheology - implications for the Martian polar layered deposits. *Icarus*, 84(2):352–361.

Howard, A. D. (1998). The role of eolian processes in forming Martian polar topography. In *First International Conference on Mars Polar Science and Exploration*, pages 19–20. LPI contribution No. 953, Lunar and Planetary Institute, Houston.

Howard, A. D., Cutts, J. A., and Blasius, K. R. (1982). Stratigraphic relationships within Martian polar cap deposits. *Icarus*, 50(2-3):161–215.

Ingersoll, A. P. (1970). Mars: occurrence of liquid water. *Science*, 168(3934):972–973.

Ivanov, A. and Muhleman, D. (1998). Opacity of the Martian atmosphere from the Mars Orbiter Laser Altimeter (MOLA) observations. *Geophysical Research Letters*, 25(24):4417–4420.

Ivanov, A. and Muhleman, D. (1999a). Observations of polar night clouds with the Mars Orbiter Laser Altimeter (MOLA). In *Fifth International Conference on Mars*.

Ivanov, A. and Muhleman, D. (1999b). Opacity of polar night clouds on Mars. In *Geophysical Research Abstracts*, volume 16(3), page 987.

Ivanov, A. and Muhleman, D. (2000). The role of sublimation for the formation of the Northern ice cap: Results from the Mars Orbiter Laser Altimeter. *Icarus*, 144(2):436–448.

Jakob, M. (1957). *Heat Transfer*, volume 1. New York, Wiley.

Jakosky, B. M. and Farmer, C. B. (1982). The seasonal and global behavior of water vapor in the Mars atmosphere; complete global results of the Viking atmospheric water detector experiment. *Journal of Geophysical Research, B*, 87(4):2999–3019.

Jakosky, B. M. and Haberle, R. M. (1992). The seasonal behavior of water on Mars. In Mars, Kieffer, H. H., Jakosky, B. M., Snyder, C. W., and Matthews, M. S., editors, *chapter 28*, pages 969–1016. The University of Arizona Press.

James, P. B., Kieffer, H. H., and Paige, D. A. (1992). The seasonal cycle of carbon dioxide on Mars. In Mars, Kieffer, H. H., Jakosky, B. M., Snyder, C. W., and Matthews, M. S., editors, *chapter 27*, pages 934–968. The University of Arizona Press.

Kieffer, H. H., Chase, C. S. J., Martin, T. Z., Miner, E. D., and Palluconi, F. D. (1976a). Martian North Pole summer temperatures: dirty water ice. *Science*, 194(4271):1341–1344.

Kieffer, H. H., Chase, C. S. J., Miner, E. D., Palluconi, F. D., Muench, G., Neugebauer, G., and Martin, T. Z. (1976b). Infrared thermal mapping of the Martian surface and atmosphere: first results. *Science*, 193(4255):780–786.

Kieffer, H. H., Martin, T. Z., Peterfreund, A. R., Jakosky, B. M., Miner, E. D., and primary mission. *Journal of Geophysical Research*, 82(28):4249–4291.

Lee, S., James, P., and Clancy, T. (1997). Rapid weather changes observed on Mars. Technical Report STScI-PRC97-24, Space Telescope Science Institute.

Leighton, R. B. and Murray, B. C. (1966). Behavior of carbon dioxide and other volatiles on Mars. *Science*, 152:136–144.

Malin, M. (1997). MOC Aerobraking Orbit Color Image #1 - p013. *MSSS Press Release.*

Malin, M. C. (1986). Density of Martian North Polar layered deposits: implications for composition. *Geophysical Research Letters*, 13(5):444–447.

Martin, T. (1986). Thermal infrared opacity of the Mars atmosphere. *Icarus*, 66(1):2–21.

Martin, T. and Richardson, M. (1993). New dust opacity mapping from Viking Infrared Thermal Mapper data. *Journal Of Geophysical Research-Planets*, 98(E6):10941–10949.

Nelson, R., Hapke, B., Smythe, W., and Horn, L. (1998). Phase curves of selected particulate materials: The contribution of coherent backscattering to the opposition surge. *Icarus*, 131(1):223–230.

Paige, D., Bachman, J., and Keegan, K. (1994). Thermal and albedo mapping of the polar-regions of Mars using Viking Thermal Mapper observations .1. North polar region. *Journal Of Geophysical Research-Planets*, 99(E12):25959–25991.

Paige, D. and Keegan, K. (1994). Thermal and albedo mapping of the polar regions of Mars using Viking Thermal Mapper observations .2. South polar region. *Journal Of Geophysical Research-Planets*, 99(E12):25993–26013.

Paige, D. A. (1985). *The Annual Heat Budget of the Martian Polar Ice Caps from Viking Observations.* PhD thesis, California Institute of Technology.

Paterson, W. S. B. (1994). *The physics of glaciers.* Elsvier Science.

Peixoto, J. P. and Oort, A. H. (1992). *Physics of climate.* American Institute of Physics.

Pettengill, G. H. and Ford, P. G. (1998). Atmospheric gravity waves in the Martian North polar cap winter. In *Eos*, volume 79(45). AGU.

Pierrehumbert, R. and Erlick, C. (1998). On the scattering greenhouse effect of CO_2 ice clouds. *Journal Of The Atmospheric Sciences*, 55(10):1897–1903.

Plaut, J., Kahn, R., Guinness, E., and Arvidson, R. (1988). Accumulation of sedimentary debris in the south polar region of Mars and implication for climate history. *Icarus*, 75:357–377.

Plescot, J. and Miner, E. (1981). Time variability of Martian bolometric albedo. *Icarus*, 41:179–201.

Pollack, J., Ockert-Bell, M., and Shepard, M. (1995). Viking Lander Image-Analysis Of Martian Atmospheric Dust. *Journal Of Geophysical Research Planets*, 100(E3):5235–5250.

Priestley, C. H. B. (1959). *Turbulent transfer in the lower atmosphere.* The University of Chicago Press.

Santee, M. and Crisp, D. (1993). Thermal structure and dust loading of the Martian atmosphere during late Southern summer - Mariner-9 revisited. *Journal Of Geophysical Research-Planets*, 98(E2):3261–3279.

Shkuratov, Y., Kreslavsky, M., Ovcharenko, A., Stankevich, D., Zubko, E., Pieters, C., and Arnold, G. (1999). Opposition effect from Clementine data and mechanisms of backscatter. *Icarus*, 141(1):132–155.

Smith, D., Zuber, M., Solomon, S., Abshire, J., Afzal, R., Aharonson, O., Fishbaugh, K., Ford, P., Frey, H., Garvin, J., Head, J., Ivanov, A., Johnson, C., Muhleman, D., Neumann, G., Pettengill, G., Phillips, R., Sun, Z., Zwally, H., Banerdt, W., and Duxbury, T. (1999a). The global topography of Mars and implications for surface evolution. *Science*, 284(5419):1495–1503.

Smith, D. E., Zuber, M. T., Frey, H., Garvin, J., Head, J., Muhleman, D., Pettengill, G., Phillips, R., Solomon, S., Zwally, H., and Banerdt, W. (1998). Topography of the Northern-Hemisphere of Mars from the Mars Orbiter Laser Altmeter. *Science*, 279(5357):1686–1692.

Smith, M., Pearl, J., Conrath, B., and Christensen, P. (1999b). Mars Global Surveyor Thermal Emission Spectrometer (TES) observations of dust opacity and science phasing. *JGR*, in press.

Smith, P. and Lemmon, M. (1999). Opacity of the Martian atmosphere measured by the imager for Mars Pathfinder. *Journal Of Geophysical Research-Planets*, 104(E4):8975–8985.

Soderblom, L. (1992). The composition and mineralogy of the Martian surface from spectroscopic observations: 0.3 μ m to 50 μ m. In Mars, H. K., Jakosky, B., Snyder, C., and Matthews, M., editors, *chapter 17*. University of Arizona Press.

Squyres, S. W. (1979). The evolution of dust deposits in the Martian North Polar region. *Icarus*, 40(2):244–261.

Thomas, P., Squyres, S., Herkenhoff, K., Howard, A., and Murray, B. (1992). Polar deposits of Mars. In Mars, Kieffer, H. H., Jakosky, B. M., Snyder, C. W., and Matthews, M. S., editors, *chapter 23*, pages 767–798. The University of Arizona Press.

Tillman, J., Landberg, L., and Larsen, S. (1994). The boundary-layer of Mars - fluxes, stability, turbulent spectra, and growth of the mixed-layer. *Journal Of The Atmospheric Sciences*, 51(12):1709–1727.

Titus, T., Kieffer, H., Mullins, K., and Christensen, P. (1999). Slab ice and snow flurries in the Mars Northern Polar night. In *AGU Fall Meeting*.

Toigo, A. and Richardson, M. (1999). Seasonal variation of aerosols in the Martian atmosphere. *Submitted to Journal of Geophysical Research.*

Toon, O., Pollack, J., and Sagan, C. (1977). Physical properties of the particles composing the Martian dust storm of 1971-1972. *Icarus*, 30(4):663–696.

Toon, O. B., Pollack, J. B., Ward, W., Burns, J. A., and Bilski, K. (1980). The astronomical theory of climatic change on Mars. *Icarus*, 44:552–607.

Warren, S. (1986). Optical-constants of carbon-dioxide ice. *Applied Optics*, 25(16):2650–2674.

Zuber, M., Smith, D., Solomon, S., Abshire, J., Afzal, R., Aharonson, O., Fishbaugh, K., Ford, P., Frey, H., Garvin, J., Head, J., Ivanov, A., Johnson, C., Muhleman, D., Neumann, G., Pettengill, G., Phillips, R., Sun, Z., Zwally, H., Banerdt, W., and Duxbury, T. (1998a). Observations of the north polar region of Mars from the Mars Orbiter Laser Altimeter. *Science*, 282(5396):2053–2060.

Zuber, M., Smith, D., Solomon, S., Muhleman, D., Head, J., Garvin, J., Abshire, J., and Bufton, J. (1992). The Mars-Observer Laser Altimeter Investigation. *Journal Of Geophysical Research Planets*, 97(E5):7781–7797.

Zuber, M. T., Lim, L., and Zwally, J. (1998b). The role of viscous flow in the morphology of the Martian North polar cap. In *First International Conference on Mars Polar Science and Exploration*, pages 45–46. LPI contribution No. 953, Lunar and Planetary Institute, Houston.